

DISSERTATION

EFFECTS OF BACKGROUND WINDS AND TEMPERATURE ON  
BORES, STRONG WIND SHEARS AND CONCENTRIC GRAVITY  
WAVES IN THE MESOPAUSE REGION

Submitted by

Jia Yue

Electrical and Computer Engineering Department

In partial fulfillment of the requirements

For the Degree of Doctor of Philosophy

Colorado State University

Fort Collins, Colorado

Fall 2009

UMI Number: 3400981

All rights reserved

INFORMATION TO ALL USERS

The quality of this reproduction is dependent upon the quality of the copy submitted.

In the unlikely event that the author did not send a complete manuscript and there are missing pages, these will be noted. Also, if material had to be removed, a note will indicate the deletion.



UMI 3400981

Copyright 2010 by ProQuest LLC.

All rights reserved. This edition of the work is protected against unauthorized copying under Title 17, United States Code.



ProQuest LLC  
789 East Eisenhower Parkway  
P.O. Box 1346  
Ann Arbor, MI 48106-1346

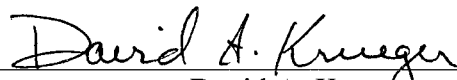
COLORADO STATE UNIVERSITY

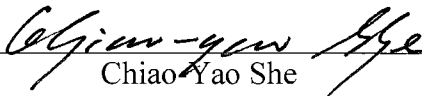
August 26, 2009

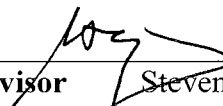
WE HEREBY RECOMMEND THAT THE DISSERTATION PREPARED UNDER OUR SUPERVISION BY JIA YUE ENTITLED EFFECTS OF BACKGROUND WINDS AND TEMPERATURES ON BORES, STRONG WIND SHEARS AND CONCENTRIC GRAVITY WAVES IN THE MESOPAUSE REGION BE ACCEPTED AS FULFILLING IN PART REQUIREMENTS FOR THE DEGREE OF DOCTOR OF PHILOSOPHY.

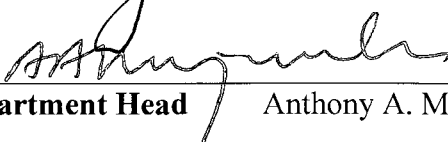
Committee on Graduate Work

  
\_\_\_\_\_  
Mario C. Marconi

  
\_\_\_\_\_  
David A. Krueger

  
\_\_\_\_\_  
**Advisor** Chiao Yao She

  
\_\_\_\_\_  
**Co-Advisor** Steven C. Reising

  
\_\_\_\_\_  
**Department Head** Anthony A. Maciejewski

## ABSTRACT OF DISSERTATION

### EFFECTS OF BACKGROUND WINDS AND TEMPERATURE ON BORES, STRONG WIND SHEARS AND CONCENTRIC GRAVITY WAVES IN THE MESOPAUSE REGION

Using data from the CSU sodium Doppler lidar and Kyoto University OH airglow imager at Fort Collins, CO (40.6N, 105W), supplemented by meteorological data in the lower atmosphere, this thesis provides a comprehensive, though qualitative, understanding for three different yet related observed fluid-dynamical phenomena in the mesopause region.

The first project involves the convection-excited gravity waves observed in the OH airglow layer at 87 km. Two case studies on May 11, 2004 and September 9, 2005 are discussed in detail along with statistical studies and a ray-tracing modeling. A single convection source matches the center of the concentric gravity waves. The horizontal wavelengths and periods of these gravity waves were measured as functions of both radius and time. These results agreed reasonably well with the internal Boussinesq gravity wave dispersion relation with an assumed zero background wind. The weak mean background wind between the lower and middle atmosphere (10 to 90 km) determines the penetration of the gravity waves into higher altitude.

The second project involves mesospheric bores observed by the same OH imager. The observation on October 9, 2007 reveals the close correlation between breaking large-scale gravity waves and mesospheric bores. It suggests that when a

large-amplitude gravity wave is trapped in a thermal or shear duct, its wave front could steepen and forms bore-like structure in the mesopause. In turn, the large gravity wave and its bore may significantly impact the background. Studying all ~8 observed cases reveals the possible link between the jet/front system in the lower atmosphere and the propagation and ducting of large-scale gravity waves and associated bores in the mesopause region of the atmosphere.

The third project involves the relationship between large wind shear generation and sustainment and convective/dynamic stabilities measured by the sodium lidar at the altitude of 80-105 km during 2002-2005. A large wind shear could substantially affect the electrodynamics in the ionosphere through Lorentz force acting on ionized particles. The correlation between windshear,  $S$ , and Brunt-Vaisala frequency,  $N$ , as observed by lidar suggests that the maximum sustainable windshear is determined by the necessary condition for dynamic instability of Richardson number  $R=0.25$ , leading to the result that the maximal windshear occurs at altitudes of lower thermosphere where the atmosphere is convectively very stable (large value of  $N^2$ ), ~ 100 km in winter and ~ 90 km in summer. Through a case study and more than 20 examples (not shown), we conclude that at the temporal and vertical resolution of 15 min and 2 km, the dominate source for sustainable large windshears appears to be the semidiurnal tidal-period perturbations with shorter vertical wavelengths and greater amplitude, compared to the typical solar tides.

Though the observations of concentric gravity waves, mesospheric bores and large windshears were made previously at other locations, our long-time studies with

5 to 10 times more observational data have enabled us to draw new comprehensive conclusions.

Jia Yue  
Electrical and Computer Engineering Department  
Colorado State University  
Fort Collins, CO 80523  
Fall 2009

## Acknowledgements

First, I would like to thank my advisor, Chiao-Yao (Joe) She for his endless support and insightful guidance. Since I met Joe in 2003, his enthusiasm about the good science and technology always encouraged me when I faced difficulties. Joe's dedication in his research and teaching gives me a perfect example of how to be a scientist. I also thank my committee members, Dr. David Krueger, co-advisor Dr. Steve Reising and Dr. Mario Marconi for their help on my dissertation.

Lidar is always a team effort. No individual can obtain 24-hours of good lidar data by himself. Thanks to my CSU lidar group fellows, Titus Yuan, Sean Harrell and Phil Acott. It has always fun to work on the technical and scientific problems with them. In the process, I learned a lot.

For the past a few years, I've received help from many scientists outside CSU. Among them, I'd emphasize three collaborators and mentors. They not only helped me on my dissertation, they will also work with me closely in my post-graduate career. Dr. Sharon Vadas spent a lot time on the concentric gravity wave paper, which is my paper and means a lot to me. She taught me step by step how to write a good scientific publication. Dr. Hanli Liu is always available to answer my sometimes naïve questions. He is so unselfish to share his knowledge with me. Thanks to Dr. Takuji Nakamura who generously shared his Yucca Ridge imager data with us. This dissertation replies heavily on the imager data and several good publications came out of it.

I would also thank my master's advisor, Dr. Richard Collins. He has believed that I could become a geophysical scientist since he guided me into this field. He has more confidence in me than even I do sometimes.

Finally, I would thank my wife, Sisi Zhang and my parents for their endless support. During such a long journey to get a PhD, Sisi's patience means a lot to me.

## Table of Contents

Chapter 1: Introduction.....	1
1.1 Earth's atmosphere.....	2
1.1.1 Introduction to the earth's atmosphere.....	2
1.1.2 Mesopause dynamics.....	5
1.2 Structure of dissertation.....	10
Chapter 2: Colorado State University Sodium Lidar System and Kyoto University OH all-sky imager.....	12
2.1 Fundamental Theory of Sodium Temperature and Wind Lidar.....	13
2.1.1 Sodium D <sub>2</sub> transition and fluorescence.....	13
2.1.2 Doppler broadening and shifting of the sodium fluorescence spectrum	15
2.1.3 Sodium fluorescence spectrum: the basis of the CSU sodium lidar...	16
2.1.4 Sodium lidar equation.....	18
2.1.5 Lidar temperature and wind ratios and calibration curve.....	20
2.2 Sodium lidar system.....	22
2.2.1 Sodium lidar transmitter.....	22
2.2.2 Sodium lidar receiver.....	33
2.2.3 Sodium lidar electronics and control system.....	36
2.3 Kyoto University OH airglow all-sky imager.....	41
2.3.1 OH airglow emission layer.....	41
2.3.2 OH airglow imager.....	43
2.3.3 OH airglow image processing.....	44
Chapter 3: Gravity wave theory in the middle atmosphere.....	50
3.1 Air parcel model.....	51
3.2 Linear theory.....	53
3.3 Gravity wave ducting.....	59
3.4 Gravity wave instability and breaking.....	62
3.5 Gravity wave filtering.....	66
Chapter 4: Chapter 4: Measurement Results: Concentric gravity waves, mesospheric bores and large wind shears.....	69
4.1 Concentric gravity waves.....	70
4.1.1 Case study of 11 May 2004 concentric gravity waves.....	71
4.1.2 Convective sources.....	74
4.1.3 Analysis of CGWs using the gravity wave dispersion relation.....	78
4.1.4 Seasonal and background wind conditions and CGW observations...	83
4.1.5 Comparison between ray-tracing program and the observation.....	91
4.2 Mesospheric bores and large-scale gravity waves.....	93
4.2.1 Introduction to mesospheric bores.....	93
4.2.2 All-sky imager observations of bore formation from large-scale gravity waves.....	94
4.2.3 GW #4 steepening and bore excitation.....	101
4.2.4 Temperature inversion layer and GW trapping.....	104

4.2.5	Vertical motions induced by the mesospheric bores.....	111
4.2.6	Lower atmosphere origin of large-scale gravity waves.....	115
4.3	Large wind shears and convective stability.....	117
4.3.1	Lidar data analysis.....	119
4.3.2	Observation of large wind shears.....	120
4.3.3	Large wind shears and tidal waves.....	123
4.3.4	Correlation between large wind shear and Brunt-Vaisala frequenc...	127
Chapter 5: Conclusions and Future Work.....		144
5.1	Conclusions.....	144
5.2	Future work.....	150

## List of Figures

- Figure 1.1** A typical temperature and pressure vertical structure in the atmosphere from the ground to the thermosphere. The yellow line is the temperature profile. The black line to the right is the pressure profile. The various layers (troposphere, stratosphere, mesosphere and thermosphere) are labeled at corresponding heights.
- Figure 1.2** Na lidar observed temperature, zonal and meridional wind at 80-105 km. [Yuan et al., 2008]
- Figure 1.3** Zonal wind as a function of height in the midlatitude in winter and summer, adopted from Lindzen [1981]. The gravity wave spectrum is Gaussian distributed around zero phase speed. The shaded phase speed is filtered out by the mean wind. The thick arrow shows the wave drag force direction.
- Figure 1.4** Schematic of pole-to-pole meridional circulation caused by the balance of gravity wave forcing and the Coriolis force (the left panel) and the air sinking in winter and rising in summer [Holton and Alexander, 2000] (the right panel).
- Figure 2.1** Energy levels of atomic sodium  $D_2$  hyperfine transition (not to scale) [She et al., 1992].
- Figure 2.2** Sodium  $D_2$  fluorescence normalized spectrum (a) at zero radial wind and three temperatures (b) at a temperature of 200 K and three radial winds. The zero frequency is the center of mass frequency.
- Figure 2.3** Calibration curve for temperature and LOS wind from the measured lidar ratios.
- Figure 2.4** Schematic diagram of CSU Na lidar transmitter in 2009.
- Figure 2.5** Schematic diagram of single-pass sum-frequency generation (SFG). The lower right part with the Na cell is the Doppler-free spectroscopy.
- Figure 2.6** the Doppler-free saturation spectrum scanned by a solid-state single SFG module. The Lamb dip of  $D_{2a}$ ,  $D_{2b}$  and crossover feature between them is highlighted. The scanning step size is 0.001 V, corresponding to 2.5 MHz.
- Figure 2.7** Enlarged scan of  $D_{2a}$  Lamb dip. The scan step is 0.0005 V.
- Figure 2.8** Schematic of AOM used in the current CSU lidar system. The three blocks illustrate three beam paths for  $\nu_0$ ,  $\nu_0+630$  MHz,  $\nu_0-630$  MHz, respectively [Sherman, 1999].
- Figure 2.9** Lineshape function of the PDA output pulse calibrated in 2007. The peak of the pulse is zoomed in to show more clearly a negative shift of several MHz.

**Figure 2.10** Iodine transmission measured by the CW ring dye laser in 2007. The locations of the three operating lidar frequencies are denoted.

**Figure 2.11** The current receiver system of CSU Na lidar.

**Figure 2.12** Normalized transmission function of Faraday vapor filter measured on September 29, 2008. The “0” frequency is the center of mass of the D2 transition (589.158 nm). The oven and the tip temperatures are 168 and 145 °C. The magnetic field is 1750 Gauss. The length of the sodium cell is 40 mm.

**Figure 2.13** Diagram of CSU Na lidar electronics.

**Figure 2.14** Waveform diagram of the current lidar system signals showing corresponding period and pulsewidth. The numbers on the left are the designated BNC cable numbers.

**Figure 2.15** The nightglow spectrum from the visible to the infrared regions observed on the ground, not including all OH emission spectrum, which extended to ~4400 nm.  
[Johnson and Broadfoot, 1993].

**Figure 2.16** Schematic diagram of the Yucca Ridge OH imager [Fukushima, 2004].

**Figure 2.17** An example of an OH imager raw image taken at 0310 UT on October 07, 2005.

**Figure 2.18** The difference image at the flat field for Figure 2.17.

**Figure 3.1** Air parcel oscillation scheme. Heavy arrow: oscillation path, light arrow: force vector, dashed lines: isentropic lines, solid line: wave front.

**Figure 3.2** Upward-propagating gravity wave phase front and vectors.

**Figure 3.3** Forms of upward propagating gravity waves in the Na lidar and airglow imager data. The gravity wave parameters are included.  $\tau$  is the period.

**Figure 3.4** Schematic of the gravity wave reflection at the interface of different value of  $N$ .  $\beta_1$ : incident angle,  $\beta_2$ : refraction angle.

**Figure 3.5** Schematic of the second harmonic standing wave. The depth of the duct is  $3 \times 0.5\lambda_z$ .

**Figure 3.6** Schematic of the amplitude growth with height and saturation of a gravity wave due to convective instability [Fritts, 1984]. Wave damping produces both a divergence of the vertical flux of horizontal momentum and an acceleration of the

mean flow toward the phase speed of the wave on the right. Deceleration and diffusion cease at the critical level ( $z = z_c$ ) in linear theory.

**Figure 3.7** When a gravity wave approaches the critical level,  $w' \rightarrow 0$  and  $\lambda z \rightarrow 0$  [Nappo, 2002, pp121].

**Figure 4.1** Time sequence of difference OH images in geographic coordinates from 0340 to 0500 UT on 11 May 2004 covering parts of Wyoming, Nebraska, Colorado and Kansas. The top left graph shows the state borders in yellow dashed lines. The red star denotes the location of the OH imager at Yucca Ridge Field Station. The UT time of each image is shown the upper right corner. Longitudes and latitudes are shown on the right and lower axes, respectively. The red and blue dashed circles denote CGW1 and CGW2, respectively, with estimated centers shown as red and blue solid dots.

**Figure 4.2** CGW OH images from eight nights. Upper row (from left to right) shows the nights of 28 August 2005, 07 September 2005, 08 September 2005, and 04 May 2007, respectively. The lower row (from left to right) shows the nights of 03 June 2008, 26 August 2008, 30 August 2008, and 04 September 2008, respectively.

**Figure 4.3** (a) and (b): NEXRAD reflectivity charts observed at Goodland, KS, at 0305 UT, on 11 May 2004, at elevation angles of  $4.13^\circ$  and  $5.14^\circ$ , respectively. (c): NEXRAD echo top height chart, also from Goodland, KS, at 0305 UT. Centers of the red and white circles are the locations of plume1 and plume 2, respectively. The altitudes of plume1 and plume2 are 12 km and 14 km, as determined from the distances and elevation angles in (b) and (a), respectively. The colors in the reflectivity charts (a) and (b) indicate reflectivity in dBZ, and those in the echo-top chart (c) indicate altitude in km.

**Figure 4.4** NEXRAD reflectivity maps recorded on the same nights on which CGWs were observed, as shown in Fig. 4.2. Some of the arcs and rings of CGWs in Fig.4.2 are projected onto the radar maps.

**Figure 4.5** Temporal and spatial variations of CGW1 observed on 11 May 2004. (a) Observed wave periods (dots) compared to those calculated using dispersion relations (solid curve) as a function of radius: blue and red dots are the measured periods at 0400 UT and 0420 UT, respectively. (b) Horizontal wavelength  $\lambda_h$  as a function of both radius and time: dots are measured values. Blue, red and green curves are calculated from the GW dispersion relation for propagation times,  $\Delta t$  of 45, 55 and 85 min, respectively, between when the convective plume is generated near the tropopause and when CGWs were observed by the OH imager.

**Figure 4.6** (a) Monthly distribution of clear observation nights of the OH imager from 2003-2008. (b) Monthly distribution of CGW observations during the same period.

**Figure 4.7** TIME-GCM zonal-mean horizontal wind climatology at 42° N for 2004. (a) Zonal wind (b) Meridional wind (c) Total horizontal wind speed.

**Figure 4.8** (a) Radiosonde wind (0-30 km) and (b) TIME-GCM wind (30-90 km) both at 0 UT on the night of 11 May 2004. The height of the tropopause is marked by a green line in (a). The minimum horizontal phase speed of the CGWs is labeled.

**Figure 4.9** Radiosonde wind profiles as Figure 4.8(a) at 0UT on the nights of CGW observations on (a) 28 August 2005 (b) 07 September 2005 (c) 08 September 2005 (d) 04 May 2007 (e) 03 June 2008 (f) 26 August 2008. Profiles at Denver/Stapleton Station (39.75°N, 104.87°W), the closest to YRFS, are unavailable for 30 August and 04 September 2008.

**Figure 4.10** (left) Model results for zero winds. (right) Model results for the April zonal winds. (a, b) Model average vertical wavelengths at  $t = 55$  min. (c, d) Model average horizontal wavelengths at  $t = 45, 55,$  and  $85$  min as solid, dashed, and dash-dotted lines, respectively. Data at 0350, 0400, and 0430 UT are shown as diamonds, triangles, and squares, respectively [Yue et al., 2009]. (e, f) Model average ground based wave periods at  $t = 55$  min (dashed lines). Data at 0400 UT (diamonds). (g, h) Model temperature perturbations  $T_0/T$  (in %) at  $t = 55$  min along a line 45° to the northwest of the convective plume (solid lines). Inferred values of  $T_0/T$  (from the data shown in Figure 1b) at 0400 UT (dashed lines). [Vadas et al., 2009]

**Figure 4.11** Flat-fielded OH images in a sequence of UT times (on the top of each image) on 09 Oct 2007. Each image is normalized by the background during the entire night before being projected onto a geographic coordinate with the size of 600km×600km. Maximum positive and negative values are shown as light and dark shading, respectively, in the scale of  $\pm 30\%$ . The yellow and red dashed lines mark the front of GW #3 and #4, respectively. The blue arrows show the propagation direction of the waves. The narrow bright feature extending from the lower left corner to the center of the images is the Milky Way.

**Figure 4.12** same as Figure 4.11, except each image is the difference between two consecutive raw images.

**Figure 4.13** Sequence of the OH emission normalized perturbations along the propagating direction of GW #4. The X-axis is the geographic distance from the right lower corner of Figures 4.11 and 4.12 in the scale of 0-500 km. The scale of the y-axis is  $\pm 20\%$ . The dashed line is a sinusoidal wave with 193 km horizontal wavelength and 36 m/s velocity. The blue straight line indicates zero perturbation ( $y=0$ ).

- Figure 4.14** Sodium lidar measurement of the mesopause region on 09 Oct 2007. (a) Temperature in K (b) squared Brunt-Vaisala Frequency in  $10^{-4} \text{ s}^{-2}$ .
- Figure 4.15** Sodium lidar measurements of the mesopause region on 09 Oct 2007. (a) Wind velocity ( $\text{ms}^{-1}$ ) in the GW #4 direction (b) squared vertical wavenumber for GW #4 in  $\text{km}^{-2}$ .
- Figure 4.16** (a) Mean state and tidal component reconstructed temperature contour, (b) residue temperature after Mean state and tidal component being removed.
- Figure 4.17** Potential temperature on Oct 09 2007 measured by the east beam. The white arrow indicates the time when the bright front of GW #4 with a large perturbation passed the beam.
- Figure 4.18** Sodium density (in a unit of  $\text{cm}^{-3}$ ) contours measured by CSU sodium lidar on 09 Oct 2007 by the east (a), north (b) and west (c) beams. The temporal spatial resolution is 5 min.
- Figure 4.19** Weather maps at (a) 22 UT, 8 October 2007 (b) 00 UT, 7 October 2002 (c) 00 UT, 29 October 2003 (d) 00 UT, 19 October 2006.
- Figure 4.20** Superposition of the total wind shear magnitude profiles in 2002-2005 with (a) 15 min average time (b) 1 hour average time.
- Figure 4.21** Superposition of wind shears measured by rocket chemical release experiments for four decades [Larsen, 2002].
- Figure 4.22** Lidar data on May 14 2003. (a) zonal wind ( $\text{ms}^{-1}$ ), (b) meridional wind ( $\text{ms}^{-1}$ ), (c) wind shear ( $\text{ms}^{-1}\text{km}^{-1}$ ). Column (from left to right): Raw data, mean state and tides only. The color scale is the same for the left and right column.
- Figure 4.23** The local time dependence of (a) large total wind shear ( $> 40 \text{ ms}^{-1}\text{km}^{-1}$ ) (b) large amplitude of zonal and meridional wind shears ( $> 30 \text{ ms}^{-1}\text{km}^{-1}$ ) at 95-100 km in winter.
- Figure 4.24** Brunt-Vaisala frequency square versus wind shear in summer with 15 min integration time and 2 km vertical resolution at the altitude of (a) 85-90 km (b) 90-95 km (c) 95-100 km. The blue cross indicates the averaged measurement uncertainty.
- Figure 4.25** Brunt-Vaisala frequency square versus wind shear in winter with 15 min integration time and 2 km resolution at the altitude of (a) 80-85 km (b) 85-90 km (c) 90-95 km (d) 95-100 km (e) 100-105 km.
- Figure 4.26** Brunt-Vaisala frequency square versus wind shear in summer with 1 hour integral time and 2 km vertical resolution at the altitude of (a) 85-90 km (b)

90-95 km (c) 95-100 km. The blue cross indicates the averaged measurement uncertainty.

**Figure 4.27** Brunt-Vaisala frequency square versus wind shear in winter with 1 hour integral and 2 km resolution at the altitude of (a) 80-85 km (b) 85-90 km (c) 90-95 km (d) 95-100 km (e) 100-105 km.

**Figure 4.28** Maximum allowed wind shear  $S_{\max}$  in summer (red) and winter (blue).

**Figure 4.29** Superposition of the total wind shear magnitude profiles in 2002-2005 with 15 min average time in (a) winter and (b) summer.

**Figure 4.30** Semidiurnal tide amplitude of (a) zonal and (b) meridional wind at 80-105 km.

### List of Tables

**Table 2.1** Relative frequencies and line strengths of sodium  $D_2$  lines.

**Table 4.1** List of gravity waves discussed in Chapter 4.

## **Chapter 1: Introduction**

The earth's atmosphere not only provides a sustainable environment for humans, animals and plants, but it also connects earth to space. It is vital for humans to understand the characteristics and perturbations of the atmosphere. Entering the 21<sup>st</sup> century, the human race faces crises such as global warming and environmental degradation. As academics, it is our responsibility to study the atmosphere as a whole to understand these critical issues.

The lower atmosphere has been continuously and intensely studied for centuries because it is closely related to the daily life of humans and it is easier to measure than higher layers are. For the past few decades, the development of the modern technology allowed people to study the upper part of the atmosphere, for example, using radio-wave and optical remote sensing, rockets and satellites. Recent discoveries using these new techniques marked the start of a new era of atmospheric science and space physics. We can now study the atmosphere as a complete system, from the earth's surface to the outer atmosphere.

This dissertation is focused on study of the dynamics of the mesopause region (80-105 km), an important and often mysterious portion of the upper atmosphere, based on the observation of two optical remote sensing instruments: sodium (Na) Doppler lidar and OH nightglow imager. The altitude range measured by both methods is the mesopause region. Three individual but related scientific phenomena involving

atmospheric gravity waves in the mesopause will be addressed: mesospheric bores, large wind shears and concentric gravity waves. These studies have revealed novel scientific results and enhanced the understanding of those phenomena.

In this introductory chapter, we will first review the structure of the earth's atmosphere, focusing on the vertical temperature profile. Then we will introduce the role of gravity waves in determining the general circulation and fundamental structure of the middle atmosphere. This chapter concludes with a description of the structure of this dissertation.

## 1.1 Earth's atmosphere

### 1.1.1 Introduction to the Earth's atmosphere

The Earth's atmosphere is a mixture of gases surrounding the planet earth. It is retained by the earth's gravity. Molecular nitrogen and molecular oxygen dominate the composition of the air. Some minor species, such as water vapor, ozone and carbon dioxide, are also important because they drive atmospheric dynamics and chemistry. The dynamic behavior of the atmosphere is characterized by the following variables: temperature  $T$ , air density  $\rho$  and pressure  $p$ , and wind  $U$ .  $T$ ,  $\rho$  and  $p$  are related by the ideal gas law:

$$p = \rho \frac{R^*}{M} T = \rho R T \quad (1.1)$$

where  $R^*$  and  $R$  are the gas constant ( $8.314472 \text{ JK}^{-1}\text{mol}^{-1}$ ) and gas constant per unit mass ( $287 \text{ JK}^{-1}\text{kg}^{-1}$ ),  $M$  is the molar mass ( $28.97$  for the dry air). These variables are functions of space (zonal, meridional and vertical) and time. For the entire atmosphere at rest, the zero net vertical force on an air parcel comes from the balance of the force due to

gravity by a vertical pressure gradient force. The balance of these two forces is called hydrostatic equilibrium.

$$\frac{dp}{dz} = -g\rho \tag{1.2}$$

where  $g$  is the acceleration due to the earth's gravity. By integrating (1.2) for an isothermal atmosphere and inserting (1.1), this balance gives a pressure which decays exponentially with height where the pressure at the earth's surface is  $p_0$ .

$$p = p_0 e^{-z/H} \tag{1.3}$$

Here  $H=R*T_0/g$  is the scale height. In the same way, the density also falls exponentially from the surface. Figure 1.1 illustrates the layers of the atmosphere and their temperature and pressure characteristics. The black line on the right side shows the falling pressure as a function of height.

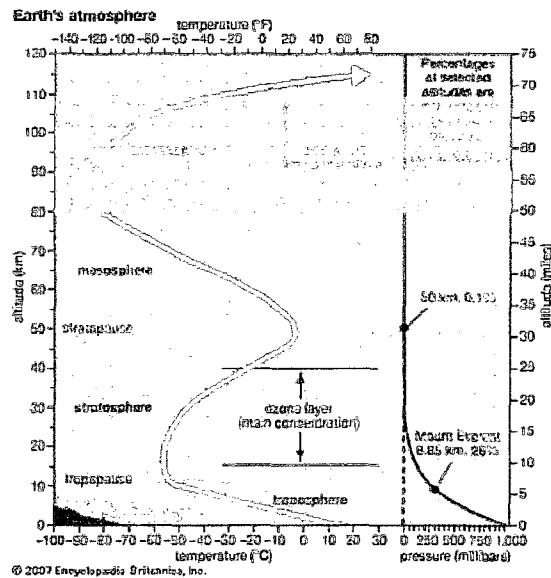


Figure 1.1 A typical temperature and pressure vertical structure in the atmosphere from the ground to the thermosphere. The yellow line is the temperature profile. The black line to the right is the pressure profile. The various layers (troposphere, stratosphere, mesosphere and thermosphere) are labeled at corresponding heights.

The temperature structure is more complicated than that of the pressure. The atmosphere is divided into four layers from the ground to the upper atmosphere by the change of the temperature gradients: troposphere, stratosphere, mesosphere and thermosphere, respectively. Here, we introduce them individually.

The troposphere lies between the surface and the tropopause (~10 -16 km), where the temperature is a local minimum. Solar radiation is absorbed mostly by the surface, and the temperature decreases with height. The troposphere contains most of the water vapor and aerosols. All the day-to-day weather occurs in this layer, including deep convection and the transport of frontal/jet systems. These weather systems are able to excite atmospheric gravity waves, which are the main focus of this dissertation. We will introduce gravity waves in the next section.

The stratosphere extends from the tropopause (~ 10 - 16 km) to the stratopause (~50 km) where the temperature is a local maximum. The temperature gradient is positive in this region because of the existence of the ozone layer (see Figure 1.1). The absorption of solar ultraviolet radiation by the ozone layer is responsible for the temperature increase. With a warm layer above and a cooler layer below, the stratosphere is highly stratified and stable. Atmospheric waves can be supported in such a stable region, which will be discussed in Chapter 4.

The mesosphere ranges from the stratopause (~ 50 km) to the mesopause (~ 85 km in summer and ~100 km in winter)) where the temperature is again at a local minimum. With little absorption of solar radiation in this region, the temperature decreases with height. Most meteors burn up here and deposit meteor dust. This residual

meteor dust (Na, K, Fe, etc.) allows the possibility of using laser-induced fluorescence lidar to probe this region.

Above ~ 85 km in summer and ~ 100 km in winter is the thermosphere with increasing temperature due to absorption of solar ultraviolet radiation which causes ionization of nitrogen and oxygen. Because the atmosphere is so thin, free electrons can exist for a relatively long time before being captured by positive ions. The E and F regions of the ionosphere overlap with the thermosphere. The interaction between neutral dynamics and the electromagnetic dynamics makes this region quite different from the layers below. It influences terrestrial radio and satellite communications.

### **1.1.2 Mesopause dynamics**

Between the mesosphere and thermosphere, the mesopause is at ~ 80-105 km. This region poses special interests. For example, the mesopause is the coldest part of earth's atmosphere with temperatures as cold as -100 °C. The mesopause also separates the homosphere (where the chemical constituents are well mixed and have identical mixing ratio) from the heterosphere (where the chemical constituents have different variations with height). It has been one of the least understood regions on the earth because very few modern probing methods reach there. The mesopause height displays seasonal variations in the midlatitudes, from ~85 km in summer to ~ 100 km in winter [She and Von Zahn, 1998]. The mesopause shows a seasonal temperature variability departure from the radiative equilibrium. Figure 1.2 shows the climatology of the temperature at 80-105 km measured by the CSU Na lidar from May 2002 to April 2006 [Yuan et al., 2008]. It is clear that the temperature is colder in summer and warmer in

winter from 80 to 90 km altitude. The zonal (eastward) wind is switching directions near the equinoxes and the meridional (northward) circulation is always from the summer hemisphere to the winter hemisphere. The only theory to explain these counter-intuitive behaviors is based on gravity wave dissipation that occurs in the mesopause.

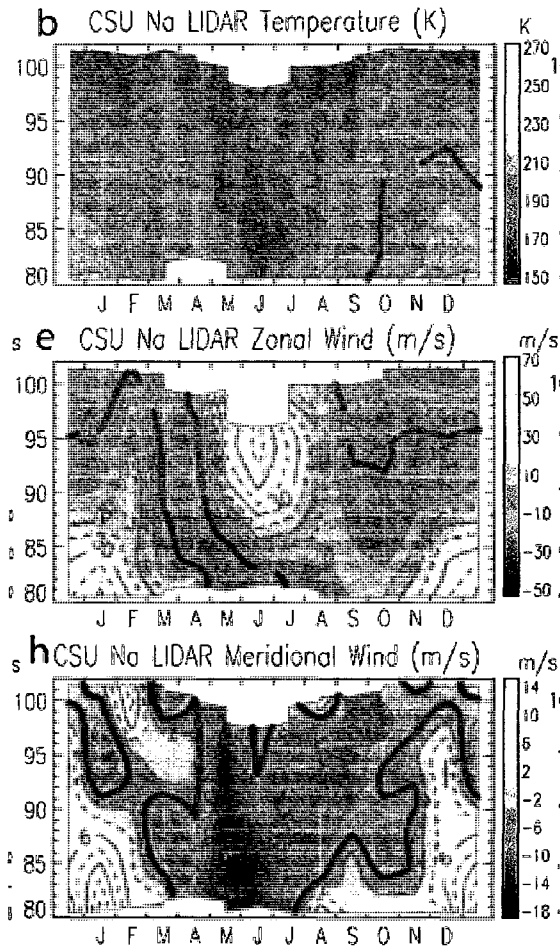


Figure 1.2 Na lidar observed temperature, zonal and meridional wind at 80-105 km. [Yuan et al., 2008]

Basically, atmospheric gravity waves are fluid-dynamical waves, supported by the buoyancy restoring effect in a stably stratified atmosphere [Andrews, 2000]. The theory of gravity waves will be discussed in depth in Chapter 3, and the observed phenomena

related to gravity waves will be presented in Chapter 4. All we need to know here is that gravity waves are generated in the lower atmosphere. They are fluctuations of temperature, air density, wind and pressure. Their horizontal wavelength can be as small as a few kilometers (internal gravity waves) or as long as thousands of kilometers (inertia gravity waves). Their period ranges from several minutes to hours. The gravity waves may propagate upward into the mesosphere and transport momentum and energy from the lower atmosphere. When waves break, they deposit their momentum flux and provide the necessary drag force to change the zonal wind direction. Propagating gravity waves can be filtered (prevented from propagating further upward) when the wave phase velocity is less than the mean wind velocity. The theory of gravity wave filtering will be reviewed in Section 3.5. The impact of wave filtering on the observation of concentric gravity waves in the mesopause will be discussed in Section 4.3. Figure 1.3 suggests that due to the mean wind filtering, gravity waves break in the upper thermosphere with phase velocity in opposite zonal directions in winter and summer. Therefore, they deposit momentum in different directions and exerts opposite drag force on the mean wind between summer and winter. In steady state, the zonal drag force due to the wave breaking is balanced by the Coriolis force. The Coriolis force is an apparent force on moving objects when they are viewed from a rotating reference frame and it is to the right of the direction of motion in the Northern Hemisphere and to the left in the Southern Hemisphere. The gravity wave induced zonal force and the associated balance induces a meridional flow from the summer pole to winter pole, as shown in Figure 1.4. Through mass continuity, this meridional circulation drives vertical air motion of rising in the summer polar region and sinking in the winter polar region. The sinking air causes

adiabatic heating in winter and the rising air induces adiabatic cooling in summer. Because there is no other major heating source in the mesopause, this provides a mesopause temperature structure of cold summer and warm winter, as observed by the Na lidar and shown in Figure 1.2.

Therefore, gravity waves play a fundamental role in the dynamics of the middle atmosphere. It has also been discovered recently that gravity waves may greatly impact the electrodynamics of the ionosphere. Although most of the gravity waves are in the middle atmosphere, there are secondary gravity waves generated by the wave breaking and there are the small-amplitude fast-velocity gravity waves which may reach altitudes of  $\sim 300$  km. The amplitude of these gravity waves becomes very large in the thermosphere. They are capable of modulating the electron density in the ionosphere and seeding plasma bubbles. These phenomena are critical for global radio communications.

Even though gravity waves play a vital role in atmosphere dynamics, people just began to observe and simulate them in the past few decades. Optical remote sensing tools with high enough spatial and temporal resolution, like the Na Doppler lidar and the OH airglow imager used in this dissertation, help to advance one's understanding of the gravity waves in the mesopause region. The more we know about the spectrum and evolution of the gravity waves, the more accurately we are able to simulate the middle atmosphere. The study of gravity wave breaking and propagation also has the potential to forecast the outage of radiowave communications in the ionosphere.

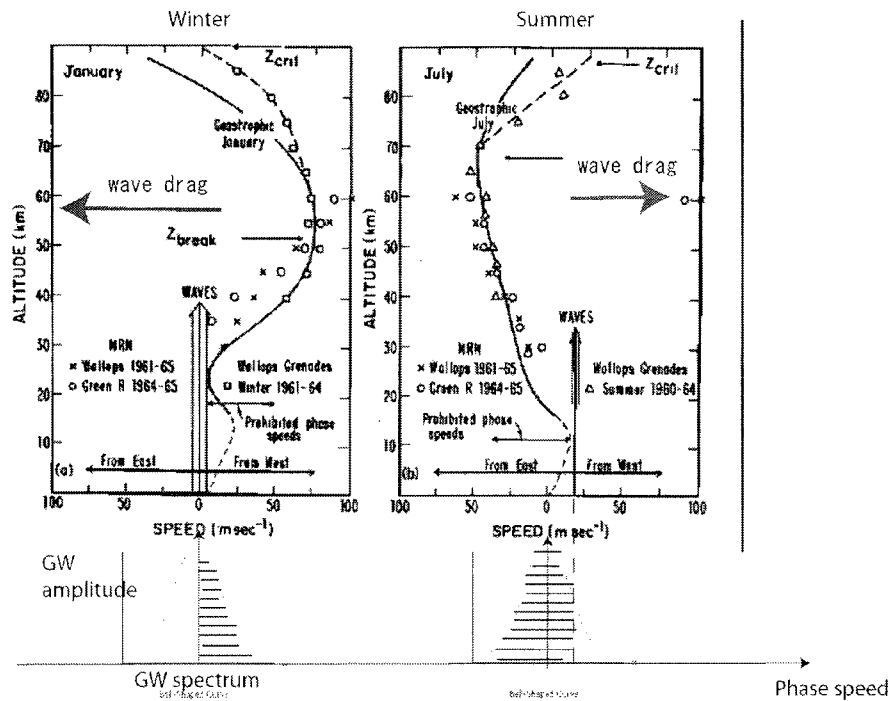


Figure 1.3 Zonal wind as a function of height in the midlatitude in winter and summer, adopted from Lindzen [1981]. The gravity wave spectrum is Gaussian distributed around zero phase speed. The shaded phase speed is filtered out by the mean wind. The thick arrow shows the wave drag force direction.

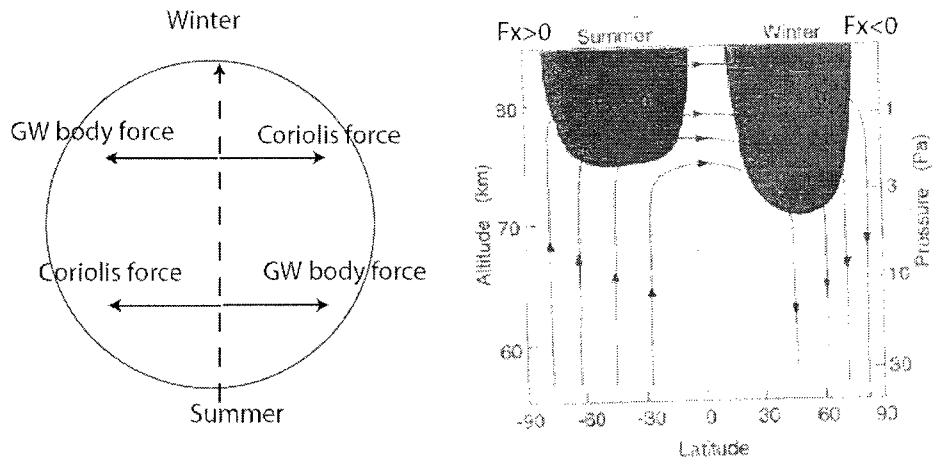


Figure 1.4. Schematic of pole-to-pole meridional circulation caused by the balance of gravity wave forcing and the Coriolis force (the left panel) and the air sinking in winter and rising in summer [Holton and Alexander, 2000] (the right panel).

## 1.2 Structure of dissertation

Chapter 2 first introduces basic sodium lidar theory and its corresponding sodium spectroscopy. The details of the current CSU sodium lidar system setup are discussed. This includes the lidar transmitter, receiver, and electronics subsystem. Newly developed or reported subsystems are emphasized. The nearby Kyoto University OH imager at Fort Collins is also briefly introduced at the end of this chapter.

Chapter 3 reviews linear gravity wave theory, establishing a basis for the discussion of results in the following Chapter. This chapter covers a number of aspects of gravity waves: characteristics derived from the linear theory, wave ducting, wave instability and breaking and wave filtering by the mean wind.

Chapter 4 describes results of observations using the data from the CSU Na lidar and the OH imager. The gravity wave theories introduced in Chapter 3 will be employed here to explain the observational results. The first section of Chapter 4 discusses concentric gravity waves observed by the airglow imager. The tropospheric origin of the waves is discussed. The observed waves are compared to the gravity wave dispersion relation and the ray-tracing program results in Vadas et al. [2009]. The second section considers mesospheric bores and their evolution from large-scale gravity waves. The impact of mesospheric bores on the mean state and the source of the large-scale gravity waves are also discussed. The third section focuses on the large wind shears observed by the Na lidar. The large wind shear and its relation to the convective stability and semidiurnal tides are presented.

Chapter 5 draws the conclusions of this work and shares a view of the future work.

## References:

- Andrews, D. G., An introduction to atmospheric physics, Cambridge University Press, 2000.
- Lindzen, R. S., Turbulence and Stress owing to gravity wave and tidal breakdown, *J. Geophys. Res.*, 86(C10), 9707-9714, 1981.
- Holton, J. R., The Influence of Gravity Wave Breaking on the General Circulation of the Middle Atmosphere, *J. Atmos. Sci.*, 40(10), 2497-2507, 1983.
- Holton, J. R. and J. Alexander, The role of waves in the transport circulation of the middle atmosphere, *Geophys. Monograph 123*, 21-35, 2000.
- She, C. Y. and U. von Zahn, The concept of two-level mesopause: Support through new lidar observation, *J. Geophys. Res.*, 103, 5855 - 5863, 1998
- Vadas S., J. Yue, C.-Y. She, P. Stamus and A. Z. Liu, A model study of the effects of winds on concentric rings of gravity waves from a convective plume near Fort Collins on 11 May 2004, *J. Geophys. Res.*, doi:10.1029/2008JD010753, 2009.
- Yuan T., C.-Y. She, D. A. Krueger, F. Sassi, R. Garcia, R. G. Roble, H.-L. Liu, H. Schmidt, Climatology of mesopause region temperature, zonal wind, and meridional wind over Fort Collins, Colorado (41°N, 105°W), and comparison with model simulations, *J. Geophys. Res.*, 113, D03105, doi:10.1029/2007JD008697, 2008.

## **Chapter 2: Colorado State University Sodium Lidar System and Kyoto University**

### **OH all-sky imager**

The Colorado State University sodium lidar system at Fort Collins, Colorado (41°N, 105°W) has been in operation to monitor the temperature and dynamics of the mesopause (80-105 km) region of the atmosphere since August 1989 [She and Krueger, 2007]. With years of persistent effort, continuing efforts have improved its performance and science capabilities. The science capability expanded from only temperature measurement using two laser frequencies to simultaneous temperature and horizontal wind measurements using three frequencies [White, 1999]. Full-diurnal cycle observing capability replaced the nighttime-only measurement with the advent of Faraday filters to block the sunlight noise [Chen, 1997; Chen, 1999; Yuan, 2004]. The lidar system was upgraded from one beam to two beams for simultaneous zonal and meridional wind measurements, and further upgraded to three beams enabling the measurement of the vertical flux of the gravity wave horizontal momentum [Acott, 2009]. The system is operating in a campaign mode at three frequencies with a three-beam setup in winter and a two-beam setup in summer to simultaneously monitor neutral temperature, and zonal and meridional winds in the mesopause region on 24-hour continuous basis. Flux of horizontal momentum is measured in winter.

As a tradition of every graduate student's dissertation from this group, a detailed description of the current lidar system will be briefly presented in this chapter. It reflects the student's understanding and vision of a sodium lidar system. A subsystem developed here, the sum-frequency generated seeder by a periodically poled lithium niobate (PPLN), will also be introduced, although it is not part of the CSU lidar system. It is currently deployed by our colleagues in the Weber lidar system at the Arctic Lidar Observatory for Middle Atmosphere Research (ALOMAR), Andoya, Norway and the Shinshu/Nagoya University all-solid-state sodium lidar system under construction.

## **2.1 Fundamental Theory of Sodium Temperature and Wind Lidar**

### **2.1.1 Sodium D<sub>2</sub> transition and fluorescence**

First, an introduction to the sodium lidar theory will be presented, i.e., how the CSU lidar is able to simultaneously measure the temperature and wind in the mesopause. More detailed description of the related quantum mechanics can be found in She et al. [1992], She and Yu [1995], and in the former PhD students' dissertations, especially Chen [1997], Chen [1999] and White [1999]. In general, the detection of temperature and wind is feasible because of a layer of atomic sodium in the altitude range of 80-105 km, deposited by meteors disintegrating as they enter the earth's atmosphere. The CSU sodium lidar system emits narrowband laser pulses at the sodium D<sub>2</sub> line of 589.158 nm and detects laser-induced fluorescence (LIF) from these sodium atoms. The temperature and line-of-sight (LOS) wind can be deduced from the Doppler broadened and shifted fluorescence spectrum. The whole process has been called a beautiful name: "spectroscopy in the sky" [She and Krueger, 2007].

Figure 2.1 shows the energy levels of the sodium D<sub>2</sub> hyperfine transition. The Na D<sub>2</sub> transition is between the ground state, <sup>2</sup>S<sub>1/2</sub>, and the excited state, <sup>2</sup>P<sub>3/2</sub>. Including the Na nuclear spin momentum splits the energy levels into hyperfine structure. The ground state <sup>2</sup>S<sub>1/2</sub> is split into two hyperfine levels separated by about 1.8 GHz. The excited state <sup>2</sup>P<sub>3/2</sub> is split into four hyperfine states within about 100 MHz. As a result, the Na D<sub>2</sub> transition is divided into two groups: D<sub>2a</sub> associated with the lower ground state (transitions 1, 2, and 3 in Figure 2.1) and D<sub>2b</sub> with the upper ground state (transitions 4, 5, and 6). The resonance frequencies  $\nu_n$  relative to the line center of mass and relative line strengths S<sub>n</sub> of these six transitions are listed in Table 2.1.

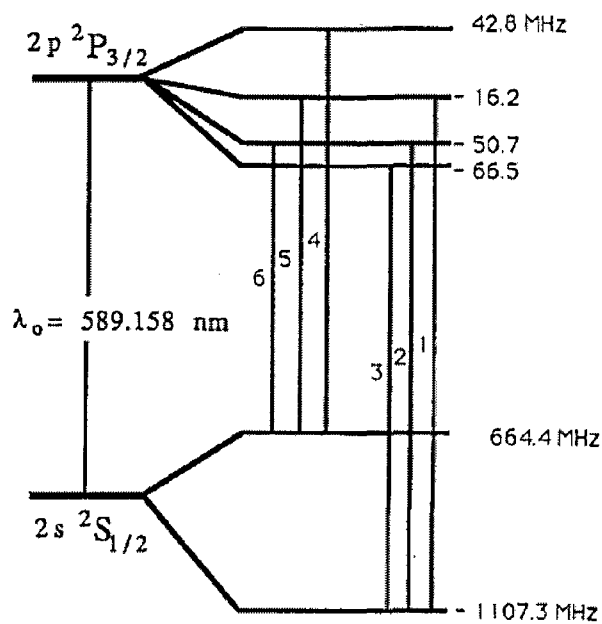


Figure 2.1 Energy levels of atomic sodium D<sub>2</sub> hyperfine transition (not to scale) [She et al., 1992].

Table 2.1 Relative frequencies and line strengths of sodium D<sub>2</sub> lines.

n	D <sub>2</sub> line name	$\nu_n$ (GHz)	$S_n$
1	D <sub>2b,0</sub>	1.0408	2/32
2	D <sub>2b,1</sub>	1.0566	5/32
3	D <sub>2b,2</sub>	1.0911	5/32
4	D <sub>2a,1</sub>	-0.7150	1/32
5	D <sub>2a,2</sub>	-0.6806	5/32
6	D <sub>2a,3</sub>	-0.6216	14/32

### 2.1.2 Doppler broadening and shifting of the sodium fluorescence spectrum

Although the transition includes six discrete lines, the fluorescence spectrum of the sodium D<sub>2</sub> transition is continuous as a result of line-broadening mechanisms. Among these mechanisms, Doppler broadening is dominant over natural broadening (resulting from finite emission lifetime) and pressure broadening [Yu, 1994].

Doppler broadening arises from the random thermal motion of sodium atoms. Atoms with different velocities relative to the incoming photons will have different transition frequencies because of the Doppler effect. Therefore, for the sodium atoms in equilibrium with the environment in the mesopause, the resonance band is Doppler broadened due to the speed distribution of sodium atoms, which is a function of the environmental temperature. For each sodium D<sub>2</sub> transition line, the fluorescence  $g(\nu)$  is [Theon et al., 1972]:

$$g_n(\nu) = S_n \left[ \frac{D}{\pi T} \right]^{\frac{1}{2}} \exp \left[ -\frac{D[\nu - \nu_n]^2}{T} \right] \quad (2.1)$$

Here,  $D$  is 497.6 K·(ns)<sup>2</sup>; the line strength  $S_n$  is given in Table 2.1;  $T$  is the temperature and  $\nu_n$  is the relative frequency, also in Table 2.1.

In addition to Doppler broadening due to random motion in the presence of wind, the center of mass of sodium atoms in the mesopause will have a collective velocity relative to incident photons. This introduces an overall Doppler shift of the fluorescence spectrum  $\Delta\nu = -V/\lambda_0$ , where  $V$  is the wind velocity toward the laser and  $\lambda_0 = 589.158$  nm is the wavelength of the sodium D<sub>2</sub> line. The fluorescence becomes:

$$g_n(\nu) = S_n \left[ \frac{D}{\pi T} \right]^{\frac{1}{2}} \exp \left[ - \frac{D \left[ \nu - \nu_n - \frac{V}{\lambda_0} \right]^2}{T} \right] \quad (2.2)$$

### 2.1.3 Sodium fluorescence spectrum: the basis of the CSU sodium lidar

The measurement of temperature  $T$  and radial wind  $V$  by the Na fluorescence lidar is possible because the Na fluorescence spectrum is a function of  $T$  and  $V$  ( 2.2). To calculate  $T$  and  $V$ , it is necessary to include all six transitions in the Na D<sub>2</sub> line and Doppler broadening/shifting. The sodium fluorescence spectrum at D<sub>2</sub> is then given as:

$$g(\nu) = \sum_{n=1}^6 g_n(\nu) = \left[ \frac{D}{\pi T} \right]^{\frac{1}{2}} \sum_{n=1}^6 S_n \exp \left[ - \frac{D \left[ \nu - \nu_n - \frac{V}{\lambda_0} \right]^2}{T} \right] \quad (2.3)$$

Several normalized fluorescence spectra of the sodium D<sub>2</sub> line are shown in Figure 2.2: (a) at zero wind but at different temperatures (b) at a constant temperature of 200 K but at different radial wind velocities. The chosen ranges of 150 - 250 K and -100 - 100 m/s for temperature and wind are representative of the normal background conditions in the mesopause [Yuan et al., 2008]. The spectrum is broadened as temperature increases from 150 K to 200 K and 200 K to 250 K, as shown in Figure 2.2(a); the spectrum is shifted to higher frequencies with a positive radial wind and shifted to lower frequencies with a negative radial wind, as shown in Figure 2.2(b).

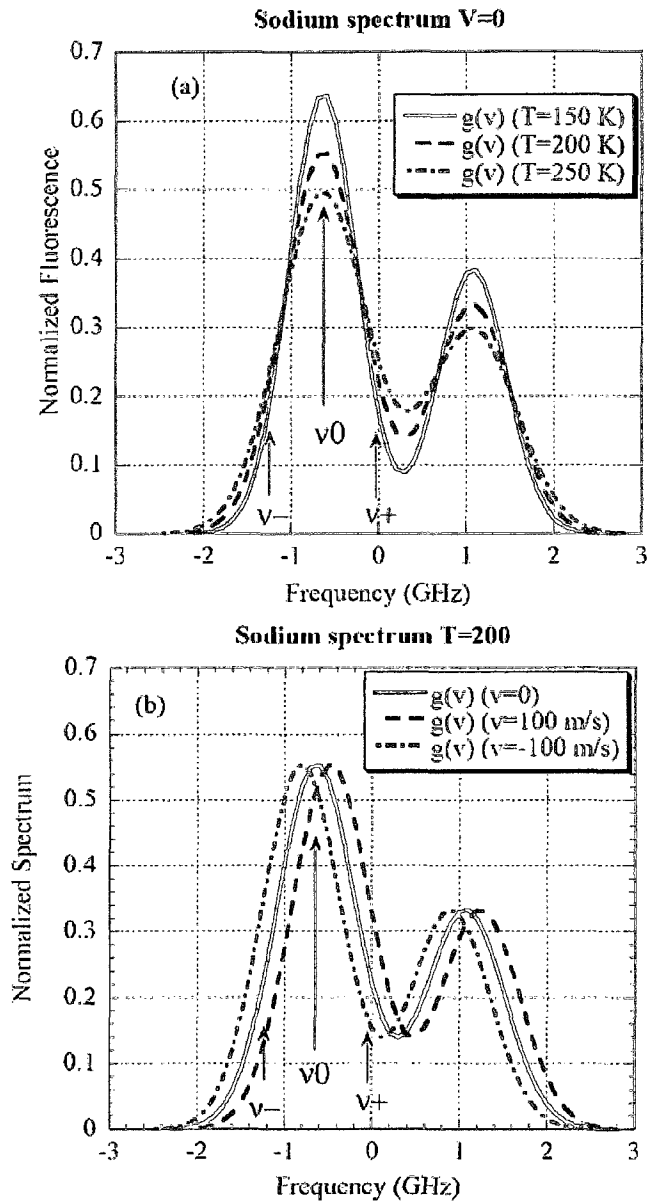


Figure 2.2 Sodium D<sub>2</sub> fluorescence normalized spectrum (a) at zero radial wind and three temperatures (b) at a temperature of 200 K and three radial winds. The zero frequency is the center of mass frequency.

To accurately determine the temperature broadening and Doppler shifting induced by the background temperature and wind fields, measurements at three frequencies are

necessary. One is located at the peak of the spectrum ( $\nu_0 = -0.656$  GHz in Figure 2.2)), two are on the shoulders ( $\nu_+ = -0.656 + 0.63$  GHz and  $\nu_- = -0.656 - 0.63$  GHz). The selection of these frequencies is discussed in White [1999]. The generation of laser beams at these three frequencies will be described in Section 2.2.

#### 2.1.4 Sodium lidar equation

Like other types of lidar [Measures, 1983], the theory of fluorescence lidar starts with the lidar equation. When a laser pulse is sent into the atmosphere, the pulse may be absorbed or scattered by aerosols, atoms and molecules. The backscattered light is collected by telescopes and detected by photodiodes or photomultiplier tubes (PMTs). The detected lidar signal is determined by the transmitted energy of the laser pulse, the absorption and backscattering properties in the sky, the distance between the lidar and the target, the area of the telescope and the sensitivity of the detector. For a lidar system with a collocated laser transmitter and receiver, the distance  $z$  between the lidar and the location where the backscattering occurs can be deduced from the time of flight  $\tau$  between the pulse emission time and the photon detection time by  $z = c \tau / 2$ . In this way, the range-resolved profile of the backscattering signal can be obtained.

For a sodium fluorescence lidar system, the lidar equation is written as:

$$N(z) = (\eta T_A^2) \left( \frac{E_L}{hc / \lambda_L} \right) (\rho(z) \Delta z \sigma_{sb}) \left( \frac{A_R}{z^2} \right) \exp[-2 \int_{z_L}^z \alpha(z') dz'] + N_B \quad (2.4)$$

where

$N(z)$  is the number of detected photons in the bin of  $(z - \Delta z / 2, z + \Delta z / 2)$  in range;

$\eta$  is the combined efficiency of the lidar system;

$T_A^2$  is the two-way transmittance between the ground and the bottom of the sodium layer;

$E_L$  is the energy of an emitted laser pulse (J);

$hc/\lambda_L$  is the energy of a single photon at  $\lambda_L$  ( $0.34 \times 10^{-18}$  J for the sodium lidar);

$\rho$  is the sodium number density ( $\text{m}^{-3}$ );

$\sigma_{sb}$  is the sodium differential backscattering cross section ( $\text{m}^2 \text{sr}^{-1}$ );

$\Delta z$  is the range bin size (m);

$A_R$  is the aperture area of the receiving telescope ( $\text{m}^2$ );

$\alpha = 4\pi\rho\sigma_{sb} = \rho\sigma_{sa}$  is the sodium extinction coefficient ( $\text{m}^{-1}$ ) and  $\sigma_{sa}$  is the total absorption cross section;

$\exp[-2 \int_{z_L}^z \alpha(z') dz']$  is the two-way transmittance in the sodium layer;

$N_B$  is the background noise and dark counts per range bin per pulse.

Equation (2.4) indicates that, to estimate the maximum photon counts  $N(z)$  a sodium lidar can achieve, one needs to consider all the attenuation factors of both transmitting and receiving photons including the passive and active transmittance of the lidar system and

the atmosphere transmission ( $T_A^2$ ), the total number of emitted photons ( $\frac{E_L}{hc/\lambda_L}$ ), the

probability of backscattering in a range bin  $\Delta z$  represented as ( $\rho(z)\Delta z\sigma_{sb}$ ), the ratio

between the total number of backscattered photons and the number of photons being

collected by the telescope ( $\frac{A_R}{z^2}$ ), as well as the transmittance in the sodium layer

$\exp[-2 \int_{z_L}^z \alpha(z') dz']$ .

The Na fluorescence spectrum of (2.3) is related to the total absorption cross section by [She et al., 1992]

$$\sigma_{sa} = (g_2 / g_1)(\lambda_0^2 / 8\pi)A_{21}g(\nu) \quad (2.5)$$

where  $(g_2/g_1)$  is the degeneracy ratio (equal to two for the  $D_2$  transition) and  $A_{21}$  is the Einstein coefficient ( $6.289 \times 10^7 \text{ s}^{-1}$ ). Combining (2.3)-(2.5), the number of detected photons is a function of temperature and wind.

### 2.1.5 Lidar temperature and wind ratios and calibration curve

As shown in Section 2.1.4, the actual returned lidar signal depends on many other factors in addition to the fluorescence. In order to deduce the temperature and radial wind information, it is more convenient to utilize the ratios between the signals at three frequencies rather than the absolute fluorescence.

After the background noise is subtracted, the first step is to normalize the sodium fluorescence counts with a Rayleigh scattered signal at 20-40 km range, far below the sodium layer, because the energy per pulse and the extinction are different for each frequency. The lidar equation for Rayleigh scattering by air molecules is:

$$N_R(z) = (\eta T_A^2) \left( \frac{E_L}{hc / \lambda_L} \right) (\rho_{air}(z) \Delta z \sigma_{Rb}) \left( \frac{A_R}{z^2} \right) + N_B \quad (2.6)$$

where the air density is  $\rho_{air}$ , and the Rayleigh backscattering cross section is  $\sigma_{Rb}$ .

For the CSU sodium lidar, sum and difference ratios are formed for the temperature and wind calculations, respectively:

$$R_T(T, V) = \frac{N_+ + N_-}{2N_0} = \frac{\sigma_{sb}^+(T, V) + \sigma_{sb}^-(T, V)}{2\sigma_{sb}^0(T, V)} \quad (2.7)$$

$$R_V(T, V) = \frac{N_+ - N_-}{N_0} = \frac{\sigma_{sb}^+(T, V) - \sigma_{sb}^-(T, V)}{\sigma_{sb}^0(T, V)} \quad (2.8)$$

Note that the photon counts at three frequencies,  $N_+$ ,  $N_-$  and  $N_0$ , are normalized by the Rayleigh signal at 20-40 km, to remove the effect of changing pulse energies and transmittances. The subscripts of 0, + and - denote the frequencies at  $\nu_0$ ,  $\nu_+ = \nu_0 + 0.63$  GHz and  $\nu_- = \nu_0 - 0.63$  GHz, respectively. The sodium fluorescence backscattering cross section  $\sigma_{sb}$  is a function of ambient temperature and line-of-sight (LOS) wind.  $R_T$  and  $R_V$  depend only on  $T$  and  $V$  in (2.7) and (2.8). In turn,  $T$  and  $V$  can be retrieved from  $R_T$  and  $R_V$  using (2.7) and (2.8). A look-up table is constructed by calculating the theoretical intensity ratios  $R_T$  and  $R_V$  from the temperature and LOS wind, as illustrated in Figure 2.3. The detailed derivation of the calibration table can be found in Li [2005]. Knowing the temperature and wind speed, the sodium total absorption cross section can be calculated from Eqn (2.5) and using the normalization between fluorescence and Rayleigh lidar equations (2.4) and (2.6), we can deduce the sodium density for three frequencies independently.

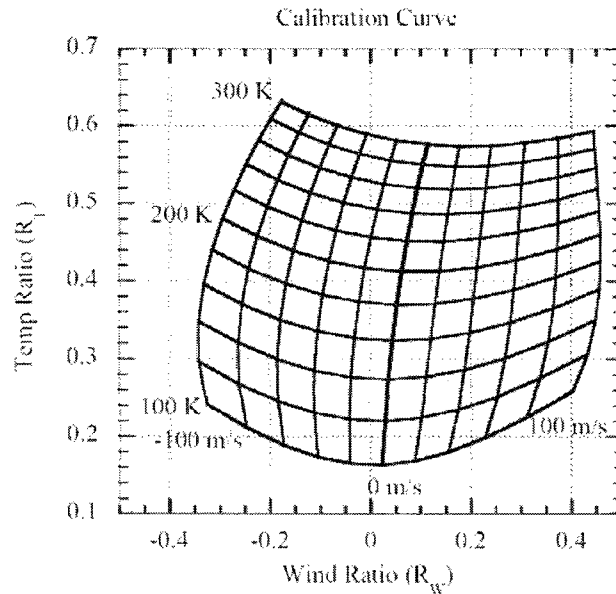


Figure 2.3 Calibration curve for temperature and LOS wind from the measured lidar ratios.

## 2.2 Sodium lidar system

The CSU Na lidar consists of three major subsystems: the transmitter, the receiver and the control. These three parts need to work seamlessly to achieve its versatile scientific capability.

### 2.2.1 Sodium lidar transmitter

As introduced in Section 2.1, to measure the temperature and LOS wind in the sodium layer, the lidar transmitter needs to provide narrow-band pulsed laser beams at the three frequencies mentioned above. To achieve this, the transmitter consists of three lasers (one CW Nd:YAG laser, one CW ring dye laser, and one pulsed Nd:YAG laser), one pulsed dye amplifier, a Doppler-free spectroscope, an Acoustic Optic Modulator and an iodine-filter based chirp monitor. Figure 2.4 gives the schematic of the current CSU lidar transmitter. The current system is the results of the efforts of dozens of people over almost two decades.

There are five important subsystems in the lidar transmitter: CW laser seed injector, Doppler-free spectroscopy, Acousto-Optic Modulator, Pulsed amplifier and Chirp Monitor subsystem (listed A-E). They are integrated by the necessary mirrors and lenses. We will briefly describe each subsystem below. With an eye toward the next-generation all-solid-state mobile Na lidar, we also discuss the proposed solid-state subsystem to replace the current dye lasers. This subsystem was tested at CSU.

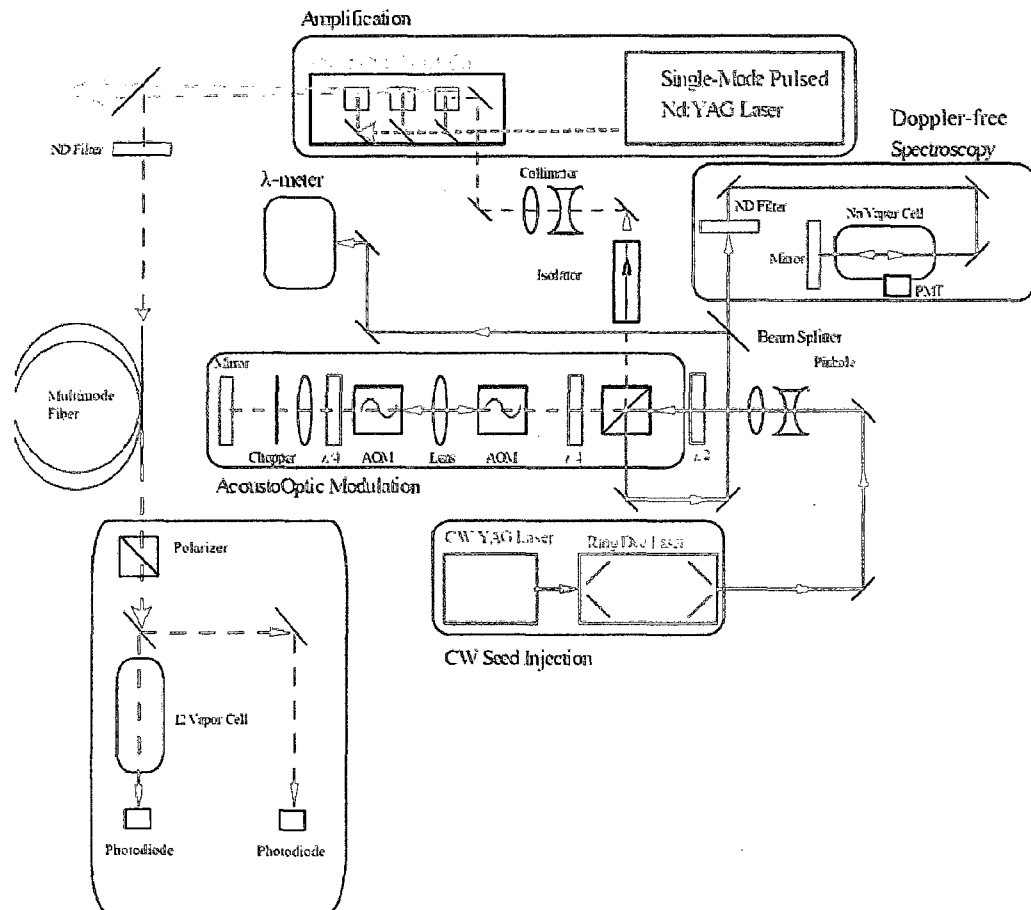


Figure 2.4 Schematic diagram of CSU Na lidar transmitter in 2009.

**A. CW seed injection:** The current CW seed injection system for the pulsed dye amplifier is composed of a CW Nd:YAG pump laser at 532 nm (Spectra Physics Millennia-V) and a CW Ring Dye laser (Coherent 899-21) at 589 nm. With 3.5-4 W of YAG laser pump power, the ring dye laser produces 300-500 mW of single-mode narrow-band CW light at the Na D<sub>2a</sub> peak with ~500 kHz bandwidth. To stabilize the frequency of the ring laser, a reference cavity provides an error signal; a Brewster plate and a PZT-mounted fold mirror (or tweezer) correct the frequency in real time.

The use of the liquid dye as the ring laser medium greatly limits the potential for the sodium lidar being transported and remotely deployed. This cannot meet the expanding scientific need of deploying fluorescence lidars at remote sites like the polar and tropical regions to collaborate with other instruments. Therefore, one needs to build a solid-state seeder to replace the ring laser. One promising approach is noncritical phase matching sum-frequency generation (SFG) with two single-mode CW Nd:YAG lasers at 1064 nm and 1319 nm. A number of different approaches have been demonstrated to achieve this. For example, 3.4 mW of 589 nm SFG radiation was generated with a congruent Lithium Niobate crystal in a single-pass scheme [Moosmuller and Vance, 1997], and 400 mW of SFG power was achieved with a doubly resonant congruent lithium niobate resonator [Vance et al., 1998]. A mobile narrow-band sodium fluorescence lidar [She et al., 2007] and related diagnostics require 5 – 10 mW of tunable CW light at 589 nm; a simple single-pass method is preferred for easier alignment. It should be noted that while the power generated by the congruent crystal in a single-pass scheme is not sufficient, resonant SFG systems inherit the resonator design, similar to ring dye lasers. They not only dramatically enhanced the output power, but also greatly

added to the complexity and cost of the system and required highly skilled operators to align them.

More efficient generation of narrow-band CW sodium resonance radiation has been demonstrated by a single-pass SFG using two CW Nd:YAG lasers (InnoLight Mephisto 1500 NE at 1064 nm and MIR 500 NE 1319 nm) with a Periodically Poled Lithium Niobate (PPLN) crystal. The advantage of a poled crystal is the fact that quasi-phase matching facilitated by periodic poling allows the use of the more efficient nonlinear coefficient  $d_{33}$  (~6 times larger than  $d_{31}$ ) for SFG in Lithium Niobate, while conventional phase matching with a non-poled crystal can never be achieved with  $d_{33}$ . With 0.8 W of 1064 nm and 0.35 W of 1319 nm light incident on the PPLN crystal, 11 mW output power at 589 nm has been demonstrated. This compact and maintenance-free nonlinear optical element has been utilized as the CW laser light in the Weber sodium wind-temperature lidar, located at the Arctic Lidar Observatory for Middle Atmosphere Research (ALOMAR) Range, Norway. It will also be used as the frequency marker in an all-solid-state mobile narrow-band sodium lidar under construction at Shinshu University/Nagoya University, Japan. A diagram of the single-pass SFG is given in Figure 2.5. The detailed experiment results are described in Yue et al. [2009]. In the future, with commercially available longer PPLN crystals (40 mm and longer) and high-power CW YAG lasers at 1064 nm with 15 W power (Innolight Mephisto MOPA) or 800 mW at 1319 nm, it may be feasible to generate more than 200 mW of the CW light at 589 nm. The power level is comparable to that of the ring dye laser used in the CSU sodium lidar system. Another alternative approach is to build a external doubly bow-tie cavity for the same infrared Nd:YAG lasers. About 0.8 W of CW power at the Na D<sub>2</sub> line has been

reported with this scheme for the purpose of laser cooling and trapping [Mimoun et al., 2009].

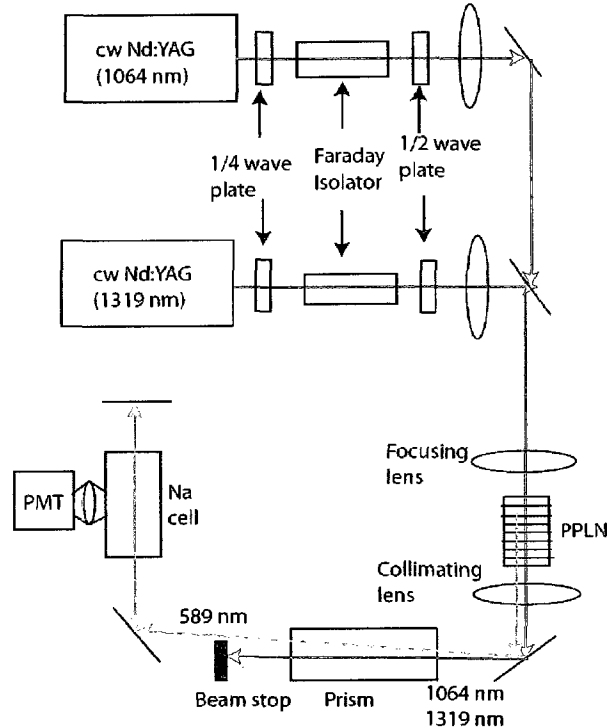


Figure 2.5 Schematic diagram of single-pass sum-frequency generation (SFG). The lower right part with the Na cell is the Doppler-free spectroscopy.

**B. Doppler-free saturation fluorescent spectroscopy:** As introduced in Section 2.1, the key to successfully measure the temperature and wind in the sodium layer with a lidar is to precisely control the laser frequency. For wind measurements, 1 MHz of frequency drift will cause an error of 0.6 m/s. Doppler-free spectroscopy is used based on a sodium vapor cell heated to 70-80 °C [She and Yu, 1995]. Its schematic diagram can be found in Figure 2.4 and 2.5. A small amount of light ( $\sim 100 \mu\text{W}$ ) is guided into the sodium vapor cell and reflected by a mirror at the other end. The incident and reflected beams need to be overlapped. A PMT is mounted adjacent to the side of the cell to collect

the sodium fluorescence light excited by the laser beam. For the LIF at the resonance frequencies of  $D_{2a}$  and  $D_{2b}$ , the group of “motion-free” Na atoms experience stronger saturation, leading to a signal reduction. One example of a Na Doppler-free spectrum scanned by a single-pass SFG is shown in Figure 2.6. The same spectrum scanned by the ring dye laser is included in most of the dissertations by former students in the group [Yu, 1995; Yuan, 2004]. The “crossover” peak in Figure 2.6 is generated because the light at frequencies between  $D_{2a}$  and  $D_{2b}$  can interact with two different groups of Na atoms with opposite velocities, resulting in weaker saturation and a slightly stronger signal. The enlarged spectrum at  $D_{2a}$  is given in Figure 2.7 scanned by the same single-pass SFG. The frequency  $\nu_0$  of the ring dye laser is chosen to be locked at the sharpest dip within 1-2 MHz with a lock-in amplifier (LIA). Other than Doppler-free Saturation Fluorescence spectroscopy, Doppler-free Saturation Absorption spectroscopy can also be used in sodium lidar systems [Smith et al., 2008].

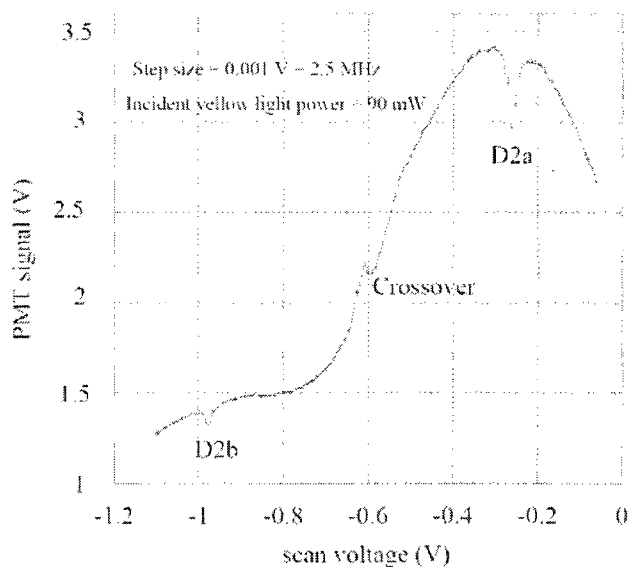


Figure 2.6 the Doppler-free saturation spectrum scanned by a solid-state single SFG module. The Lamb dip of  $D_{2a}$ ,  $D_{2b}$  and crossover feature between them is highlighted. The scanning step size is 0.001 V, corresponding to 2.5 MHz.

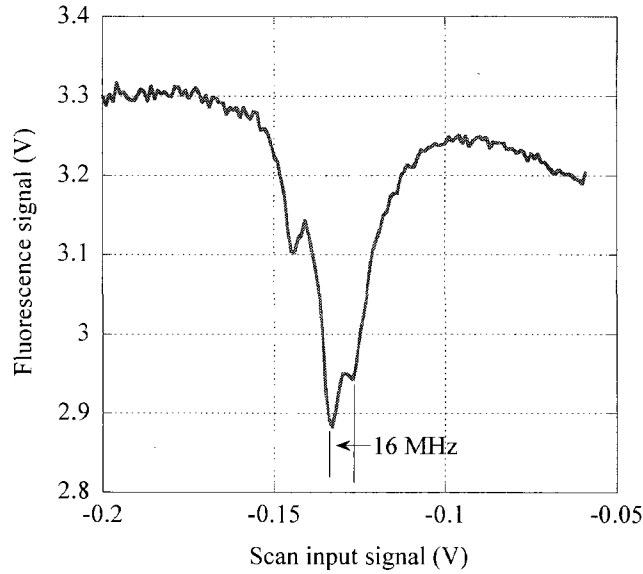


Figure 2.7 Enlarged scan of  $D_{2a}$  Lamb dip. The scan step is 0.0005 V.

**C. Acousto-Optic Modulator:** As discussed in Section 2.1.4, return signals at different frequencies are necessary to form ratios to obtain temperature and LOS wind. The dual-pass acousto-optic modulator (AOM) is employed in the system to shift the locked frequency  $\nu_0$  from the ring laser by +630 MHz or -630 MHz sequentially. Figure 2.8 shows the schematic diagram and the beam path of AOM in three different scenarios: unshifted, upshifted and downshifted. The timing of the frequency shift/unshift is controlled by the TTL signal from the electronics system. The key components of AOM are two acousto-optic crystals attached to piezo-electric transducers (Brimrose, TEF-315-.589), which generate acoustic vibrations at 315 MHz. The vibration periodically modulates the index of refraction inside the crystal. As a result, part of the incident light is diffracted by a certain angle. The frequency of the diffracted beam is Doppler-shifted by 315 MHz. For the dual-pass AOM, the net frequency shift is  $315 \times 2 = 630$  MHz.

The challenge of the AOM design is to separate the incident and output beams independent of the frequency. However, when the transducer is on and the frequency is shifted by the crystal, the beam will be diffracted by an angle  $2\theta$ . Following the first-order Bragg diffraction condition,  $\theta$  is defined as  $\sin\theta = \lambda_i/2\lambda_a$ , where  $\lambda_i$  is the incident beam wavelength and  $\lambda_a$  is the wavelength of acoustic wave. The dual-pass design with two AO crystals overlap the incident and reflected beams inside the AOM for all three frequencies, as illustrated in Figure 2.8. The single path diffraction efficiency of the AO crystal is  $\sim 80\%$ . A chopper wheel is customized to block the unshifted beam when the shifted beam is desired. To separate the beam out of the module from the input beam, a polarizing beam splitter is placed at the entrance/exit of the AOM. In addition, a quarter waveplate is put into the path of light. For the dual-pass design, the polarization of the incident beam is rotated  $90^\circ$  cumulatively. The polarization of the output beam is perpendicular to that of the incoming beam. Therefore, the polarizer reflects the output beam and transmits the incident beam.

**D. Pulsed Dye Amplifier:** The CW laser beam exiting the AOM is guided into the Pulsed Dye Amplifier (PDA) and significantly amplified pulse by pulse. The PDA is pumped by a single-mode pulsed Nd:YAG laser (Spectra-Physics Quanta-Ray Pro-230) at 532 nm with 50 Hz repetition rate and  $\sim 15$  W power. There are three amplification stages inside the PDA using a dye mixture of Rhodamine 640 and Kiton Red 620 as the gain medium. This design of the PDA generates an output beam with  $> 1$  W power and  $< 20$  mW Amplified Spontaneous Emission (ASE). The outgoing beam of the PDA has  $\sim 120$  MHz bandwidth and  $\sim 12$  ns pulsewidth. After the output of the PDA, the pulsed laser

beam is divided into two or three beams by beam splitters and pointed upward in the desired directions by mirrors.

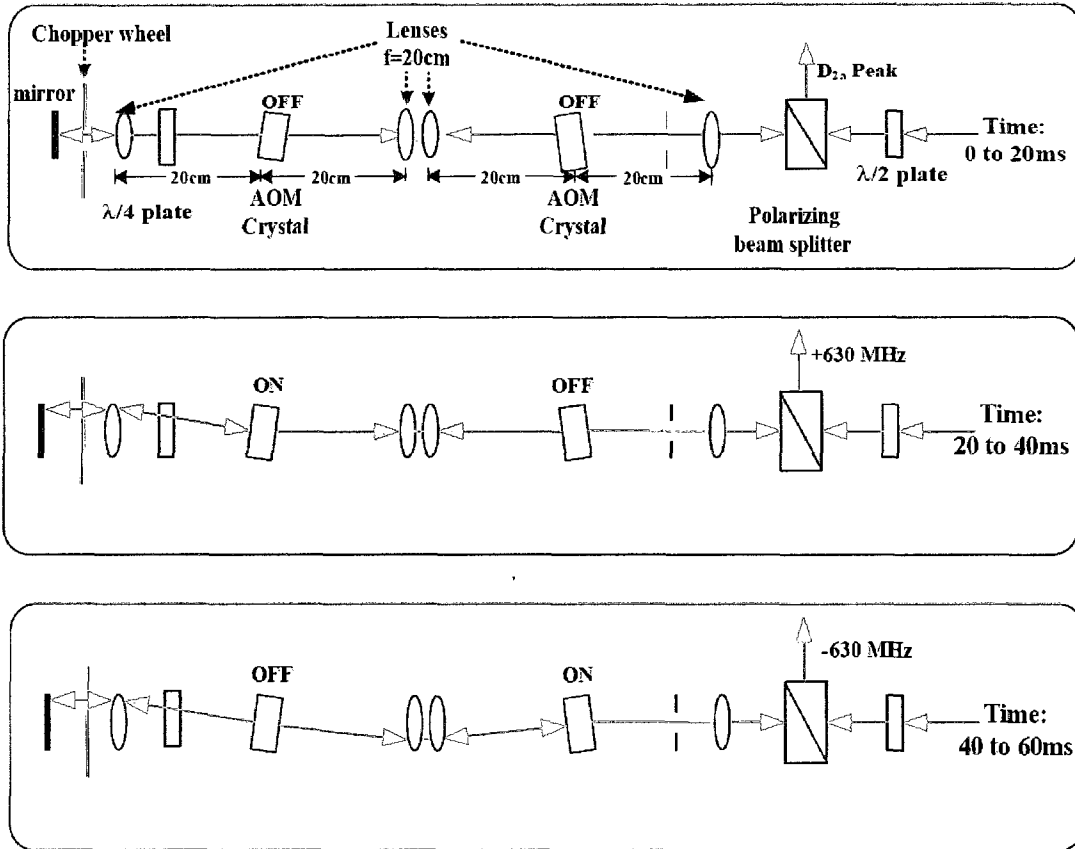


Figure 2.8 Schematic of AOM used in the current CSU lidar system. The three blocks illustrate three beam paths for  $\nu_0$ ,  $\nu_0+630$  MHz,  $\nu_0-630$  MHz, respectively [Sherman, 1999].

**E. Chirp Monitor:** Even though the CW seed laser frequency can be locked precisely at the  $D_{2a}$  Lamb dip within  $\pm 1$  MHz, nonlinear amplification in the PDA produces a small centroid frequency shift, a so-called “chirp” [Siegnam, 1986], from the seed frequency, as shown in Figure 2.9. The impact of this frequency bias on the temperature measurement is negligible; however, a 1-MHz frequency shift corresponds to

0.6 m/s wind measurement bias. A “chirp” monitor subsystem is used to characterize this shift in order to correct it in the data analysis program. An iodine absorption line near 589.16 nm is utilized. A small portion of the PDA output pulse is transmitted through an iodine vapor cell. We monitor the change of the transmission through the cell at two lidar frequencies,  $\nu_0$  and  $\nu$ . (see Figure 2.10). The two transmissions form a ratio

$$R = (T_{pulse}^- - T_{pulse}^0) / (T_{pulse}^- + T_{pulse}^0) \quad (2.9)$$

as a function of frequency shift, where T is the iodine pulse transmission, and the subscripts 0 and – denote the frequencies,  $\nu_0$  and  $\nu$ . The ratio is correlated to the frequency shift  $\Delta\nu_{shift}$  by  $\Delta\nu_{shift} = c_0 + c_1R + c_2R^2 + c_3R^3$ . The  $c_0$ - $c_3$  parameters are determined by the iodine pulsed transmission function. More detailed discussion on the “chirp” experiment can be found in White [1999], Sherman [2002] and Yuan et al. [2009]. The “chirp” monitor has been validated by comparing to the vertical wind measurement. It is worthy to point out that, in addition to the iodine absorption method, the “chirp” bias can also be measured by heterodyne coherent method [Chu, personal communication, 2008].

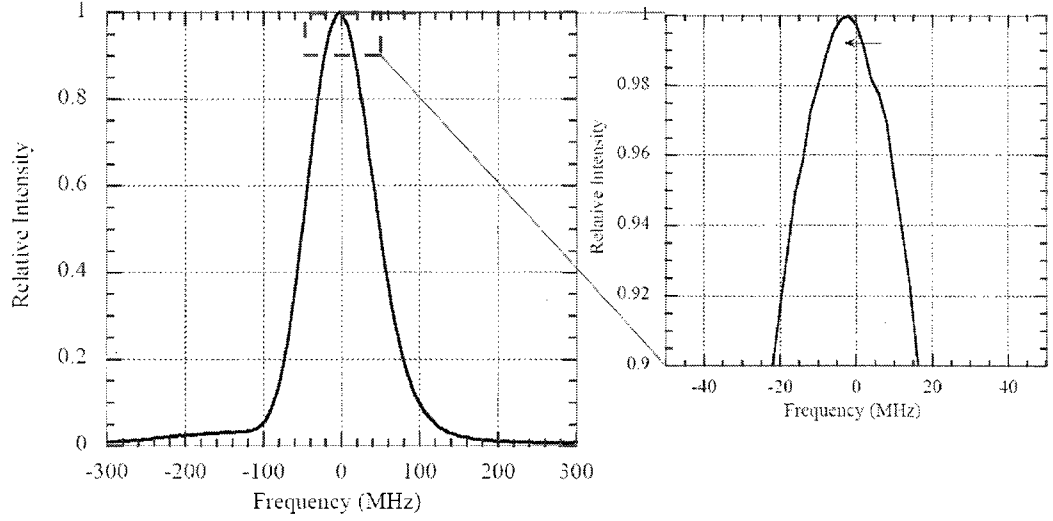


Figure 2.9 Lineshape function of the PDA output pulse calibrated in 2007. The peak of the pulse is zoomed in to show more clearly a negative shift of several MHz.

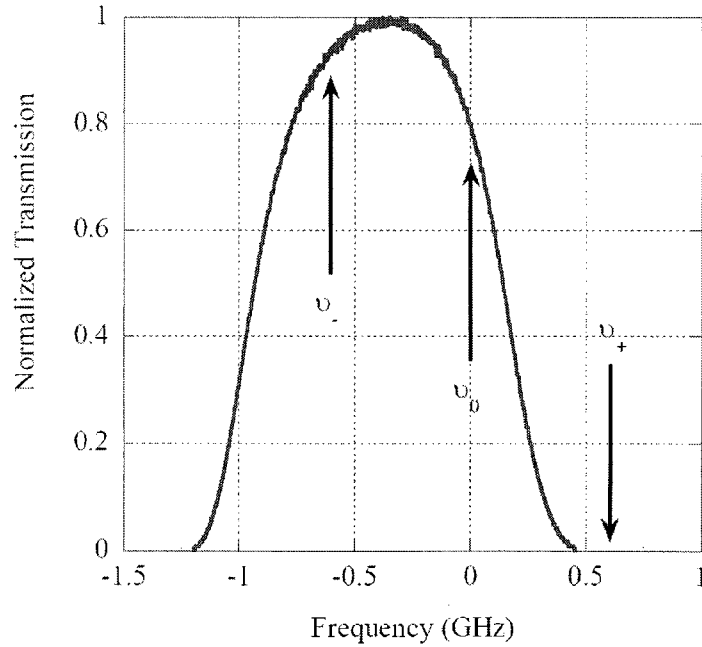


Figure 2.10 Iodine transmission measured by the CW ring dye laser in 2007. The locations of the three operating lidar frequencies are denoted.

### 2.2.2 Sodium lidar receiver

Compared to the transmitter, the CSU Na lidar receiver is relatively simple. Depending on the number of laser beams aimed at different directions, two or three telescopes are used to collect the backscattered photons. For the gravity wave momentum flux measurement in winter since 2006, two 76 cm Newtonian Starsplitter II telescopes are pointing eastward and westward  $20^\circ$  from zenith and one 35 cm Schmitt Cassegrain Celestron C-14 telescope is northward  $30^\circ$  from zenith [Acott, 2009]. For the regular 24-hour atmospheric tidal study, only one Starsplitter II telescope and one Celestron C-14 telescope are used. The telescope scheme is not yet fixed. Figure 2.11 shows a diagram of the receiver. Only two telescopes, one Celestron C-14 and one Starsplitter II, are drawn. The signals are coupled by lenses from the telescopes into optical fibers and guided by fibers onto the photodetectors, which are Photomultiplier tubes (PMT). The fiber for the 35 cm telescope is 0.9 mm in diameter and 0.116 numerical aperture (NA), while the fiber for the 76 cm telescope is 1.5 mm in diameter and 0.37 NA [Acott, 2009].

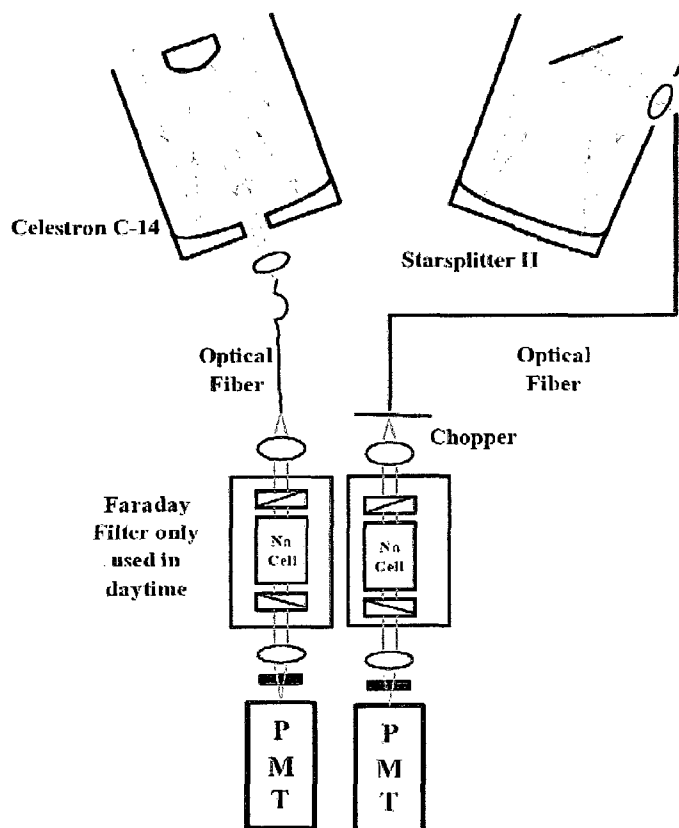


Figure 2.11 The current receiver system of CSU Na lidar.

In addition to the large telescopes, higher efficiency PMTs are installed for the purpose of momentum flux measurement. Two types of PMTs are available for use: two PMTs are Hamamatsu H7421-40 with < 20% quantum efficiency (QE), another two are Hamamatsu R934-02 PMTs with 40% QE. The lower QE PMTs include an electronic blanking circuit to remotely turn on/off the PMTs from the control program. This blocks out the strong Rayleigh and Mie scattering signals from lower altitudes and protects the PMTs from saturation. However, the newer and higher QE PMTs have no such functionality. An extra mechanical chopper (Boston Electronics 300C) is necessary to

synchronize with the laser firing and block the strongest backscattering light [Acott, 2009].

To enable full-diurnal cycle observations and tidal studies, two Faraday filters are inserted in front of the PMTs in the daytime to reduce the sky background by a factor of 6000 to 8000. As shown in the Faraday filter part of Figure 2.11, the Faraday filter consists of one heated Na vapor cell in a magnetic filter sandwiched between two perpendicular polarizers. The randomly-polarized incident light is linearly polarized by the first polarizer. The polarization of the signal at the sodium D<sub>2</sub> frequency is rotated by 90° through the sodium vapor cell in a magnetic field [Chen, 1997; Chen, 1999; Yuan, 2004]. Therefore, the signal is able to pass through the second crossed polarizer. The polarization of the off-resonance background is unchanged and is blocked by the second polarizer. The normalized transmission of the Faraday filter in use is illustrated in Figure 2.12. Disregarding the signal loss at the initial polarizer, the filter has about 85% peak transmission at Na D<sub>2</sub> transition with a FWHM of ~4 GHz.

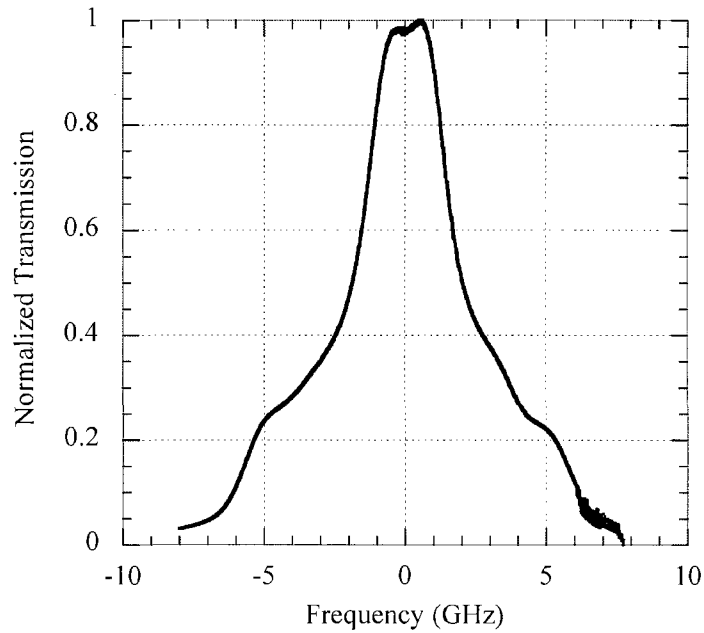


Figure 2.12 Normalized transmission function of Faraday vapor filter measured on September 29, 2008. The “0” frequency is the center of mass of the D2 transition (589.158 nm). The oven and the tip temperatures are 168 and 145 °C. The magnetic field is 1750 Gauss. The length of the sodium cell is 40 mm.

### 2.2.3 Sodium lidar electronics and control system

To guarantee that the lidar system works properly, the electronic and control system is as important as the transmitter and the receiver. The electronic system including both hardware and software controls the lasers, collects the data and synchronizes the timing of various parts of the lidar system. Figure 2.13 displays the flow chart of the control system. Among all of the components, the logic circuit and the Labview program in the Labview computer serve as the “brain”. The Labview computer is using a National Instruments DAQ-6024E data acquisition card with a control program “Lock&Chirp” written in Labview code. The main job of the Labview computer is to analyze the incoming Doppler-free fluorescence signal and lock the CW ring laser at the  $D_{2a}$  peak of the Na  $D_2$  transition. The logic circuit is composed of a number of 74 series logic IC

chips. Figure 2.14 gives the timing diagram of the signals in and out of the logic circuit. Another three computers are called the “Optech” computer with an MSDOS operating system with a Optech fdc700m card, the “Comtec” computer with a Windows 2000 operating system with two Comtec P7882 cards and a Linux server. All together there are six data acquisition channels. Both the Optech and the Comtec computers automatically save the data onto the server.

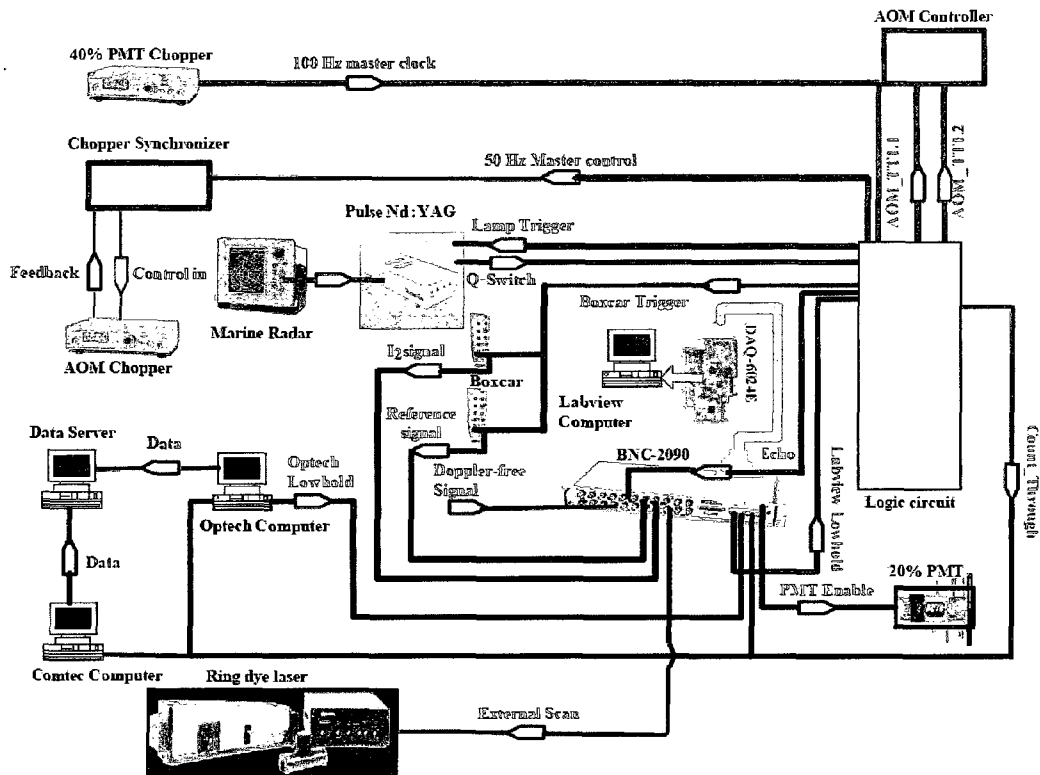


Figure 2.13 Diagram of CSU Na lidar electronics.

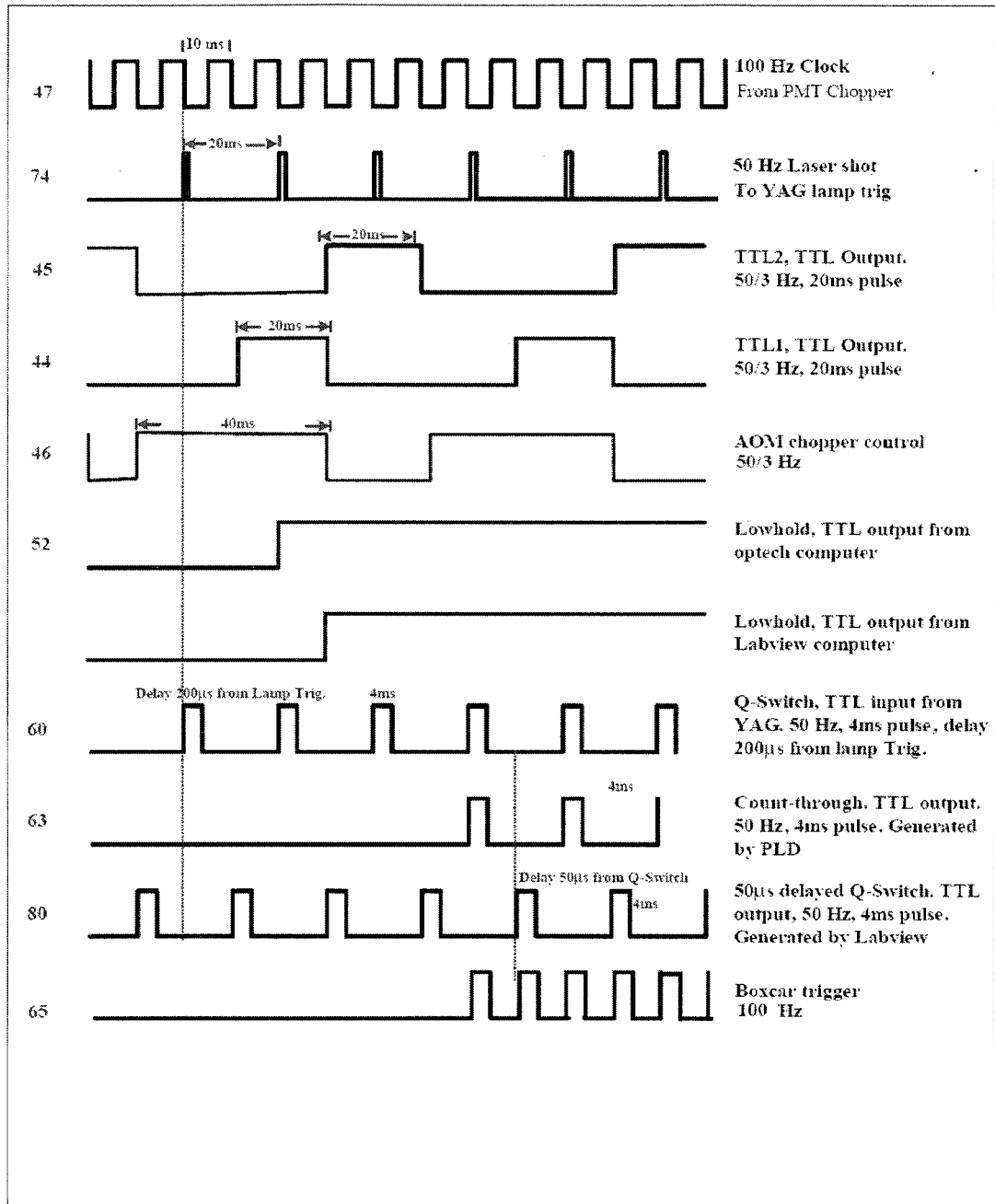


Figure 2.14 Waveform diagram of the current lidar system signals showing corresponding period and pulsewidth. The numbers on the left are the designated BNC cable numbers.

The primary mission of the logic circuit is to synchronize the pulsed laser, data acquisition, PMTs, choppers and Boxcar averagers. The 100 Hz TTL signal generated by

the 40% PMT chopper is set as the master clock for the entire electronics, because the frequency jitter is more crucial for PMT safety than for other equipment. The rest of the signals for other devices must follow the PMT chopper.

**A. 50 Hz laser shot signal** for firing the pulsed Nd:YAG laser is falling-edge triggered by the 100 Hz TTL signal every two cycles (20 ms) with a digital counter in the logic circuit [Acott, 2009]. The pulse width of the laser shot signal can be changed to satisfy the YAG laser's trigger requirement.

**B. Q-switch signal** is the 50 Hz TTL output from the YAG laser with 200  $\mu$ s delay from the laser shot signal. It is fed back to the logic circuit to trigger data acquisition.

**C. Lowhold signals** from Labview and Optech computers go high when the computers are ready for data acquisition.

**D. AOM1, AOM2 and AOM chopper control** signals are essential to the proper operation of the AOM. AOM1 and AOM2 50/3 Hz TTL signals turn on and off the corresponding AO crystal transducers. The frequency of the CW light into the PDA is then modulated in a sequence of  $\nu_0$ ,  $\nu_+$ ,  $\nu_-$ . Like the laser shot signal, they are also generated by the counter in the logic circuit and the 100 Hz TTL signal. Directly inverted from AOM2, the AOM control "reset" signal synchronizes the AO chopper with the frequency shift to block unwanted light. A 300 Synch Chopper Synchronizer by Boston Electronics is used to maintain the chopper phase. The same AOM1 and AOM2 TTL signals are also fed into the Comtec computer. The combination of AOM1 and AOM2 signals allows the Comtec computer to tag the data with corresponding frequency.

**F. Count-through signals** from the logic circuit tell the Comtec and Optech computers when to start counting photons. The count-through signal has the same waveform of the

Q-switch signal except that the first pulse is at  $\nu_0$  (after the rising edge of AOM control) and the lowhold is high (all the computers are ready to take data).

**G. Boxcar trigger** controls the timing of the Stanford Research Systems SR250 Gated Integrator and Boxcar Averager. It is twice the frequency ( $\sim 100$  Hz) of the count-through signal. In this way, the background between two pulses can be recorded and subtracted from the signal.

The “lock&chirp” Labview program accomplishes two significant tasks. It maintains the lock of the ring dye laser and calculates the chirp velocity bias. When the Comtec and Optech computers are taking data, the Labview program reads the Doppler-free signals and detects the frequency drift using a phase detection technique. Then with proper settings of proportional-integral-differential (PID) bands, the program feeds back the external scan signal to the ring laser controller every 0.4 s. This part of the program works as an external LIA. During the interval when the computer is saving the data, the program scans the spectrum around the locking point over 200 MHz and relocks the frequency at the peak of the spectrum (highest  $D_{2a}$  Lamb dip). Regarding the chirp bias calculation, the program reads in the Boxcar signals and calculates the ratio  $R$  following (2.7). Therefore, for every data profile, the frequency shift is obtained and displayed. When the system is not working properly, the chirp value could be unusual, reminding the operator to check the system.

## 2.3 Kyoto University OH airglow all-sky imager

The Na lidar measures only the vertical profiles of temperature and wind as a function of time. As will be seen in the next chapter, the horizontal information on gravity waves is as important as the vertical information. To obtain a horizontal map of gravity waves, we use the Kyoto University OH airglow imager at the Yucca Ridge Field Station (~15 km northeast of Fort Collins). The theory of the airglow imager and the data analysis will be introduced in the subsections below.

### 2.3.1 OH airglow emission layer

In the mesopause region, there are bright nightglow emissions from several molecular and atomic species, such as hydroxyl (OH), sodium (Na), molecular oxygen (O<sub>2</sub>) and atomic oxygen (OI). The nightglow spectra at visible and infrared bands are shown in Figure 2.15. The OH Meinel band is concentrated from 550 nm to 4400 nm (although the Yucca Ridge imager detects between 795 and 1000 nm band); the Na lines are 589.0 and 589.6 nm; and the OI band is at 557.7 nm. These emission layers occur at different altitudes in the atmosphere. The OH emission layer is centered at 87 km with about 10 km depth. The Na nightglow layer is between 80 and 105 km. The OI layer is near 97 km [Taylor et al., 1987]. By monitoring the airglow emissions simultaneously at different bands, vertical information on gravity wave structures can also be revealed. This is because, in addition to the chemical reactions to be discussed below, these species act as a tracer of air density and follow the motion of air parcels. Therefore, the strength of their emissions traces out atmospheric density perturbations and hence gravity waves or other atmospheric waves. The Kyoto University imager at Yucca Ridge detects only the OH Meinel band. Therefore, we discuss only the OH nightglow here.

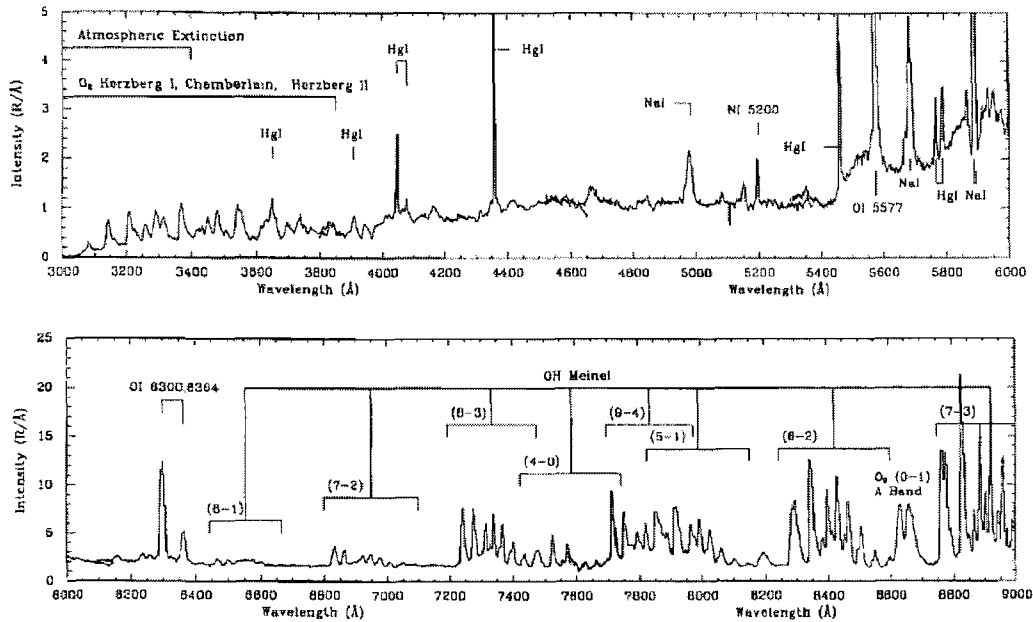


Figure 2.15. The nightglow spectrum from the visible to the infrared regions observed on the ground, not including all OH emission spectrum, which extends to  $\sim 4400$  nm. [Johnson and Broadfoot, 1993].

The OH nightglow emission is excited by a series of chemical reactions.



where  $v$  and  $v'$  are vibrational states ( $v > v'$ ). Reactions (2.10)-(2.12) produce the excited state of hydroxyl ( $\text{OH}^*$ ) with vibrational state of 9 or less. Immediately after an  $\text{OH}^*$  molecule is generated, the hydroxyl has some non-zero probability of relaxation from the upper vibrational state ( $v$ ) to the lower state ( $v'$ ), emitting a photon to carry away the transition energy.

### 2.3.2 OH airglow imager

The Kyoto University OH imager was deployed at Yucca Ridge near Fort Collins in September 2003. Figure 2.16 gives a schematic diagram of the system. Unlike the very complex CSU Na lidar system, the imager system basically consists of a primary lens, an optical filter, a CCD camera and a PC with a data acquisition program. A fish-eye lens (Nikkor,  $f=8$  mm,  $f/2.8$ ) is used beneath the customized dome. Between the lens and the CCD chip, a long-wave pass optical filter (Kodak Wratten Filter #87) with a cut-off wavelength of 795 nm is inserted. The CCD camera (SBIG ST-1001E) uses a Kodak KAF1001E CCD chip ( $1024 \times 1024$  pixels in the area of  $24.6 \text{ mm}^2$ ). The camera is air-cooled to less than  $-10^\circ\text{C}$  to minimize the dark noise. In order to improve the signal-to-noise ratio, the chip is binned to  $512 \times 512$  pixels. The CCD chip can sense only photons with wavelengths shorter than 920 nm. Therefore, the imager is designed to be sensitive to most of the Meinel band (see Figure 2.15) and insensitive to other strong nightglow lines. The imager is connected to the control PC for automatic data acquisition and storage. The CCD chip is exposed for 100 seconds and the image is saved every 2 min. The imager data can remotely be downloaded by the computer at Colorado State University through RealVNC.

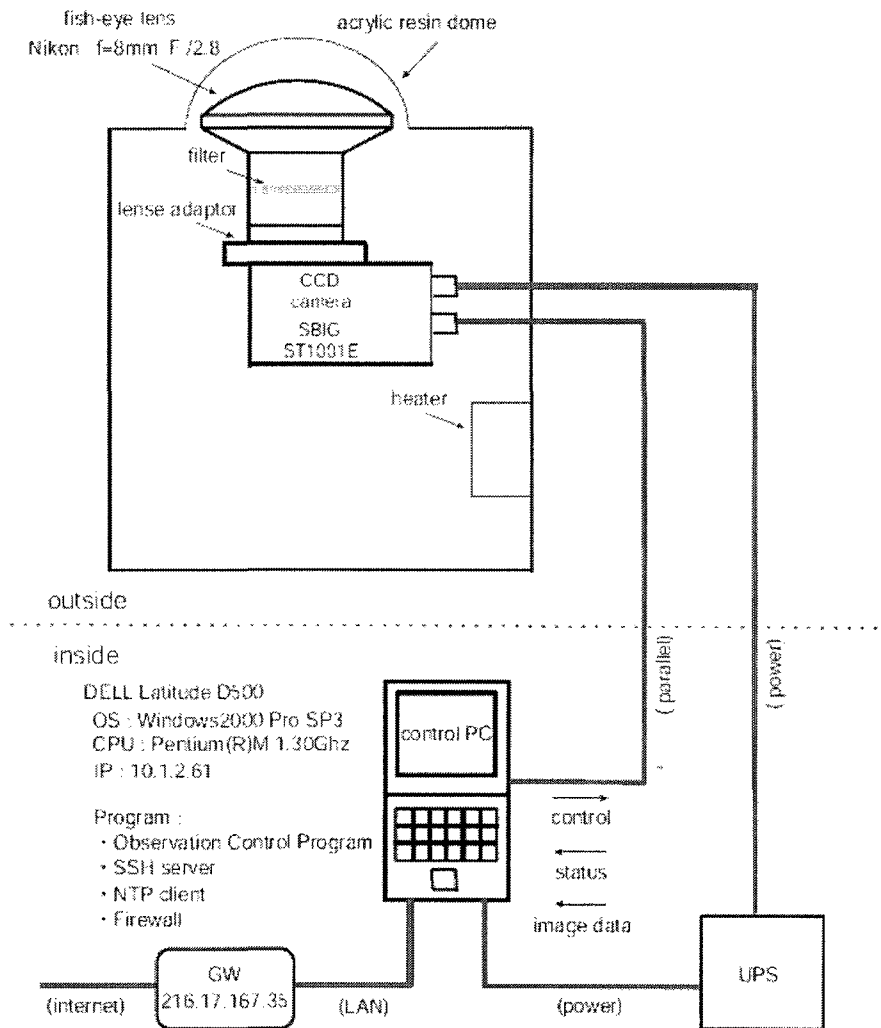


Figure 2.16 Schematic diagram of the Yucca Ridge OH imager [Fukushima, 2004].

### 2.3.3 OH airglow image processing

An example of a raw OH airglow image is given in Figure 2.17. Many stars can be seen all over the sky. The line near the upper edge is a meteor. The bright band extending from the southwest to the northeast is the Milky Way. The object near the left upper corner is unrelated equipment near the dome. Wavy bands are apparent in the field near the meteor, but they are unrelated to the meteor. These are gravity waves of interest.

In order to enhance gravity waves and study their characteristics, image processing is necessary, as described below.

The first step is rotating the whole image to put the North Star at the appropriate azimuth. The camera is designed to close the shutter every 1 hour to record the dark counts, so this dark image can be subtracted from each image. Next, depending on the purpose of the study, there are two ways to process the rotated raw image. To view the short period gravity waves like ripples, we subtract consecutive 2 min images to form difference images. In this way, the non-varying or slowly-varying background is removed, for example, the stars, city lights and moonlight. The differencing acts effectively like a high-pass filter, with maximum response at 4 min periods, falling off as the gravity wave period increases. The resulting image is named the difference image. The second way is normalization, achieved by dividing each image by the average of the 1-hour or 1-night mean after stars are removed by the median filter. In this way, the longer period gravity waves are enhanced. We will show examples of these two types of images in Chapter 4.

To facilitate the direct measurement of the horizontal wavelength and apparent phase velocity, we need to unwrap the all-sky images onto the flat field. The detailed algorithm is discussed in Garcia et al. [1997]. In general, the method is to convert the emission brightness as a function of azimuth and elevation angle to the (x,y) geographic axis. Figure 2.18 gives an example of an unwrapped difference image of Figure 2.17. The latitude/longitude coordinates and state borders have also been added.

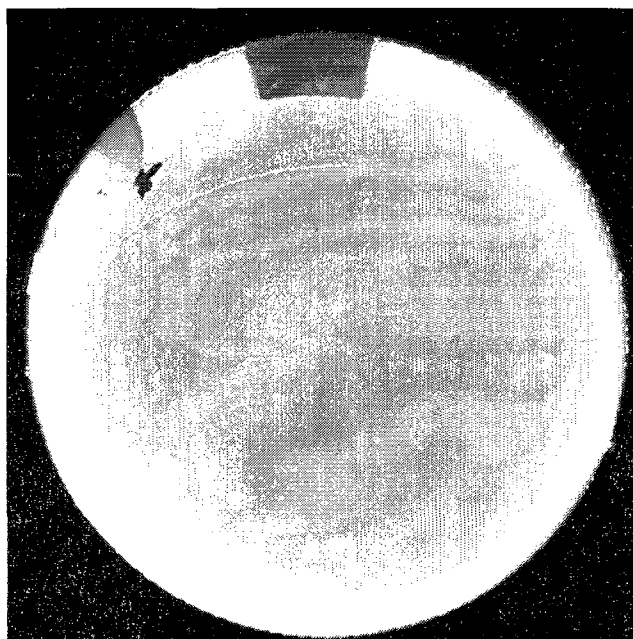


Figure 2.17 An example of an OH imager raw image taken at 0310 UT on October 07, 2005.

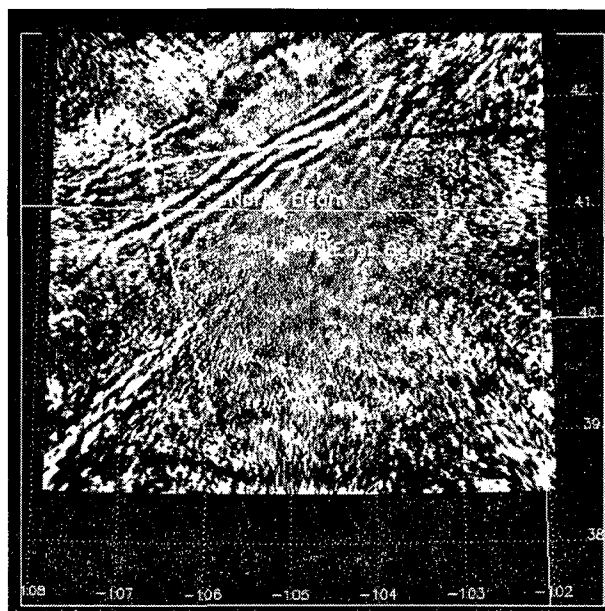


Figure 2.18 The difference image at the flat field for Figure 2.17.

We make three types of pictures and associated movies from the imager data: rotated raw images, difference images and associated unwrapped difference images. In

this way, we can quickly examine the data to find interesting gravity wave related phenomena, e.g., concentric gravity waves, mesospheric bores, and ripples. These scientific results will be presented in Chapter 4.

Before we present scientific results in Chapter 4 using the data from the CSU Na lidar system and the Yucca Ridge OH airglow imager, a review of gravity wave theory will be conducted in Chapter 3. Thus when Chapter 4 is reached, we will have not only an idea of how the data were obtained, but also will understand the atmospheric dynamics behind those observations.

## References:

- Acott, P. E., Mesospheric momentum flux studies over Fort Collins CO (41N, 105W), *Ph.D. Dissertation*, Colorado State University, 2009.
- Chen, H., A sodium fluorescence lidar for daytime operation using dispersive faraday vapor filter, *Ph.D. Dissertation*, Colorado State University, 1997.
- Chen, S., 24 hour lidar campaigns and Tidal Analysis, *Ph.D. Dissertation*, Colorado State University, 1999.
- Fukushima, T., A study on variability of airglow structure with dual-site imaging observations, *Master Thesis*, Kyoto University, 2004,
- Garcia, F. J., M. J. Taylor, and M. C. Kelley, Two-dimensional spectral analysis of mesospheric airglow image data, *Appl. Opt.*, 36, 7374-7385, 1997.
- Johnston, J. E., and A. L. Broadfoot, Midlatitude Observations of the Night Airglow: Implications to Quenching Near the Mesopause, *J. Geophys. Res.*, 98(A12), 21,593–21,603, 1993.
- Li, T., Sodium lidar observed variability in mesopause region temperature and horizontal wind: planetary wave influence and tidal-gravity wave interactions, *Ph.D. Dissertation*, Colorado State University, 2005.
- Mimoun, E., L. De Sarlo, J. Zondy, J. Dalibard, and F. Gerbier, Sum-frequency generation of 589 nm light with near-unit efficiency, *Opt. Express*, 16, 18684-18691, 2008.
- Moosmüller, H. and J. D. Vance, Sum-frequency generation of continuous-wave sodium D<sub>2</sub> resonance radiation, *Opt. Lett.*, 22, 1135-1137, 1997.
- She, C. Y., J. R. Yu, H. Latifi, R. E. Bills, High-spectral-resolution fluorescence light detection and ranging for mesospheric sodium temperature measurements, *Appl. Opt.*, 31, 2095-2106, 1992.
- She, C. Y., and J. R. Yu, Doppler-free saturation fluorescence spectroscopy of Na atoms for atmospheric application, *Appl. Opt.*, 34(6), 1063-1075, 1995.
- She, C. Y., and D. A. Krueger, Laser-induced fluorescence: spectroscopy in the sky Optics, *Photonic News (OPN)*, 35-41, September issue, 2007.
- She, C. Y., J. D. Vance, T. D. Kawahara, B. P. Williams, Q. Wu, A proposed all-solid-state transportable narrow-band sodium lidar for mesopause region temperature and horizontal wind measurements, *Can. J. of Phys.*, 85(2), 111-118(8), 2007.

- Sherman, J. P., Mesopause region thermal and dynamical studies based on simultaneous temperature, zonal and meridional wind measurement with an upgraded sodium fluorescence lidar, *Ph.D. Dissertation*, Colorado State University, 2002.
- Siegman, A.E., *Lasers*, University Science Books, Mill Valley CA., 1986.
- Smith, J. A., X. Chu, W. Huang, J. Wiig, and A. T. Brown, LabVIEW-based laser frequency stabilization system with phase sensitive detection servo loop for Doppler lidar application, *Optical Engineering*, 47(11), 114201, 2008.
- Taylor, M.J., M.A. Hapgood, and P. Rothwell, Observation of gravity wave propagation in the OI (557.7 nm), Na (589.2 nm) and the near infrared OH nightglow emissions, *Planet. Space Sci.*, 35(4), 413-427, 1987.
- Theon, J. S., The mean observed structure and circulation of the stratosphere and mesosphere, *NASA Tech. Rep.*, TR-375, 1972.
- Vance, J. D., C. Y. She, and H. Moosmüller, Continuous-Wave, All-Solid-State, Single-Frequency 400-mW Source at 589 nm Based on Doubly Resonant Sum-Frequency Mixing in a Monolithic Lithium Niobate Resonator, *Appl. Opt.*, 37, 4891-4896, 1998.
- White, M. A., A frequency-agile Na lidar for the measurement of temperature and velocity in the mesopause region, *Ph.D. Dissertation*, Colorado State University, 1999.
- Yu, J. R., A sodium wind/temperature lidar and observed mesopause thermal structure over Fort Collins, CO, *Ph.D. Dissertation*, Colorado State University, 1994.
- Yuan, T., Seasonal variations of diurnal and semidiurnal tidal-period perturbations in mesopause region temperature and zonal and meridional winds above Ft. Collins, CO (40°N, 105°W) based on Na-Lidar observation over full diurnal cycles, *Ph.D. Dissertation*, Colorado State University, 2004.
- Yuan, T., C.-Y. She, D. A. Krueger, F. Sassi, R. Garcia, R. G. Roble, H.-L. Liu, H. Schmidt (2008), Climatology of mesopause region temperature, zonal wind, and meridional wind over Fort Collins, Colorado (41°N, 105°W), and comparison with model simulations, *J. Geophys. Res.*, 113, D03105, doi:10.1029/2007JD008697, 2008.
- Yuan, T., J. Yue, C. Y. She, J. P. Sherman, M. A. White, S. D. Harrell, P. E. Acott, and D. A. Krueger, Wind-bias correction method for narrowband sodium Doppler lidars using iodine absorption spectroscopy, *Appl. Opt.*, 48, 3988-3993, 2009.
- Yue J., C.-Y. She, B. P. Williams, J. D. Vance, P. E. Acott, and T. D. Kawahara, Continuous-wave sodium D<sub>2</sub> resonance radiation generated in single-pass sum-frequency generation with periodically poled lithium niobate, *Opt. Lett.* 34, 1093-1095, 2009.

### **Chapter 3: Gravity wave theory in the middle atmosphere**

Atmospheric gravity (or more precisely, buoyancy) waves have drawn growing attention from scientists since the paper of Hines [1960] because of their significant impact on the middle atmosphere. They contribute greatly to the general circulation, as well as the thermal structure and constituent distributions, by transporting momentum and energy from lower atmosphere sources to the middle atmosphere. The momentum flux deposited by gravity waves leads to the departure of the temperature distribution from its intuitive radiative steady state as introduced in Chapter 1. At the same time, seasonally-varying gravity wave forcing induces meridional circulation in the mesosphere from the summer pole to the winter pole [Holton, 1983]. Gravity waves are also thought to provide a seeding mechanism for equatorial plasma bubbles in the ionosphere [Kelley et al., 1981], which cause disruptions in radio-wave communication and strongly affect space weather forecasts. Theoretical, numerical and observational studies are crucial to advance the understanding of gravity wave source characterizations, evolution, instability dynamics, wave-wave and wave-mean flow interactions. We have studied three independent but related topics on gravity waves, using ground-based instruments, the Na Doppler lidar and the OH airglow imager. The first topic describes one of the major gravity wave sources [Fritts and Alexander, 2003], convection, and the observation of convective gravity waves in the mesopause region. The second topic concerns the

nonlinear evolution of gravity waves in a ducted region, resulting in the generation of mesospheric bores. The third topic is the investigation of large wind shears and the relationship of maximum allowed wind shear and large convective stability, along with the discussion of the large amplitude or short vertical wavelength semidiurnal tidal period perturbations as the main cause for generating the observed large wind shears. These subjects will be discussed in Chapter 4. Before presenting the results, general gravity wave theory is reviewed in this chapter.

### 3.1 Air parcel model

The physics of gravity waves can be explained by considering the motion of a simple air parcel in a stratified atmosphere. In this model, the movement of the parcel is adiabatic, i.e., there is no heat source or sink within it. The gravity or buoyancy force is the restoring force when the parcel is displaced. As shown in Figure 3.1, the parcel is displaced  $\delta s$  from the equilibrium at  $z_0$  along a line tilted at an angle of  $\beta$  to an isentrope (a line with constant potential temperature). The potential temperature  $\theta$  of a parcel at pressure  $p$  is the temperature if the pressure on the parcel is adiabatically displaced to the reference pressure  $p_0$ , and is defined by:

$$\theta = T \left( \frac{p_0}{p} \right)^\kappa \quad (3.1)$$

where  $\kappa = R/c_p$ ,  $R$  is the gas constant per unit mass and  $c_p$  is the specific heat capacity at a constant pressure. The resulting vertical distance  $\Delta z$  is  $\Delta s \sin\beta$ . The net force (gravity minus buoyancy) on the parcel  $gV(\rho_e - \rho_p)$  is vertical, where  $V$  is the volume of the parcel,  $\rho_p$  is the air parcel mass density,  $\rho_e$  is the environmental air mass density. The component of this force perpendicular to the path is balanced by the pressure gradient induced by the

wave oscillation discussed below. The component of this force parallel to the path is accelerating the parcel. Thus the acceleration of the air parcel times the mass is equal to the net force along the tilted path:

$$\rho_p V \frac{d^2(\delta s)}{dt^2} = gV(\rho_e - \rho_p) \sin \beta \quad (3.2)$$

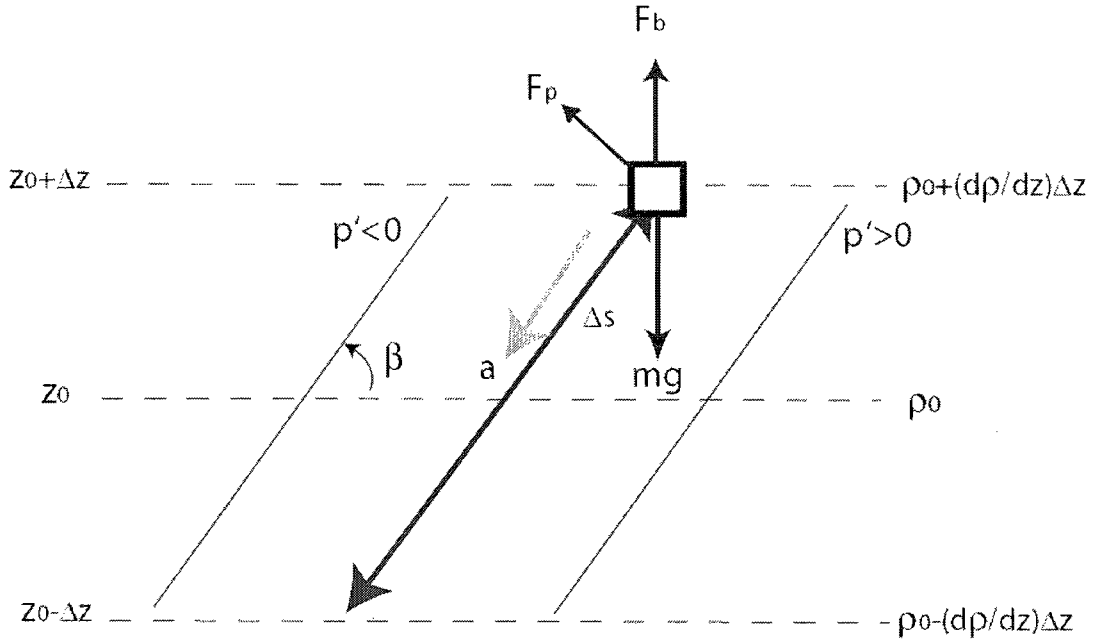


Figure 3.1 Air parcel oscillation scheme. Heavy arrow: oscillation path, light arrow: force vector, dashed lines: isentropic lines, solid line: wave front.

Then the acceleration of the air parcel becomes:

$$\begin{aligned} \frac{d^2(\delta s)}{dt^2} &= g \left( \frac{\rho_e}{\rho_p} - 1 \right) \sin \beta = g \left( \frac{T_p}{T_e} - 1 \right) \sin \beta = g \left( \frac{T_0 - \Gamma_a (\delta s \sin \beta)}{T_0 + dT/dz (\delta s \sin \beta)} - 1 \right) \sin \beta \\ &= g \left( \frac{-dT/dz - \Gamma_a}{T_0 + dT/dz (\delta s \sin \beta)} \right) \delta s \sin^2 \beta = \frac{g}{T} (-dT/dz - \Gamma_a) \delta s \sin^2 \beta \end{aligned} \quad (3.3)$$

Here,  $\Gamma_a = 9.5 \text{ K/km}$  is the adiabatic lapse rate near the mesopause region and  $T_0$  is the background temperature at equilibrium. Using the ideal gas law (1.1) and assuming that

the air parcel and the environment have the same pressure, we have used  $\frac{\rho_e}{\rho_p} = \frac{T_p}{T_e}$  in

(3.3). Both  $T_p$  and  $T_e$  are considered small departures from the equilibrium temperature  $T_0$ . Therefore,  $T_p$  and  $T_e$  can be written as  $T_0 - \Gamma_a(\delta s \sin \beta)$  and  $T_0 + dT/dz(\delta s \sin \beta)$ .

Defining the square of the Brunt-Väisälä frequency as  $N^2 = \frac{g}{T}(dT/dz + \Gamma_a) = \frac{g}{\theta}d\theta/dz$ ,

then (3.3) can be simplified as:

$$\frac{d^2(\delta s)}{dt^2} = -(N \sin \beta)^2 \delta s \quad (3.4)$$

Assuming  $N^2$  is positive, the parcel may oscillate at a frequency (angular frequency)  $\omega = N \sin \beta$  and with a maximum frequency of  $N$  for a gravity wave. So far, the derivation is based on the assumption that the atmosphere is stable, i.e., when the air parcel is displaced upward (downward), its density is greater (less) than the ambient air. If the atmosphere is not convectively stable ( $d\theta/dz < 0$ , i.e. oscillation frequency  $\omega$  is imaginary), the restoring force for the air parcel will no longer exist. Therefore, in an unstable atmosphere, gravity waves cannot exist, thus, gravity waves propagating into an unstable region will dissipate its energy. Additional characteristics of gravity waves will be discussed in next section based on linear theory. The discussion of gravity wave instability is deferred to Section 3.4.

### 3.2 Linear theory

In Section 3.1, the parcel model estimates the gravity wave frequency. To fully understand the spatial and temporal features of gravity waves and their dispersion and polarization relations, we have to go through the governing linear theory. Fluid motions

are ruled by three fundamental physical principles: conservation of momentum, conservation of energy and conservation of mass. We also assume that the air satisfies the ideal gas law. The rate of change of momentum, density and thermodynamic energy in the coordinates on the earth's surface under the assumption of  $z \ll a$  (earth radius) and not near the equator or the poles is expressed as [Chapter 4, Andrews, 2000]:

$$\frac{du}{dt} = fv - \frac{1}{\rho} \frac{\partial p}{\partial x} + X \quad (3.5)$$

$$\frac{dv}{dt} = -fu - \frac{1}{\rho} \frac{\partial p}{\partial y} + Y \quad (3.6)$$

$$\frac{dw}{dt} = -g - \frac{1}{\rho} \frac{\partial p}{\partial z} \quad (3.7)$$

$$\frac{d\rho}{dt} = -\rho \left( \frac{\partial u}{\partial x} + \frac{\partial v}{\partial y} + \frac{\partial w}{\partial z} \right) \quad (3.8)$$

$$\frac{d\theta}{dt} = Q = \frac{J}{c_p} \left( \frac{p}{p_0} \right)^{-\kappa} \quad (3.9)$$

where  $(x,y,z)$  are coordinates along the zonal, meridional and vertical directions, respectively, above the surface of earth, and  $(u,v,w)$  is the velocity vector.  $d/dt = \partial/\partial t + u\partial/\partial x + v\partial/\partial y + w\partial/\partial z$  is the total (advective) derivative.  $p$  is the pressure.  $\rho$  is the air mass density.  $f = 2\Omega \sin\Phi$  is the Coriolis parameter ( $\Omega$  is the Earth rotation rate and  $\Phi$  is latitude).  $X$  and  $Y$  are external forces in the  $x$  (zonal) and  $y$  (meridional) directions including friction and wave-driven force.  $J$  is diabatic heating rate.

When there are no external driving forces, the parameters in (3.5)-(3.9) can be linearized around a steady, horizontally uniform background with mean winds  $(\bar{u}, \bar{v}, 0)$ , potential temperature  $\bar{\theta}$ , pressure  $\bar{p}$ , and air density  $\bar{\rho}$  [Chapter 7, Holton, 1992]. The

wave perturbations of wind, temperature, pressure and density are assumed to be small compared to the mean state values. Then the parameters in (3.5)-(3.9) can be written as a sum of the steady state values and the gravity-wave-induced perturbations:

$$(u, v, w, \rho, p, \theta) = (\bar{u}, \bar{v}, 0, \bar{\rho}, \bar{p}, \bar{\theta}) + (u', v', w', \rho', p', \theta') \quad (3.10)$$

The perturbations take the plane-wave-like form of:

$$(u', v', w', \rho', p', \theta') = (\hat{u}, \hat{v}, \hat{w}, \hat{\rho}, \hat{p}, \hat{\theta}) \exp\{i(kx + ly - \omega t) + z/(2H)\} \quad (3.11)$$

to describe a monochromatic wave with horizontal wave number (k,l) and apparent frequency  $\omega$ . The decreasing background air density as height increases is compensated by the growing amplitude of perturbations in the term  $\exp(z/2H)$  to conserve the wave energy. The scale height H is defined by  $RT/g$ , where R is the gas constant per unit mass, and T is the temperature. In this dissertation, we are only interested in small-scale internal gravity waves, for which the Coriolis term in (3.5) and (3.6) is negligible. Combining linearized versions of (3.5)-(3.9) and assuming the wave solutions (3.11) yields the Taylor-Goldstein equation:

$$\frac{d^2(\hat{w})}{dz^2} + \left[ \frac{N^2}{(c_{ph} - \bar{u}_h)^2} + \frac{\bar{u}_h''}{(c_{ph} - \bar{u}_h)^2} - \frac{1}{H} \frac{\bar{u}_h'}{(c_{ph} - \bar{u}_h)} - \frac{1}{4H^2} - k^2 - l^2 \right] \hat{w} = 0 \quad (3.12)$$

Again, N is the Brunt-Väisälä frequency discussed in Section 3.1 and  $c_{ph}$  is the horizontal phase velocity of the wave.  $\bar{u}_h$  is the background horizontal wind in the wave propagation direction and  $\bar{u}_h'$  and  $\bar{u}_h''$  are the first and second order wind gradient with height. For the case of constant N (or temperature) and  $\bar{u}_h$ , the wind shear terms in (3.12) disappear and the solution of  $\hat{w}$  is of the form  $Ae^{imz} + Be^{-imz}$ . Substitution into (3.12), gives the dispersion relation becomes:

$$m^2 = \frac{N^2}{(c_{ph} - \bar{u}_h)^2} - k_h^2 - \frac{1}{4H^2} = \frac{(k^2 + l^2)(N^2 - \hat{\omega}^2)}{\hat{\omega}^2} - \frac{1}{4H^2} = \frac{k_h^2 N^2}{\hat{\omega}^2} - k_h^2 - \frac{1}{4H^2} \quad (3.13)$$

Here the compressibility term  $1/4H^2$  is not negligible because  $H \sim 7$  km in the middle atmosphere.  $k_h = \sqrt{k^2 + l^2}$  is the horizontal wave number.  $\hat{\omega} = \omega - k\bar{u} - l\bar{v}$  is the intrinsic frequency. The intrinsic (angular) frequency,  $\hat{\omega}$  can be rewritten as  $\omega - k_h \bar{u}_h$ , where  $\bar{u}_h$  is the background horizontal wind in the wave propagating direction. The horizontal and vertical gravity wave phase speeds are represented as:

$$(c_{ph}, c_{pz}) = \left( \frac{\omega}{k_h}, \frac{\omega}{m} \right) = (\bar{u}_h, \bar{u}_h k_h / m) + \frac{Nm^{-1}}{\sqrt{k_h^2 + m^2 + 1/4H^2}} (m, k_h) \quad (3.14)$$

Note that the two components of the phase speed here are the phase speed of the wave observed along the horizontal or vertical axis, not the component of the wave phase velocity. Therefore, phase speed is not a vector. The horizontal and vertical gravity wave group velocities describing the energy transport are derived as:

$$(c_{gh}, c_{gz}) = \left( \frac{\partial \omega}{\partial k_h}, \frac{\partial \omega}{\partial m} \right) = (\bar{u}_h, 0) + \frac{N}{k_h^2 + m^2 + 1/4H^2} \frac{(m^2 + 1/4H^2, -k_h m)}{(k_h^2 + m^2 + 1/4H^2)^{1/2}} \quad (3.15)$$

Comparing (3.14) and (3.15),  $c_{gz}$  and  $c_{pz}$  have opposite signs, suggesting that the phase and the energy of the gravity wave are heading in opposite directions in the vertical. Figure 3.2 shows that for upward propagating gravity waves generated in the lower atmosphere,  $c_{gz}$  is positive and  $c_{pz}$  is negative. If  $1/4H^2$  is negligible, then  $c_{gz}$  is parallel to the line of constant phase. The “true” phase velocity  $c_p$  is related to the pseudo-phase velocity  $c_{ph}$  and  $c_{pz}$  in Eqn (3.14) by  $(1/c_p)^2 = (1/c_{ph})^2 + (1/c_{pz})^2$ .

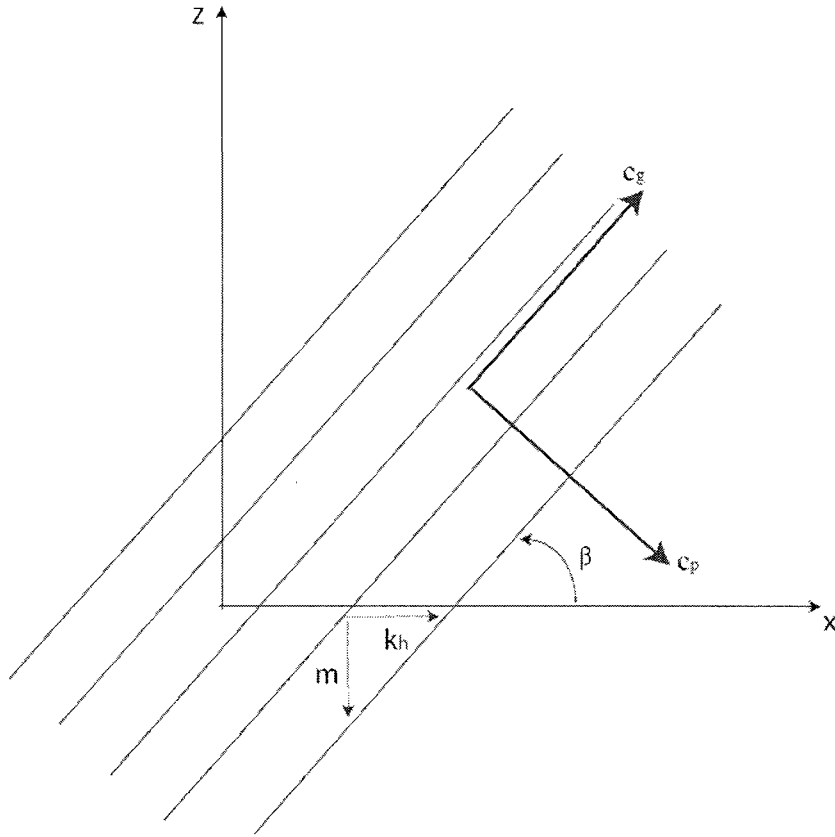


Figure 3.2 Upward-propagating gravity wave phase front and vectors.

In this dissertation, we use two optical instruments to study gravity wave dynamics: the CSU Na Doppler lidar system and the Yucca Ridge OH airglow imager, as introduced in Chapter 2. The lidar measures the temperature and wind perturbation along a tilted or vertical line with time and height resolution; the imager monitors the emission in a horizontal plane over time. Therefore, gravity waves have different shapes in the lidar and imager data. Fig. 3.3(a) shows that the phase of the upward propagating gravity wave downward progresses over time in the lidar contour. With a vertical laser beam, the vertical phase velocity  $c_{ph}$  and vertical wavenumber  $m$  can be measured directly by the Na lidar. For an airglow imager, gravity waves are displayed as parallel lines or curves on the horizontal plane as in Fig. 3.3(b) if we assume that there is no motion of the phase

front in the y-direction. Thus the horizontal phase velocity  $c_{ph}$  and horizontal wavenumber  $k$  can be measured. With the combination of a Na lidar and an airglow imager, the parameters of a gravity wave in the wave dispersion relation (3.13) can all be determined. The amplitude of the wave perturbation can be estimated by the temperature, wind and Na density oscillation measured by the lidar and by the nightglow emission modulation in the imager.

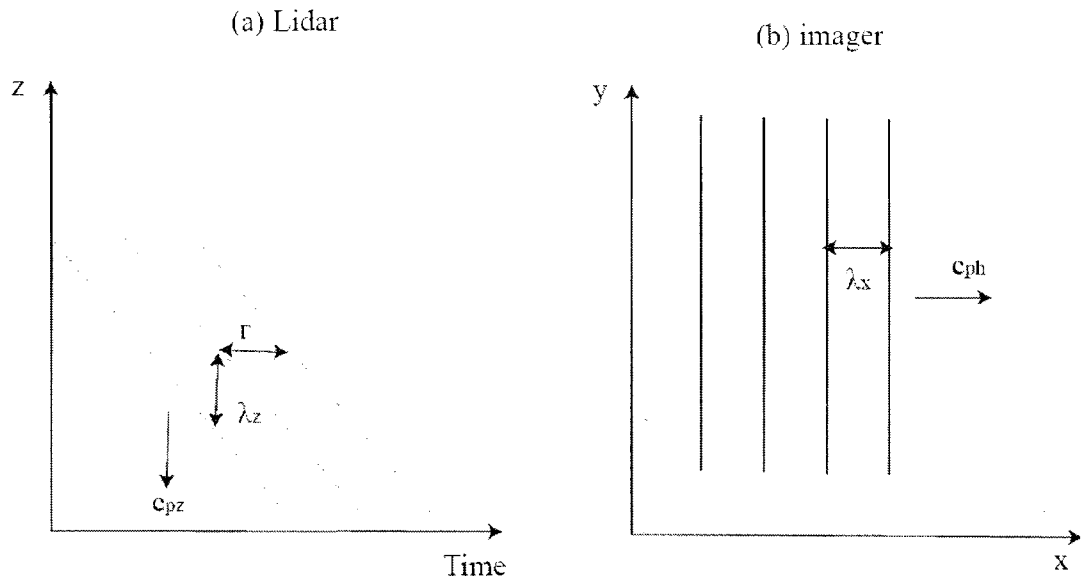


Figure 3.3 Forms of upward propagating gravity waves in the Na lidar and airglow imager data. The gravity wave parameters are included.  $\tau$  is the period.

For high frequency gravity waves, the polarization relations are derived from (3.5)-(3.11) to relate different perturbation amplitudes:

$$\frac{\hat{u}}{\hat{w}} = -\frac{m}{k} \quad (3.16)$$

$$\frac{\hat{u}}{\hat{v}} = \frac{k}{l} \quad (3.17)$$

$$\hat{p} = \frac{\hat{\omega}}{k} \hat{u} = \frac{\hat{\omega}}{l} \hat{v} \quad (3.18)$$

$$\hat{w} = \frac{(m - \frac{i}{2H})\hat{\omega}}{N^2 - \hat{\omega}^2} \hat{p} \quad (3.19)$$

Different measurement technologies may be sensitive to different perturbations. Using these polarization relations, we can deduce the perturbations that a lidar or airglow imager cannot measure.

### 3.3 Gravity wave ducting

Horizontally propagating gravity waves can often be observed in the imager for tens of minutes to a few hours over a large distance. They are believed to be trapped in a duct. It is very important to study and understand ducted gravity waves for their capabilities to transport momentum and energy horizontally. In addition, nonlinearities of gravity waves may be amplified in a duct, as will be discussed in Chapter 4.

Note that the results derived from the linear equations in the last section are based on the assumption of constant  $N$  and  $\overline{u_h}$ . When  $N$  and  $\overline{u_h}$  change quickly with height, the Taylor-Goldstein equation (3.12) is no longer valid. Like other waves, gravity wave reflection may occur at boundaries between media of different  $N$  (or different background), as shown in Fig. 3.4.

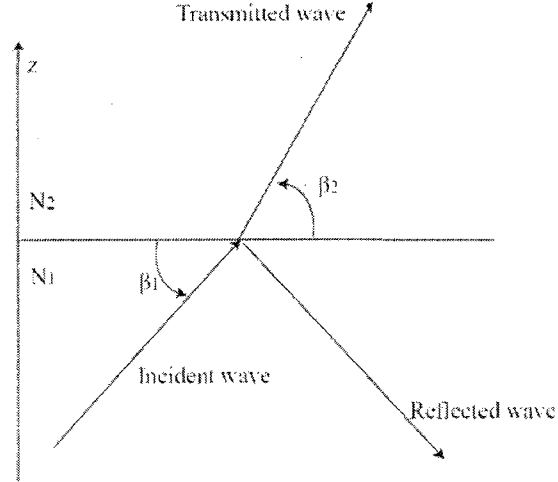


Figure 3.4. Schematic of the gravity wave reflection at the interface of different value of  $N$ .  $\beta_1$ : incident angle,  $\beta_2$ : refraction angle.

Since the wave frequency ( $\omega = N \sin \beta$  following (3.4)) is the same on both sides of the interface between two regions with different temperature structures. The “Snell’s law” for a gravity wave in the atmosphere is:

$$N_1 \sin \beta_1 = N_2 \sin \beta_2 \quad (3.20)$$

To determine how much a wave can be partially reflected, two boundary conditions are specified along with the solutions in (3.12). One is the dynamic boundary condition, i.e., the pressure perturbation is continuous at the interface. The other is the kinematic boundary condition for satisfying continuous vertical mass flux  $\rho w'$ . Then the reflection coefficient  $r$ , defined as the ratio of the amplitude of the reflected wave to the incident wave, is determined as (for a detailed derivation, see Nappo [2002])

$$r = \frac{m_1 - m_2}{m_1 + m_2} \quad (3.21)$$

If the vertical wavenumber  $m_2$  in  $N_2$  medium is zero (when the vertical wavelength is infinite), then  $r$  becomes unity and total internal reflection occurs. If there is no change in the medium, then  $m_1$  is equal to  $m_2$  and  $r=0$ .

An ideal gravity wave duct in the atmosphere is composed of an internal layer ( $m^2 > 0$ ) sandwiched by two evanescent layers ( $m^2 < 0$ ). In this ideal way, the gravity wave may be guided horizontally in the duct (with total reflection inwards and evanescent from the boundaries) and travel thousands of kilometers. Not every gravity wave can be trapped efficiently. Only if the incident and reflected waves are constructively interfering with each other can there be a standing wave. The depth of the duct must be identical to an integer number of half vertical wavelengths of the gravity wave, as shown in Fig. 3.5. The combination of a Na Doppler lidar and airglow imager facilitates the study of gravity wave ducting. The lidar is able to measure the background temperature and wind to give the  $N^2$ ; the imager measures the horizontal wavelength and apparent (measured relative to the ground frame) phase velocity, from which, following (3.14), the profile of  $m^2$  for a ducted wave can be derived. In principle the Na lidar can directly measure the vertical wavelength. Since there often exist a number of gravity waves with different wavelengths data, it is difficult to determine their vertical wavelengths from lidar observation. This situation will be illustrated as part of the mesospheric bore study in Chapter 4.

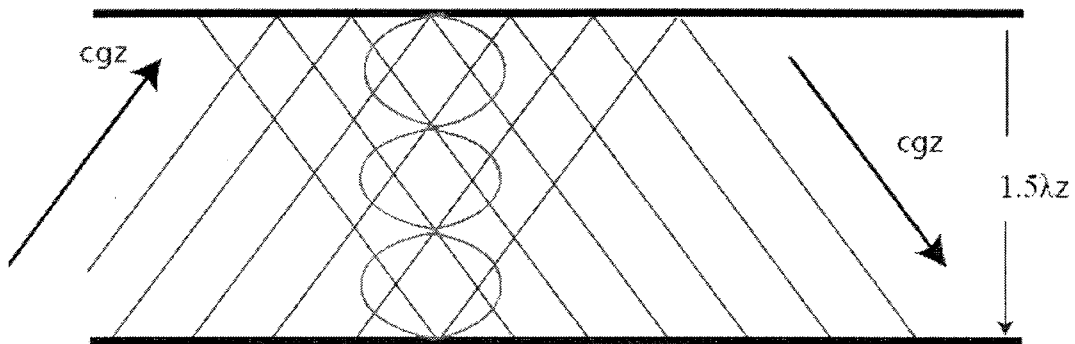


Figure 3.5 Schematic of the second harmonic standing wave. The depth of the duct is  $3 \times 0.5\lambda_z$ .

### 3.4 Gravity wave instability and breaking

When a gravity wave is launched in the lower atmosphere and propagates upward, its amplitude grows exponentially to conserve energy, as seen from (3.11). From linear theory, the wave amplitude could become infinitely large. However, in the real world (and it is nonlinear!), the amplitude is bounded. When the amplitude of the gravity wave is comparable to the mean state, the wave becomes unstable and eventually breaks in the upper atmosphere. Linear theory can estimate the condition for wave breaking, but nonlinear dynamics dominates after wave breaking occurs. Although the term “gravity wave breaking” is used, it does not mean that the gravity wave collapses and disappears. The unstable gravity wave generates large turbulence, and the turbulence in turn dissipates the gravity wave. As a result, the wave amplitude is then clamped and balanced by growth leading to dissipation, thus wave breaking is also called wave saturation. Once wave saturation occurs, the disappearing wave momentum produces a stress (body force), which accelerates or decelerates the mean wind.

To discuss the instability of the atmosphere caused by waves, we assume the background mean state is stable. This is a valid assumption because any unstable state will lose energy and finally reach a steady and stable state. Instability is usually reached by the superposition of mean state and waves with large amplitude in the upper atmosphere based on linear theory. Note that we use “waves” here instead of “gravity waves”, because other types of air oscillations may also induce instability, e.g., solar tidal waves and planetary waves. In this dissertation, we are generally interested in gravity-wave associated instabilities.

Using (3.4), the necessary condition for the air parcel to oscillate around the equilibrium point is when  $N^2$  is greater than 0, which is convective (static) stability. Once  $N^2$  becomes negative, the displacement  $\delta s$  will increase or decrease infinitely, and wave oscillation is no longer supported. Assume the wave perturbation  $T'$  cannot be ignored, and  $N^2 = \frac{g}{T} (dT/dz + \Gamma_a)$ , the atmosphere is convectively unstable where

$$d(\bar{T} + T')/dz < \Gamma_a, \text{ or } d(\bar{\theta} + \theta')/dz < 0 \quad (3.22)$$

From the adiabatic energy equation (3.8) ,i.e.,  $Q = 0$ , and polarization relation (3.17), this condition is equivalent to [Fritts, 1984]

$$u' > c - \bar{u} \quad (3.23)$$

When the gravity wave reaches the instability threshold and breaks, local turbulence occurs or is enhanced. This produces two effects: a drag force on the mean wind and an enhanced eddy diffusion. These results can be expressed as [Holton, 1982]:

$$\frac{\partial u_0}{\partial t} = -\frac{1}{\rho_0} \frac{\partial(\rho_0 \overline{w'u'})}{\partial z} + \frac{\partial(D \frac{\partial u_0}{\partial z})}{\partial z} \quad (3.24)$$

where  $D$  is the eddy diffusivity due to wave breaking. The first term on the right is the vertical divergence of horizontal momentum flux, i.e., the wave stress ( $\text{m/s}^2$ ). The second term is the Reynolds stress, i.e., the turbulence stress. The process is depicted by the cartoon in Figure 3.6. Below the wave breaking level  $z_s$ , the wave amplitude  $u'$  grows with height. Once the wind perturbation satisfies  $u' = c - \bar{u}$ , the gravity wave saturates and drags the mean flow toward the phase velocity of the wave. The closer the mean flow is to the wave phase velocity, the smaller the allowed wave amplitude  $|u'|$ . This process makes the mean wind identical to the wave phase velocity at the critical level of  $c = \bar{u}$ , or the dissipation then ends at the critical level. On the right side of Figure 3.6, the vertical flux of horizontal momentum  $-\rho_0 \overline{w'u'}$  is a constant before wave breaking. When the gravity wave is saturated, the momentum flux diverges and reaches zero at the critical level. On the other hand, the background wind acceleration  $\delta\bar{u}$  decreases above the breaking height. This gravity wave breaking mechanism is employed to explain the zonal wind changes direction in the MLT region in summer and winter. Since 2006, the vertical divergence of the gravity wave zonal momentum flux can be measured directly by the CSU Na lidar [Acott, 2009]. Since the gravity wave momentum flux is not directly relevant to the three topics considered, we have not use the limited result of momentum flux work for this dissertation.

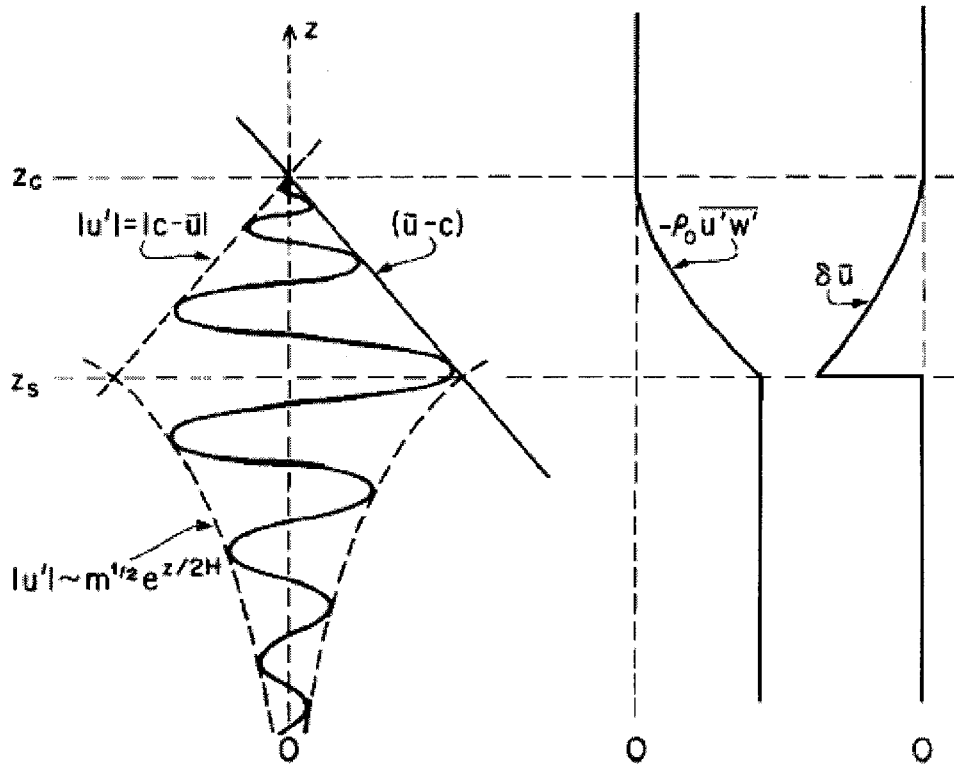


Figure 3.6 Schematic of the amplitude growth with height and saturation of a gravity wave due to convective instability [Fritts, 1984]. Wave damping produces both a divergence of the vertical flux of horizontal momentum and an acceleration of the mean flow toward the phase speed of the wave on the right. Deceleration and diffusion cease at the critical level ( $z = z_c$ ) in linear theory.

The convective instability discussed above is based on the shearless background, i.e., when the background wind  $\bar{u}$  is a constant. In fact, the stratified air can be overturned by the wind shear and the atmosphere becomes dynamically unstable under large wind shears. The Richardson number defined below can be used to characterize the stability of the atmosphere in this case:

$$Ri = \frac{N^2}{(\partial u_h / \partial z)^2} \quad (3.25)$$

The necessary but not sufficient condition for dynamic instability is  $0 < Ri < 1/4$ . The equivalent condition for convective instability is  $Ri < 0$ . The derivation for the dynamic stability condition can be found in Nappo [2002]. Similar to convective instability, dynamic instability also induces turbulence and causes gravity wave breaking and dissipation.

### 3.5 Gravity wave filtering

As introduced in Chapter 1, the counter-intuitive structure of cold summer and warm winter is due to the seasonal variation of the gravity wave momentum flux in the middle atmosphere. Gravity wave filtering was also mentioned in the last section. Wind filtering changes the gravity wave spectrum as the gravity wave moves from the lower atmosphere to the mesopause region. A gravity wave is filtered out, i.e., no longer propagates upward, when its horizontal phase velocity  $c$  is equal to the mean horizontal wind  $\overline{u}_h$ . From the Taylor-Goldstein equation of (3.12),  $c = \overline{u}_h$  is a singularity and no simplified solution can be derived. But we can see the effect when  $\overline{u}_h$  is approaching  $c$ , i.e.,  $\overline{u}_h = c + \frac{du_h}{dz} \delta z$ . Assuming the wind shear  $S = \frac{du_h}{dz}$  is a constant value, the gravity

wave dispersion relation, (3.13) can be rewritten as:

$$m^2 = \frac{N^2}{(c - \overline{u}_h)^2} - k_h^2 - \frac{1}{4H^2} = \frac{N^2}{(S\delta z)^2} - k_h^2 - \frac{1}{4H^2} \quad (3.26)$$

Now  $m^2$  becomes infinitely large when  $\delta z$  approaches zero, and as a result,  $\lambda_z = 2\pi/m$  is close to zero near the critical level. When the wind shear induced by the gravity wave becomes very large, the Richardson number becomes very small and dynamic instability

occurs. The amplitude of the gravity wave  $w'$  is gradually dissipated as shown in Figure 3.7. By (3.26), when  $m^2$  is infinitely large, the vertical group velocity is zero. The wave packet can never propagate beyond the critical level.



Figure 3.7. When a gravity wave approaches the critical level,  $w' \rightarrow 0$  and  $\lambda_z \rightarrow 0$  [Nappo, 2002, pp121].

Chapter 3 has established the foundation of gravity wave theory. We drew conclusions based mainly on linear theory. The atmosphere is inherently nonlinear in the real world. But linear theory simplifies it and provides good guidance to explain many phenomena. In the linear theory, the wave-wave, gravity wave-tides, gravity wave-planetary wave interactions are ignored. Hence, a single gravity wave is usually considered at one time. In the real atmosphere, there are many gravity waves coexisting along with other waves, making the study of atmospheric stability more complicated. However armed with this general understanding of gravity waves, in Chapter 4 we can proceed to study the three phenomena in the mesopause observed by the Na lidar and airglow imager: concentric gravity waves, mesospheric bores and large wind shears.

## References:

- Acott, P. E., Mesospheric momentum flux studies over Fort Collins CO (41N, 105W), *Ph.D. Dissertation*, Colorado State University, 2009.
- Fritts, D. C. and M. J. Alexander, Gravity wave dynamics and effects in the middle atmosphere, *Rev. Geophys.*, vol.41, No.1, doi:10.1029/2001RG000106, 2003.
- Fritts, D. C., Gravity wave saturation in the middle atmosphere: a review of theory and observations, *Rev. Geophys.*, 22(3), 275-308, 1984.
- Hines, C. O., Internal atmospheric gravity waves at ionospheric heights, *Can. J. Phys.*, 38(11), 1441-1481, 1960.
- Holton, J. R., The Influence of Gravity Wave Breaking on the General Circulation of the Middle Atmosphere, *J. Atmos. Sci.*, 40(10), 2497-2507, 1983.
- Holton, J. R., An introduction to Dynamic Meteorology, International Geophysics Series, Volume 48, Elsevier Science (USA), Academic Press, 1992.
- Kelley, M. C., M. F. Larsen, C. LaHoz, J. P. McClure, Gravity wave initiation of equatorial spread F - A case study, *J. Geophys. Res.*, 86, 9087-9100, 1981.
- Nappo, C. J., An introduction to atmospheric gravity waves, International Geophysics Series, Volume 85, Elsevier Science (USA), Academic Press, 2002.

## **Chapter 4: Measurement Results: Concentric gravity waves, mesospheric bores and large wind shears**

Between September 2003 and August 2008, the Yucca Ridge OH airglow imager was operational. Since May 2002, the CSU Na lidar has been able to measure wind and temperature on a 24-hour continuous basis. There are 132 nights of simultaneous OH imager and Na lidar observations available. Longer-period gravity waves and tides can be observed by the lidar and shorter-period gravity waves can be observed by the imager. However, on nights without lidar in operation, interesting wave related phenomena are often observed by OH imager alone. With a large imager (>700 nights) and Na lidar (>250 nights) database, we conducted three projects to study and help to understand the dynamics in the mesopause. These three projects are related to interesting, yet not understood phenomena: propagation of concentric gravity waves, generation of mesospheric bores and confinement of large wind shears. As a result, Chapter 4 has three sections.

The study of concentric gravity waves allows us to understand the generation and propagation of gravity waves. The investigation of mesospheric bores gives a good example of wave ducting and its impact. The statistical study of large wind shears shows the importance of wave breaking in limiting the wave amplitude. Linear theories of

gravity waves are heavily relied to explain what we have observed. Although atmosphere dynamics is nonlinear in the real world, the linear theories successfully help us to understand and explain a lot of observations.

The structure of this chapter is organized in the format of three distinct scientific papers, one for each section. The work on concentric gravity waves has been published recently [Yue et al., 2009], along with a accompanying theory paper by Vadas et al. [2009], and section 4.1 summarizes the key findings of Yue et al. and their relationships to Vadas et al. Section 4.2 is based on the paper, “Mesospheric bore formation from large-scale gravity wave perturbations observed by collocated all-sky OH imager and sodium lidar” by Yue et al. submitted to Journal of Atmospheric, Space and Terrestrial Physics; it is now in revision. Section 4.3 is based on the paper, “Large wind shears and stabilities in the mesopause region observed by Na lidar at midlatitude” by Yue et al. in preparation; it will be submitted for publication after this thesis is completed and approved.

#### **4.1 Concentric gravity waves**

Along with topography and wind shear, convection is one of the dominant lower-atmospheric mechanisms for the generation of gravity waves. Convection can generate gravity waves if upward moving air in the unstable troposphere “overshoots” the tropopause by ~1-3 km into the stably-stratified stratosphere and then collapses back down to the tropopause [Pierce and Coroniti, 1966]. Several models developed in the last decade have simulated convectively-generated gravity waves in three dimensions, greatly improving our understanding of the characteristics of gravity waves excited by this mechanism [Piani et al., 2000; Horinouchi et al., 2002; Lane et al., 2003; Alexander et al.,

2004; Vadas and Fritts, 2008]. In general, all of these models show that convectively generated gravity waves generated in the troposphere have conically shaped phase surfaces when the intervening winds between the lower atmosphere and middle atmosphere are small or zero. Therefore, for gravity waves propagating upward and horizontally from a point source (i.e., deep convection), in a horizontal plane, the waves and associated perturbations of trace species, such as the OH emission intensity, appear as outward, horizontally-propagating concentric circular rings if the intervening winds are zero [Vadas and Fritts, 2008].

Among the 723 clear nights of data from fall 2003 to fall 2008, concentric gravity waves were observed on 9 nights by the Yucca Ridge OH imager. We discuss the concentric gravity waves observed on 11 May 2004 first.

#### **4.1.1 Case study of 11 May 2004 concentric gravity waves**

Beginning at 0340 UT (2140 Local Time) on 11 May 2004 (UT day 132), curved wave patterns moved away from a center in the southeast corner of the raw OH images. The widths of the curved wave bands decreased with time and were gone at ~0510 UT (2310 LT). Selected flat-field OH images of the 11 May 2004 case are shown in Figure 4.1. In the 0350 UT image, for example, ~5 nearly complete circles of bright wave fronts were observed. However, the inner 4 rings appear to have a different center than the outer ring at this time. We fit each ring with circles of varying radii and centers, and overlay them as four red dashed circles (inner rings) and one blue dashed circle (the outer ring) in this image of Figure 4.1. The centers of the concentric gravity waves are denoted as red and blue solid dots, respectively. Note that the inner 4 circles have one center, and

the outer ring has a different center; this suggests that one convective plume is the source of the inner rings, while a second convective plume is the source of the outer ring. We also performed this procedure for the images at 0400 and 0430 UT in Figure 4.1, overlaying red and blue dashed circles on the inner and outer rings of each image, respectively. We see that the locations of the centers of the inner and outer rings, denoted by red and blue dots, respectively, are in approximately the same locations in each of the images; therefore, the geographic locations of the centers of the inner and outer concentric gravity waves are approximately fixed in time. We name the inner (red) and outer (blue) concentric gravity waves as CGW1 and CGW2, respectively. In this section we will show that the centers of CGW1 and CGW2 correspond to the location of two deep convective plumes which were active  $\sim 1$  hour earlier, in good agreement with theory when the intervening winds are small [Vadas et al., 2008b].

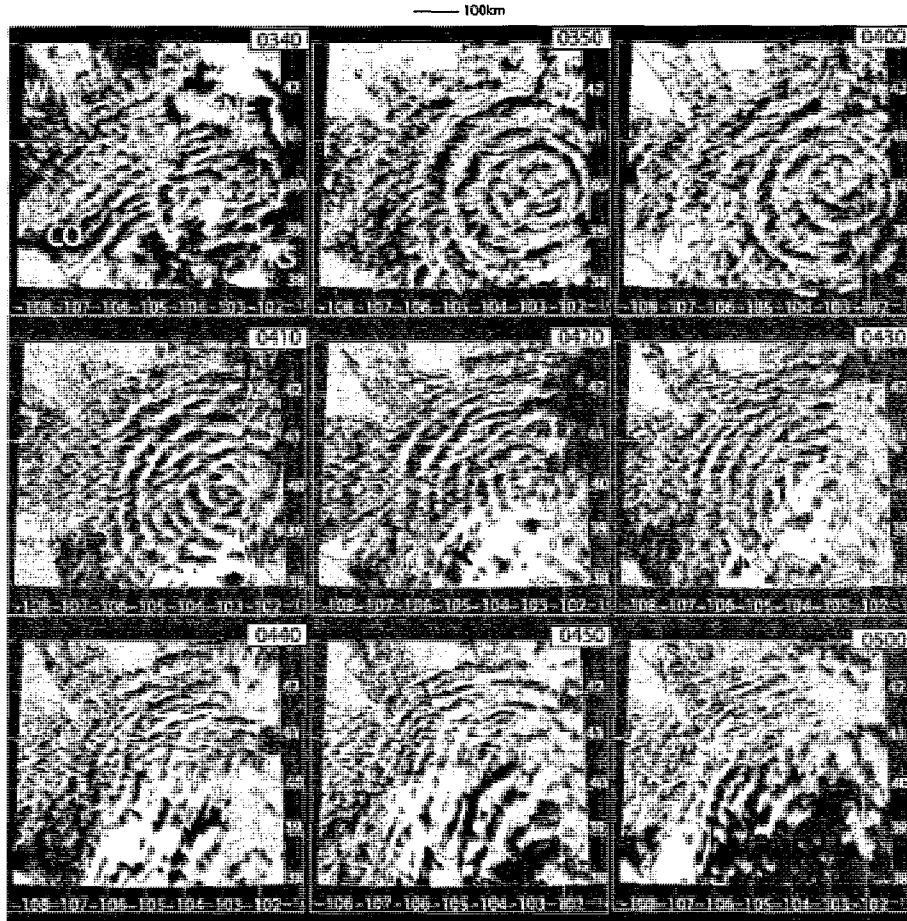


Figure 4.1. Time sequence of difference OH images in geographic coordinates from 0340 to 0500 UT on 11 May 2004 covering parts of Wyoming, Nebraska, Colorado and Kansas. The top left graph shows the state borders in yellow dashed lines. The red star denotes the location of the OH imager at Yucca Ridge Field Station. The UT time of each image is shown the upper right corner. Longitudes and latitudes are shown on the right and lower axes, respectively. The red and blue dashed circles denote CGW1 and CGW2, respectively, with estimated centers shown as red and blue solid dots.

Figure 4.2 shows OH images of the CGWs which were observed on the other 8 nights: 28 August 2005, 07 September 2005, 08 September 2005, 04 May 2007, 03 June 2008, 26 August 2008, 30 August 2008 and 04 September 2008. These images display a rich variety of shapes and types of concentric gravity waves. In some cases, for example, 04 May 2007 and 03 June 2008, these concentric gravity waves appear as portions of

ellipses rather than circles. Note that the fronts are quite distorted on many of these nights, implying large intervening winds [Vadas et al., 2008b].

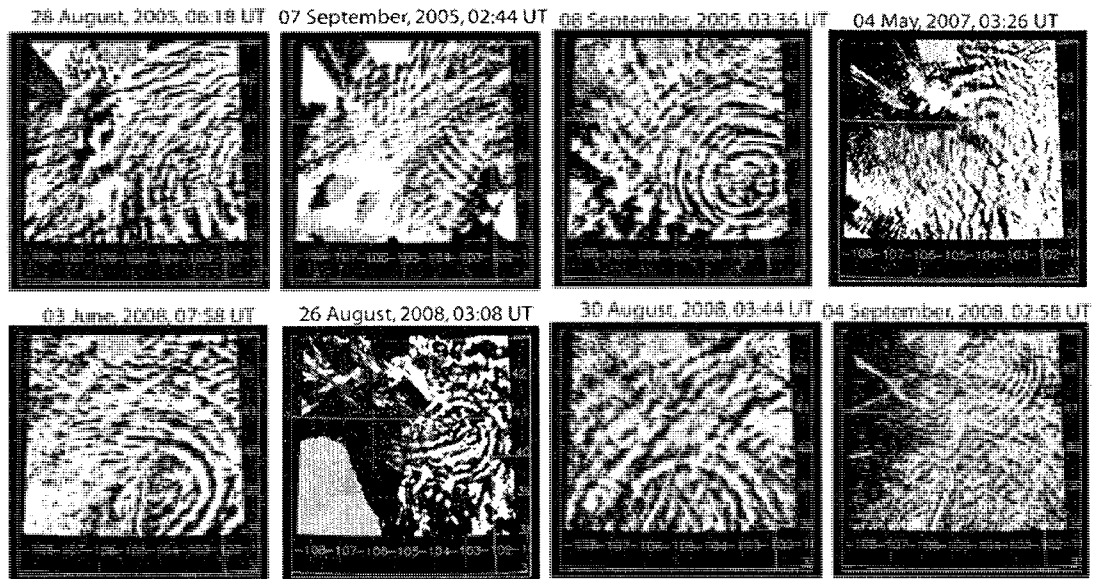


Figure 4.2. CGW OH images from eight nights. Upper row (from left to right) shows the nights of 28 August 2005, 07 September 2005, 08 September 2005, and 04 May 2007, respectively. The lower row (from left to right) shows the nights of 03 June 2008, 26 August 2008, 30 August 2008, and 04 September 2008, respectively.

#### 4.1.2. Convective sources

Gravity waves can be generated when a convective updraft “overshoots” the tropopause by 1-3 km into the stably-stratified stratosphere [Pierce and Coroniti, 1966; Larsen and Swartz, 1982; Lane et al., 2003]. On the night of 11 May 2004, the tropopause height was 12 km, as measured by the radiosonde launched from Denver/Stapleton, CO (39.75°N, 104.87°W). Figures. 4.3(a) and 4.3(b) show the 0305 UT reflectivity images from the Goodland, Kansas (39.2N, 101.4W) National Weather Service WSR-88D NEXRAD Doppler radar. The convective overshoots are indicated by

high reflectivities at altitudes 1-3 km above the tropopause. The centers of plume1 at (40.0°N, 103.0°W) and plume2 at (39.6°N, 103.8°W) are marked by red and white circles in Figure 4.3. Fig 4.3(c) shows the echo-top chart with the same red and white circles at the same time. Here, the echo-top is the largest altitude at which the reflectivity exceeds the minimum significant reflectivity of 18.5 dBZ, thereby showing the regions of convective overshoot. Fig 4.3(c) shows that the regions of convective overshoot occur at the same latitudes and longitudes (lat/long) as in the reflectivity images shown in Figures. 4.3(a) and 4.3(b). Using this information, as well as the results from the propagation time study we report in the next section, we conclude that plume1 and plume2 are the sources of the CGW1 and CGW2 patterns, respectively. Model studies confirm that if the winds are zero, the apparent center of the concentric rings near the mesopause exactly coincide with the location of the convective plume [Vadas and Fritts, 2008]. If the intervening winds are much larger than ~20-30 m/s, however, the apparent center of the concentric rings are shifted significantly with respect to the location of the convective plume [Vadas et al., 2008b]. We also note that similar “overshooting” updrafts are observed in visible-band GOES12 satellite images three or four hours earlier (prior to sunset) for the same storm system, but at different locations [Vadas et al., 2008b].

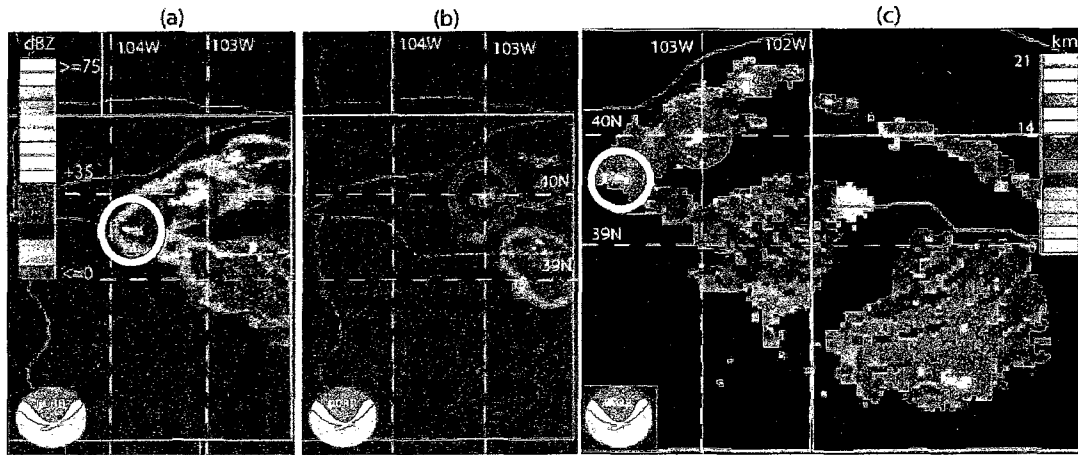


Figure 4.3. (a) and (b): NEXRAD reflectivity charts observed at Goodland, KS, at 0305 UT, on 11 May 2004, at elevation angles of  $4.13^\circ$  and  $5.14^\circ$ , respectively. (c): NEXRAD echo top height chart, also from Goodland, KS, at 0305 UT. Centers of the red and white circles are the locations of plume1 and plume 2, respectively. The altitudes of plume1 and plume2 are 12 km and 14 km, as determined from the distances and elevation angles in (b) and (a), respectively. The colors in the reflectivity charts (a) and (b) indicate reflectivity in dBZ, and those in the echo-top chart (c) indicate altitude in km.

Figure 4.4 shows NEXRAD reflectivity measurements recorded prior to the observations of CGWs on the same nights shown in Figure 4.2. We also project some of the CGW arcs and rings from Figure 4.2 onto the corresponding radar maps. Despite the variation in propagation times between the radar maps in Figure 4.4 and the OH images in Figure 4.2, the approximate centers of the CGWs coincide with the location of the convective plumes reasonably well. Because these storms tend to move less than a few degrees in latitude or longitude per hour, and because these storms tend to create new convective updrafts continually by moving away from expended regions and into regions of higher convective available potential energy (CAPE), the CGWs shown in Figure 4.2 were likely excited by convective plumes from the same storm systems shown in Figure 4.4, although the actual convective plumes that excited the particular waves observed in Figure 4.2 may have occurred earlier or later than those shown in this figure, as we did

not perform a detailed comparison with wave propagation times and wavelengths, as we have done for the 11 May 2004 case (see the next section).

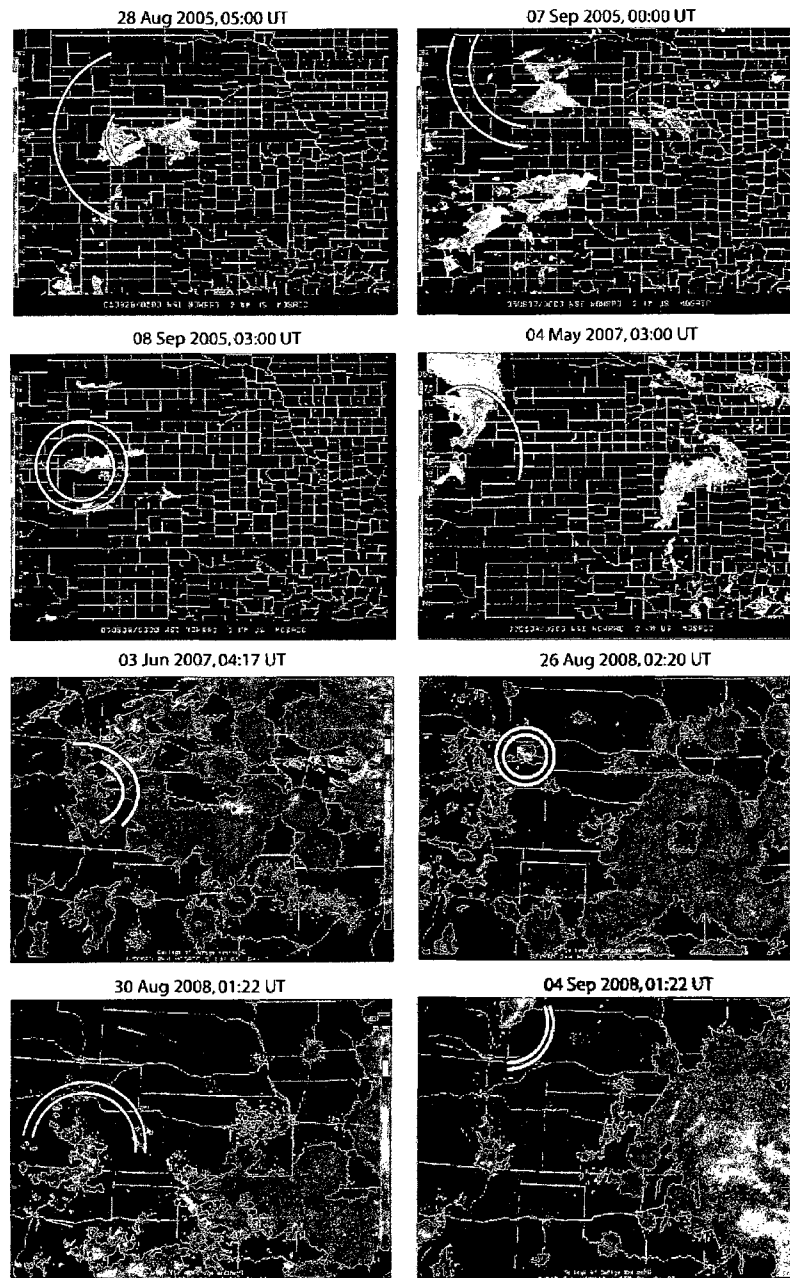


Figure 4.4. NEXRAD reflectivity maps recorded on the same nights on which CGWs were observed, as shown in Fig. 4.2. Some of the arcs and rings of CGWs in Fig.4.2 are projected onto the radar maps.

#### 4.1.3 Analysis of CGWs using the gravity wave dispersion relation

Convective plumes excite CGWs with a large range of spatial and temporal scales [Alexander et al., 1995; Lane et al., 2003; Vadas and Fritts, 2008]. In this part, the spatial and temporal scales of the CGWs observed on 11 May 2004 are analyzed and compared with the predictions of the Boussinesq internal gravity wave dispersion relation of (3.13) and the using zero winds. The spatial and temporal scales (as a function of radius from the center of the CGW1),  $\lambda_h$  and  $\tau$ , respectively, can be explained reasonably well with this dispersion relation (3.13). Additionally,  $\alpha$  is the angle in a vertical plane between the vertical line and surfaces of constant phase of the CGW at a distance  $R$  away from the observed center of the CGW at  $\sim 87$  km in altitude. Because the gravity wave generation mechanism considered here is convective overshoot, we assume that the gravity waves are launched from the tropopause. This is a good assumption because the fluid below the tropopause is generally unstable when convection is occurring, and therefore cannot support the propagation of gravity waves within the immediate plume vicinity. On the night of 11 May 2004, the tropopause is at 12 km altitude using the temperature profile measured by the Denver radiosonde. This altitude is typical at midlatitude during this season and is the same as that calculated by Fovell et al. [1992]. We denote  $\Delta z$  to be the vertical distance between the tropopause and the OH layer. Given that the average OH layer is at 87 km,  $\Delta z$  is  $87 - 12 = 75$  km. Using the relation  $\tan \alpha = R/\Delta z$ , along with (3.13) and the assumption that  $N$  has a constant value of  $2\pi/5 \text{ min}^{-1}$  ( $N^2$  is averaged as  $\sim 0.0004 \text{ s}^{-2}$  in the middle atmosphere [Hecht, 2004]) with altitude, the period  $\tau$  of a GW can be expressed in terms of  $R$  as:

$$\omega^2 = \frac{N^2 k_h^2}{k_h^2 + m^2} = N^2 \cos^2 \alpha \quad (4.1a)$$

$$\tau = \frac{2\pi}{N} \sec \alpha = \frac{2\pi}{N} \sqrt{1 + \frac{R^2}{\Delta z^2}}. \quad (4.1b)$$

Note that (4.1) implicitly assumes that the background winds are zero, the temperature is constant with altitude, and the Boussinesq assumption holds, i.e., that  $\lambda_z \ll 4\pi H$ , where  $H \sim 7$  km is the density scale height. This simple relation, (4.1), is plotted as a solid curve in Figure 4.5(a). Note that this relation is independent of the time to propagate from the tropopause to the OH layer, because all gravity waves with the same frequency propagate at the same angle from the vertical line. The apparent period  $\tau$  of CGW1 was measured using the sequential images in Figure 4.1. The measured period is actually the time between two consecutive crests or troughs at the same location. The time for the measurement is centered between two images. Since the imager records an image every 2 min, the uncertainty of the  $\tau$  measurements is estimated to be  $\pm 2$  min. Because CGW2 has a relatively large margin of error, it is excluded from Figure 4.5(a). The periods of CGW1 are measured as a function of radius from the center of CGW1 along a line  $\sim 45^\circ$  to the northwest of the center of CGW1, since the rings are the clearest along that line. The periods of CGW1 are measured at 0400 and 0420 UT, illustrated as blue and red dots, respectively, in Figure 4.5(a), with error bars. Although both observed and predicted periods,  $\tau$ , increase as the radius increases, (4.1) (with zero background winds and constant temperature with altitude) predicts periods larger than the observed periods. Slightly better agreement with the observed periods is obtained via ray-tracing simulations where anelastic effects (i.e., not neglecting  $H$ ) are included [Vadas et al., 2008b]. The zero-wind assumption also affects the interpretation of the radius,  $R$ . When the winds are zero, the geographic location of the convective plume that excites the

CGWs is the same as that of the center of the CGWs at the OH layer. However, when the intervening winds are much larger than  $\sim 20\text{-}30$  m/s, the apparent center of the CGW is offset significantly from the location of the convective plume [Vadas et al., 2008b]. In this case, plume 1 is at  $(40.0^\circ\text{N}, 103.0^\circ\text{W})$ , while the center of CGW1 is at  $(40.0^\circ\text{N}, 102.8^\circ\text{W})$ . Since the plume and the center of CGW1 are within 15 km of each other, the intervening winds are likely of order or smaller than  $\sim 20\text{-}30$  m/s. In the next section, we will show that the horizontal winds from the radiosonde and the Thermosphere-Ionosphere-Mesosphere-Electrodynamics General Circulation Model (TIME-GCM) are smaller than 20 m/s on 11 May 2004. Therefore, the zero-wind assumption we use here is reasonable.

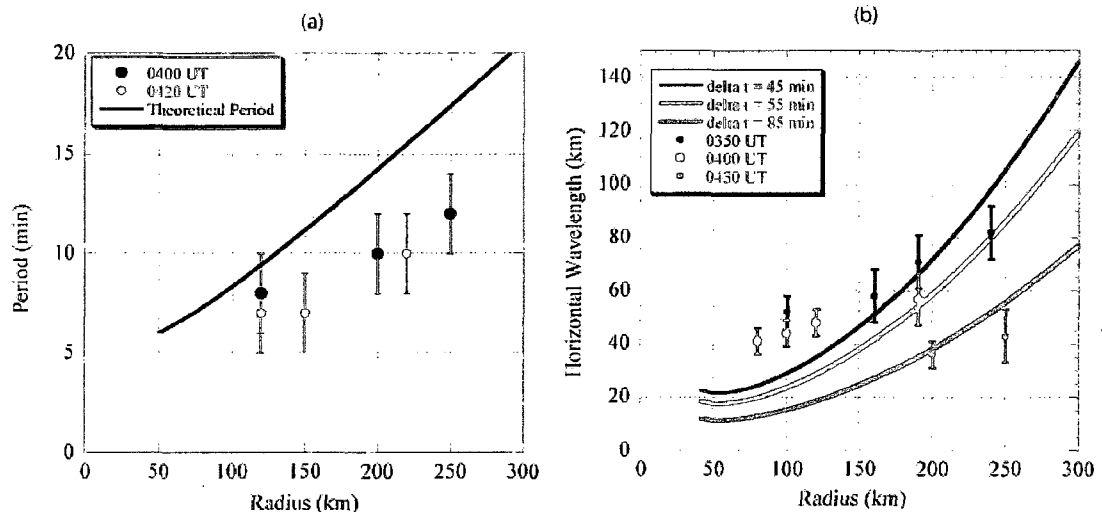


Figure 4.5. Temporal and spatial variations of CGW1 observed on 11 May 2004. (a) Observed wave periods (dots) compared to those calculated using dispersion relations (solid curve) as a function of radius: blue and red dots are the measured periods at 0400 UT and 0420 UT, respectively. (b) Horizontal wavelength  $\lambda_h$  as a function of both radius and time: dots are measured values. Blue, red and green curves are calculated from the GW dispersion relation for propagation times,  $\Delta t$  of 45, 55 and 85 min, respectively, between when the convective plume is generated near the tropopause and when CGWs were observed by the OH imager.

The observed horizontal wavelengths at the OH layer altitude of ~87 km depend on the propagation time,  $\Delta t$ , of the gravity waves from their excitation by the convective plume to their observation location within the OH layer. This propagation time in turn depends on the vertical group velocity  $c_{gz}$  which is a function of  $\alpha$ :

$$c_{gz} = -\frac{Nk_h m}{(k_h^2 + m^2)^{3/2}} = -\frac{N \tan \alpha}{k_h \sec^3 \alpha}. \quad (4.2)$$

in which the relations  $m = k_h \tan \alpha$ , and  $k_h^2 + m^2 = k_h^2 \sec^2 \alpha$  have been used. Again assuming zero winds, the time it takes for a gravity wave to propagate from the tropopause to the OH layer is  $\Delta t = \Delta z / |c_{gz}|$ . Taking the absolute value of (4.2) and substituting  $\Delta z / \Delta t$  for  $c_{gz}$ , the gravity wave horizontal wavelength,  $\lambda_h$ , as a function of radius,  $R$ , and propagation time,  $\Delta t$ , is:

$$\lambda_h = \frac{2\pi R^2 (1 + \Delta z^2 / R^2)^{3/2}}{N \Delta z \Delta t}. \quad (4.3)$$

We measure the average horizontal wavelength,  $\lambda_h$ , of CGW1 as a function of radius at 0350, 0400 and 0430 UT along a line ~45° toward the northwest of the center of CGW1. (This is the same line as was used to measure the observed periods of CGW1). The  $\lambda_h$  values are manually measured to be the distance between two consecutive wave crests or troughs in the images. The radius  $R$  used in each measurement is then the midpoint between two crests or two troughs. The uncertainties in  $\lambda_h$  are quantitatively measured depending on how clear the wave front is. This is due to the wave interference and noise (thin clouds, city light, Milky Way, etc.). This is because the wave front sometimes is shown as a band instead of a sharp line. These measurements are plotted as dots in Figure 4.5(b). Since plume1 overshoot the tropopause at 0305 UT, the corresponding gravity

wave propagation times,  $\Delta t$ , are 45, 55 and 85 minutes for the OH imager observation times of 0350, 0400 and 0430 UT, respectively. The horizontal wavelengths derived from (3.3) as a function of  $R$  for  $\Delta t = 45, 55$  and  $85$  min are plotted as blue, red, and green solid lines, respectively, in Figure 4.5(b). The observed horizontal wavelengths for CGW1 at different  $\Delta t$  are in general agreement with the gravity wave dispersion relation for zero winds, since  $\lambda_h$  increases as  $R$  increases at a given  $\Delta t$ , and  $\lambda_h$  decreases with time at a fixed radius  $R$  [Vadas and Fritts, 2008]. A discrepancy exists because the observed  $\lambda_h$  is larger than the zero wind theory results for  $R < 150$  km and is typically smaller for  $R > 200$  km. We have also determined  $\lambda_h$  for CGW2 at 0400 for two radii from its center (blue dot in Figure 4.1): they are 77 and 102 km for  $R = 190$  km and 260 km, respectively. Within error bars, these values are consistent with the simple prediction (red curve) in Figure 4.5(b). Better agreement is obtained for radii  $R < 150$  km using realistic convective spectra, realistic winds, and an anelastic dispersion relation [Vadas et al., 2008b].

The vertical wavelengths  $\lambda_z$  of CGW1 are calculated using (3.13) with the assumption that the background winds are zero. The resulting vertical wavelengths are  $\sim 20 - 40$  km. This is greater than twice the vertical thickness ( $\sim 8$ km) of the OH emission layer. From Liu and Swenson [2003], the cancellation factor for OH emission and for vertical wavelengths of 20 - 40 km is 2 - 3. Therefore, we estimate that the OH airglow intensity perturbations are reduced by  $\sim 20 - 45\%$  for CGW1 compared to GWs with infinitely large vertical wavelengths.

#### 4.1.4. Seasonal and background wind conditions and CGW observations

Although gravity waves are often observed by airglow imagers as quasi-monochromatic, quasi-linear, parallel-phase fronts with horizontal wavelengths limited by the typical range of resolution of all-sky imagers (20 – 500 km), concentric gravity waves are rarely observed. The monthly distribution of the 723 clear nights of data from September 2003 to September 2008 is shown as a histogram in Figure 4.6(a). The observations are fairly uniform throughout the year. Figure 4.6(b) shows the monthly distribution of CGW observations. Nearly concentric CGWs were observed by the Yucca Ridge OH imager only on 11 May 2004, 28 August 2005, 07 and 08 September 2005 and 04 May 2007, 03 June 2008, 26 and 30 August 2008, 04 September 2008. Therefore, 8 out of these 9 events were observed ~2 months after the spring equinox and ~0.5 - 1 months before the fall equinox. Comparing with Figure 4.6(a), we see that the seasonal distribution of CGWs is not caused by a skewed monthly distribution of the clear-night imager data. The occurrence frequency of CGW observations is very low ( $9/723 \approx 1.5\%$ ). The peaks of CGW observations occur in May and in August-September, which are ~3-4 months apart.

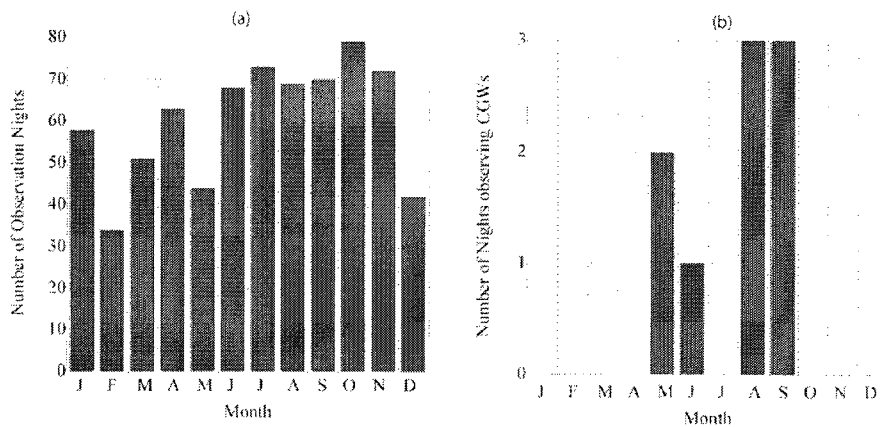


Figure 4.6. (a) Monthly distribution of clear observation nights of the OH imager from 2003-2008. (b) Monthly distribution of CGW observations during the same period.

We now discuss a possible reason as to why the CGWs are primarily observed in May and in August-September. The zonal and meridional mean winds between 35 and 90 km at 42°N are shown in Figure 4.7(a) and 4.7(b) from a recent climatology run of the TIME-GCM by Dr. Hanli Liu at NCAR. The zonal mean winds are weaker than 20 m/s (because they switch direction) from April 15-May 15 and August 15-September 15, which are approximately ~4 months apart [Roble, 1995]. Therefore, if the planetary and tidal waves happen to be weak (which may only occur on certain days and at certain local times), and if the mean winds above the tropopause are weak, then the total winds from the tropopause to the upper mesosphere may be weak. (We show that this is the case for the 11 May 2004 example below using radiosonde and TIME-GCM data.) This is consistent with the suggestion by Suzuki et al. [2007], that weak horizontal winds appear to be a necessary condition for the observation of CGWs in the mesopause region. The total horizontal wind speed is shown in Figure 4.7(c), obtained from Figure 4.7(a) and (b). Weak total winds with speeds < 20 m/s are seen from April 15-May 15 and from August 15-September 15. The weak climatological winds may explain why the occurrence distribution in Figure 4.6(b) is double-peaked during these spring and fall months. Additionally, peak thunderstorm season over Eastern Colorado is from late April through early September. Therefore, the seasonal dependence of convective sources near YRFS, Colorado, constrains the occurrence of CGWs to be from May to September.

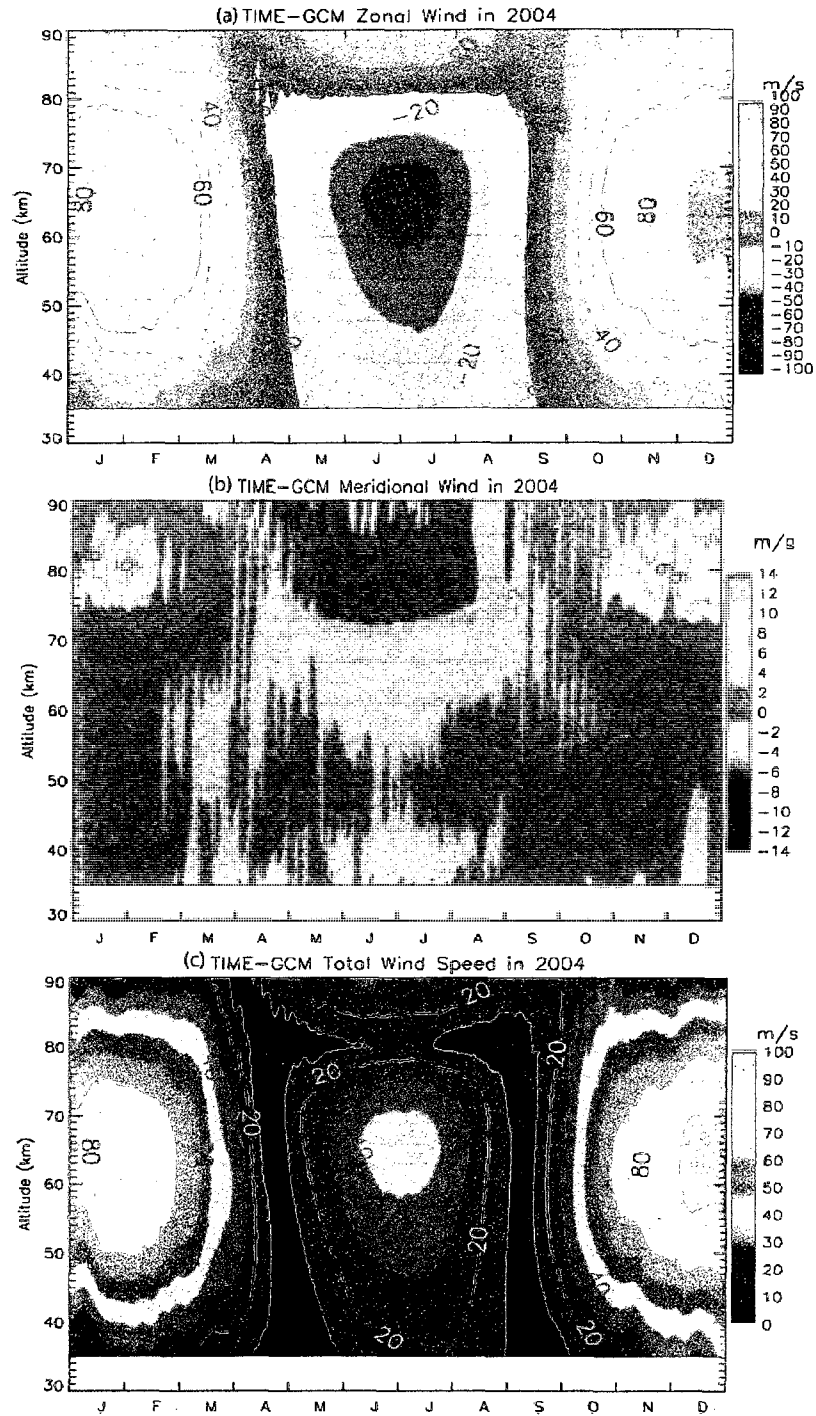


Figure 4.7. TIME-GCM zonal-mean horizontal wind climatology at 42° N for 2004. (a).Zonal wind (b) Meridional wind (c) Total horizontal wind speed.

As shown in Figure 4.6(b), 8 of the 9 CGW events were observed in May or late August/early September when the total climatological wind speed above the tropopause is low. The CGWs reported by Sentman et al. [2003] occurred on 19 August at a nearby location with a similar latitude/longitude.

The only case of the 9 CGW observations that did not occur during the period when the mean climatological winds are  $< 20\text{m/s}$  was 03 June 2008. On that night, however, it is possible that the total wind (with the planetary wave, tidal, and other wave contributions) was unusually weak.

Since tidal and planetary waves, as well as lower stratospheric winds from weather systems, can significantly increase the hourly winds from the weak monthly mean wind, we examine the wind profiles for these 9 cases. Figure 4.8(a) and (b) show the horizontal wind profiles at 0 UT on 11 May 2004 from the ground to 90 km. Figure 4.8(a) shows the Denver radiosonde winds, while Figure 4.8(b) shows the TIME-GCM winds at the time of the CGW observations. The maximum wind speed below 87 km is no greater than  $\pm 20\text{ m/s}$ . Therefore, we infer that the combined planetary and tidal winds are small at the time the CGWs were observed on 11 May 2004. It is worthwhile to mention that there are many nights with convective storms nearby and low winds but no CGWs were observed. This shows that the deep convection and low wind are the necessary but not sufficient conditions for the OH imagers to see the CGWs.

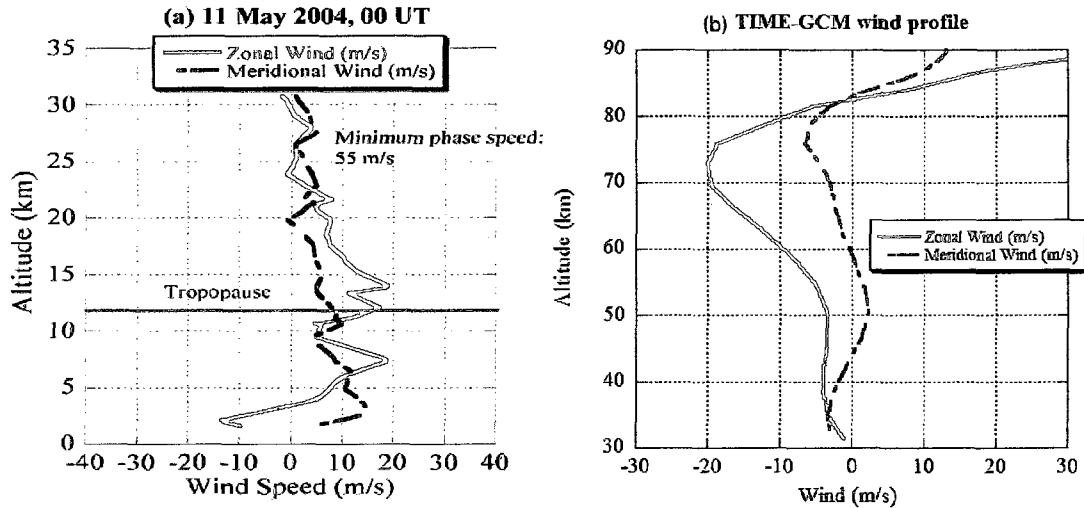


Figure 4.8. (a) Radiosonde wind (0-30 km) and (b) TIME-GCM wind (30-90 km) both at 0 UT on the night of 11 May 2004. The height of the tropopause is marked by a green line in (a). The minimum horizontal phase speed of the CGWs is labeled.

The wind observed by the same Denver radiosondes (with altitude ranges of ~0 – 30 km) are shown in Figure 4.9 for the other nights when 6 of the CGWs were observed. The sounding failed above the tropopause on 26 August, 2008; no radiosonde data is available on 30 August 2008 and 04 September 2008. These soundings are only available at 0 and 12 UT. Only the soundings at 0 UT is shown because the 0 UT soundings are closer to the times of the convection. For all of these cases, the horizontal wind speeds above the tropopause (where the CGWs propagate) were smaller than ~ 30 m/s. The apparent minimum horizontal phase speeds of these CGWs labeled on each graph are 50 - 120 m/s, much larger than the winds from 12-30 km. Although obtaining TIME-GCM winds for these 8 cases is beyond the scope of this paper, the radiosonde data along with the detailed 11 May 2004 data/model winds provide evidence that weak background horizontal winds permit the propagation of CGWs into the mesopause region with relatively little filtering and distortion at those altitudes, allowing the CGWs to appear as

rings or arcs in the OH layer. Indeed, Vadas et al [2008b] find that the concentric rings near the mesopause are “squashed” or arc-like if the intervening zonal winds are much larger than  $\sim 20\text{-}30$  m/s and the meridional winds are zero. If the intervening winds are zero, the gravity waves appear as perfectly concentric rings near the mesopause. If the intervening winds are less than  $\sim 30$  m/s, the gravity waves appear mostly as concentric rings, although portions of the rings may disappear at late times because of wave reflection and critical level absorption.

We now connect the shape of the arcs and concentric CGWs in Figure 4.1 and 4.2 with the horizontal winds in the troposphere in Figure 4.8(a) and 4.9. On 11 May 2004, 08 September 2005 and 26 August 2008, the CGWs are  $360^\circ$  circular rings, while on 04 May 2007 and 03 June 2008, the CGWs are arcs. Simulations show that if a convective plume is moving vertically through zero wind, then perfectly circular rings of gravity waves are generated [Vadas and Fritts, 2008; Vadas et al., 2008b]. However, convective plumes in a wind shear environment result in the generation of an asymmetric spectrum of gravity waves, with gravity waves propagating mainly in the rearward direction of the storm propagation direction [Fovell et al., 1992; Lane et al., 2001]. Additionally, concentric CGWs propagating through large-scale winds (such as the QBO) become anisotropic, resulting in only half of the rings being visible [Piani et al., 2000]. Finally, a plume moving through a tropospheric wind shear tilts at an angle in the vertical (e.g., Marwitz and Berry, [1971]). Ray trace simulations show that tilted plumes with zero wind above the tropopause create an anisotropic spectrum of GW which appear as arcs, not concentric rings [Vadas, unpublished]. As shown in Figure 4.9 (d) and (e), large eastward zonal and southward meridional wind shears exist in the upper troposphere on

both 04 May 2007 and 03 June 2008. This may partially account for the CGW appearing as arcs in the OH airglow layer on these nights (see Figure 4.2). On days when circular wave patterns are observed (e.g., 11 May 2004, 08 September 2005, and 26 August 2008 from Figures.4.1 and 4.2), the wind shear in the upper troposphere is relatively small (see Figures. 4.8(a), 4.9(c) and 4.9(f)).

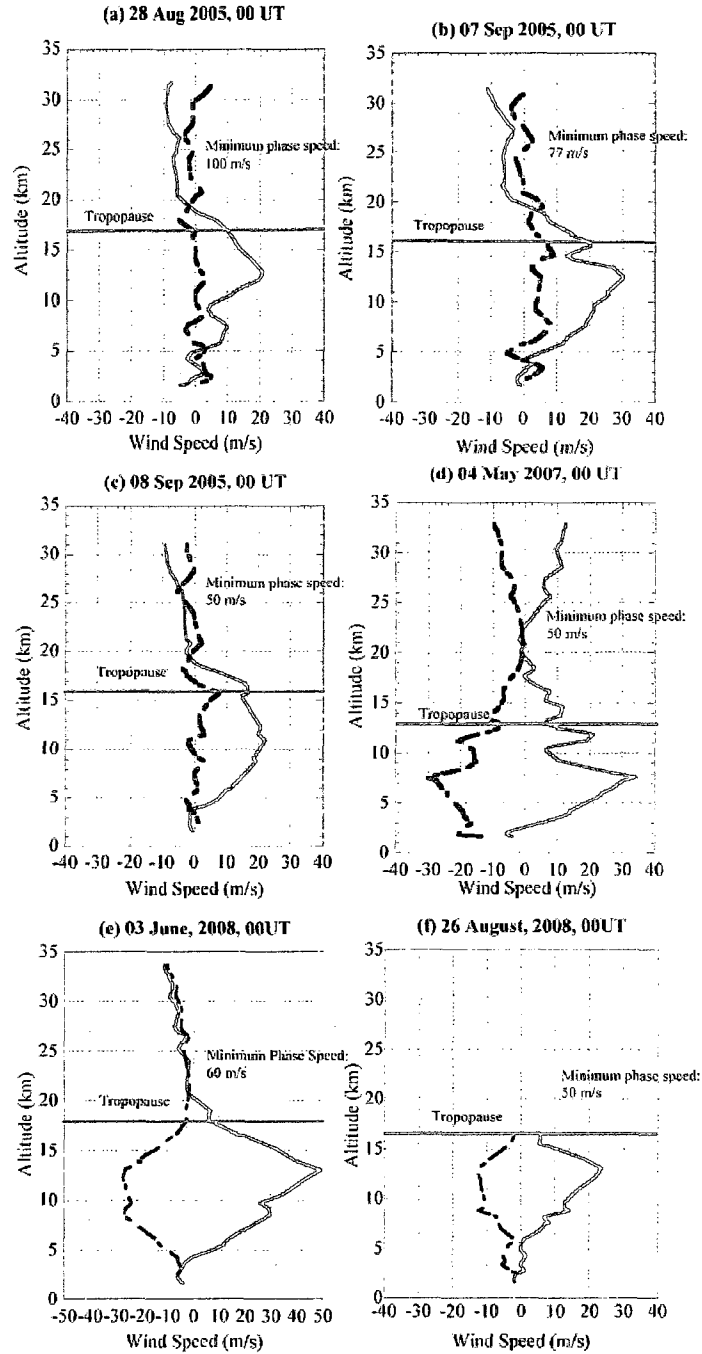


Figure 4.9. Radiosonde wind profiles as Figure 4.8(a) at 00 UT on the nights of CGW observations on (a) 28 August 2005 (b) 07 September 2005 (c) 08 September 2005 (d) 04 May 2007 (e) 03 June 2008 (f) 26 August 2008. Profiles at Denver/Stapleton Station (39.75°N, 104.87°W), the closest to YRFS, are unavailable for 30 August and 04 September 2008.

#### **4.1.5 Comparison between ray-tracing program and the observation**

Our collaborator, Dr. S. Vadas, used a convective plume model and a ray trace model to simulate the CGW on 11 May 2004. Using a zero wind profile and a April mean wind profile from the HAMMONIA general circulation model, the model results are comparable to the observation presented in Section 4.1.1. The modeled horizontal wavelength and period agree better to the observation, but not significantly improved from zero wind estimation in Figure 4.5. This shows that the model wind is close to zero in April. However, the actual wind between the tropopause and the OH layer may not be the same as the climatology wind. The measurement of wind between tropopause and the OH layer is in need for the model to perform better real time simulation. The modeled temperature perturbation  $T'$  is also compared to the temperature perturbation deduced from the measured airglow intensity perturbation  $I'$ . Figure 4.10 shows the comparisons of horizontal wavelength, period, temperature perturbation between observation and ray trace model. Interested readers could read [Vadas et al., 2009] for more details.

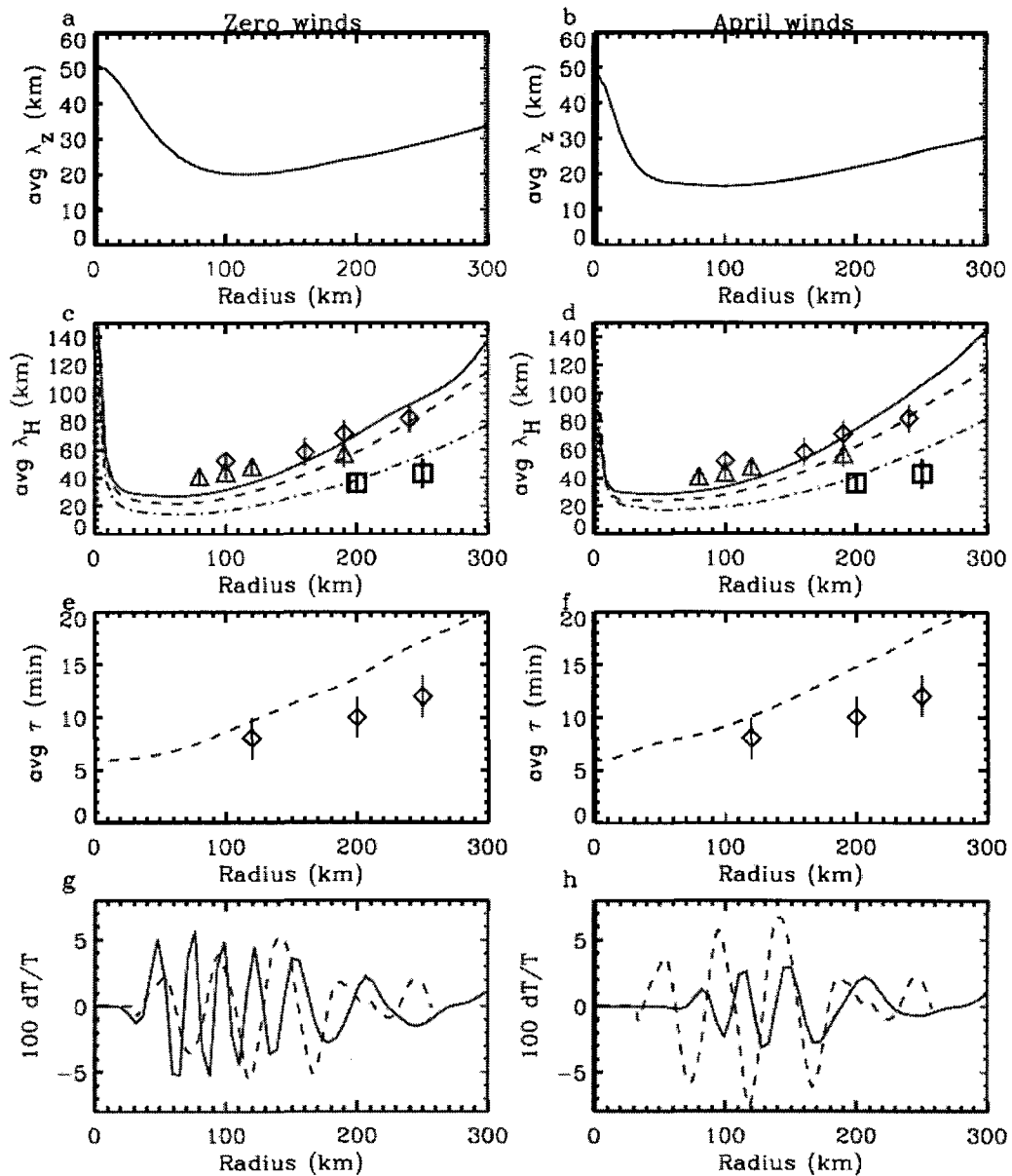


Figure 4.10 (left) Model results for zero winds. (right) Model results for the April zonal winds. (a, b) Model average vertical wavelengths at  $t = 55$  min. (c, d) Model average horizontal wavelengths at  $t = 45, 55,$  and  $85$  min as solid, dashed, and dash-dotted lines, respectively. Data at 0350, 0400, and 0430 UT are shown as diamonds, triangles, and squares, respectively [Yue et al., 2009]. (e, f) Model average ground based wave periods at  $t = 55$  min (dashed lines). Data at 0400 UT (diamonds). (g, h) Model temperature perturbations  $T_0/T$  (in %) at  $t = 55$  min along a line  $45^\circ$  to the northwest of the convective plume (solid lines). Inferred values of  $T_0/T$  (from the data shown in Figure 1b) at 0400 UT (dashed lines). [Vadas et al., 2009]

## 4.2 Mesospheric bores and large-scale gravity waves

### 4.2.1. Introduction to mesospheric bores

The mesospheric bore is a propagating sharp front followed by a wave-train (undular bores) or turbulence (turbulent bores) in the mesopause region. It has been previously observed by all-sky airglow imagers at various locations and in different seasons [Taylor et al., 1995; Medeiros et al., 2001; Smith et al., 2003, 2005; Brown et al., 2004; She et al., 2004; Fechine et al., 2005; Shiokawa et al., 2006] as a clear propagating front in the airglow intensity. Dewan and Picard [1998] first explained the mesospheric bore with the hydraulic jump theory. They suggested that a temperature inversion layer, a large wind shear layer or both in the mesopause region could form a duct for bore propagation. This theory was later verified by collocated temperature/wind lidar and airglow imager observations [Smith et al., 2003, 2005; She et al., 2004] and by the collocated airglow imager and meteor radar observation [Simkhada et al., 2009]. Dewan and Picard [2001] continued to suggest that the critical level interaction between a large gravity wave (GW) and the mean wind field could provide the necessary forcing to generate the mesospheric bores. This mechanism has not yet been confirmed by observations or numerical simulations.

Seyler [2005] first numerically simulated the mesospheric bore formation. A long-wavelength large-amplitude GW is initially confined in a thermal duct. Due to the nonlinear dynamics in a shallow channel, the wave crest travels faster than the lower portion of the GW. As a result, the front of the GW steepens with time and becomes vertical. Then the sharp front becomes the bore front and continues to generate trailing small undulations. Laughman et al. [2009] extended Seyler's work by considering

different ducting scenarios, including thermal ducts, Doppler ducts and the combination of both. Similar large-amplitude GW generating mesospheric bores resulted in each case.

In this section, we report the observation of the excitation of mesospheric bores by ducted large-scale GWs on 09 October 2007, by an all-sky OH imager located near Fort Collins (41°N, 105°W), Colorado. To our knowledge, this is the first observation of near-monochromatic GW steepening and generating mesospheric bores. The required ducting region is a temperature inversion layer in the mesopause region, which was detected by the collocated Colorado State University (CSU) temperature/wind sodium lidar prior to the passage of those GWs and subsequent bore formation.

#### **4.2.2. All-sky imager observations of bore formation from large-scale gravity waves**

The OH images from the night of 09 October 2007 show very active GW activity throughout the night. The imager acquisition started at 0144 UT. Before 0330 UT, small-scale GWs were dominant, propagating westward with ripples with horizontal wavelength less than 10 km at sporadic places. The ripples indicate local instabilities in these areas [Hecht, 2004]. The observation of the large-scale GW steepening and bore excitation was after 0330 UT, which will be discussed in detail in this section. After 7 UT, no clear large-scale GWs and sharp fronts could be identified. The sky was again dominated by small-scale GWs.

Figure 4.11 shows a sequence of normalized images at 10 min interval from 0330 to 0640 UT on 09 October 2007. Figure 4.12 shows the associated difference images. The times when the images were recorded are on the top of the images. The geographic map of Figures 4.11 and 4.12 covers the same 600km×600km area. The centers of the maps

are the YRFS. We determine the large-scale GWs in the normalized OH images by identifying their bright and dark wavefronts (or bands) with two criteria: they have to keep a relatively constant waveform within a long enough time (about one period of GW) and the phase velocities at the bright and dark wavefronts must be consistent. In Figures 4.11 and 4.12, we identify two large-scale GWs (named GW #3 and #4) propagating from the southeast to the northwest, which will be described in detail below. Table 4.1 is used to distinguish GW #1-4. Their wave fronts are denoted by yellow and red lines, respectively, and their propagation directions by the blue arrows in Figures 4.11 and 4.12.

Table 4.1 List of gravity waves discussed in Chapter 4.

	Date	Description	Section belongs
CGW #1	May 11, 2004	Concentric gravity wave	4.1
CGW #2	May 11, 2004	Concentric gravity wave	4.1
GW #3	Oct 09, 2007	Large-scale band wave	4.2
GW #4	Oct 09, 2007	Large-scale band wave	4.2

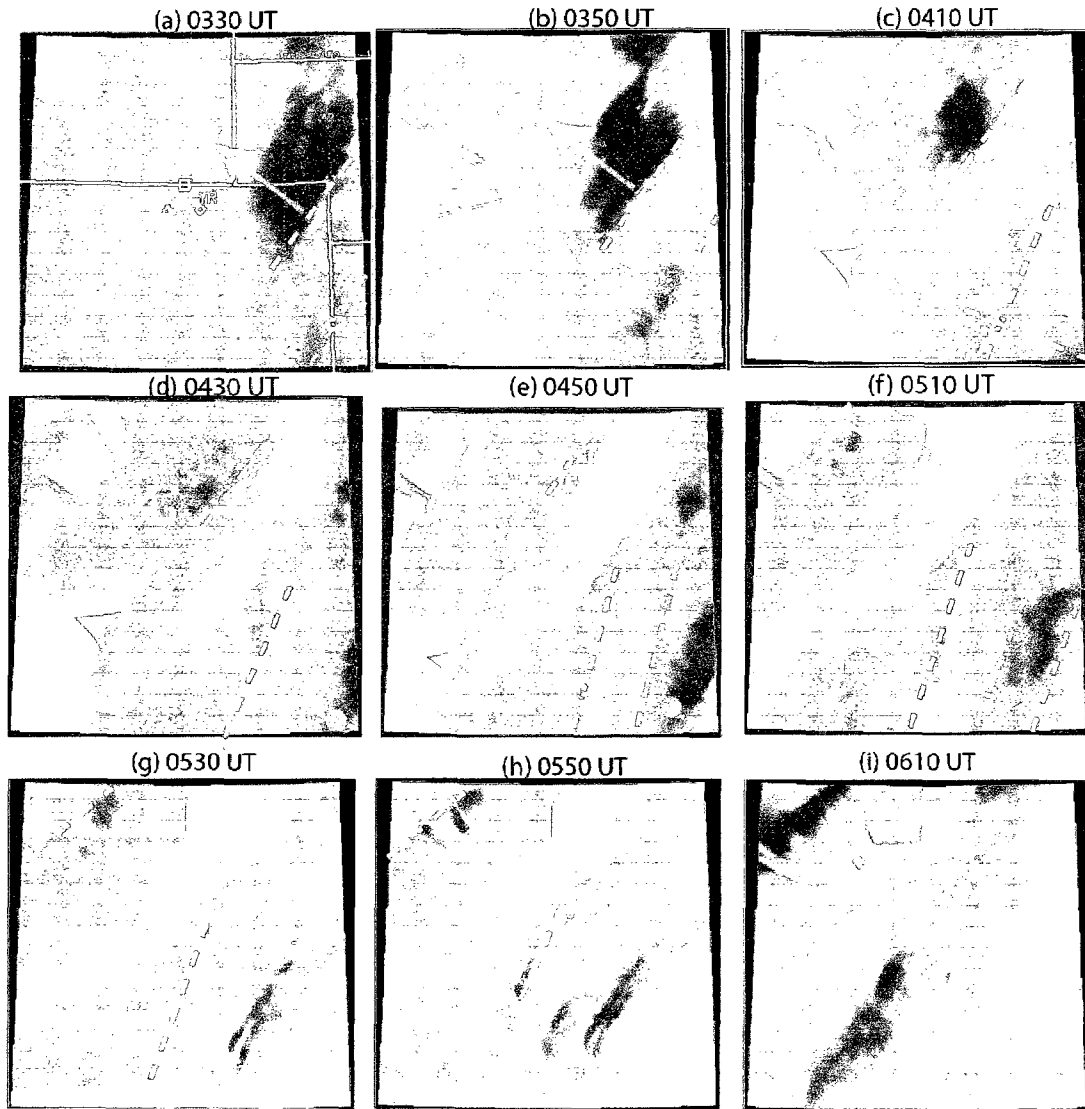


Figure 4.11. Flat-fielded OH images in a sequence of UT times (on the top of each image) on 09 Oct 2007. Each image is normalized by the background during the entire night before being projected onto a geographic coordinate with the size of 600km×600km. Maximum positive and negative values are shown as light and dark shading, respectively, in the scale of  $\pm 30\%$ . The yellow and red dashed lines mark the front of GW #3 and #4, respectively. The blue arrows show the propagation direction of the waves. The narrow bright feature extending from the lower left corner to the center of the images is the Milky Way.

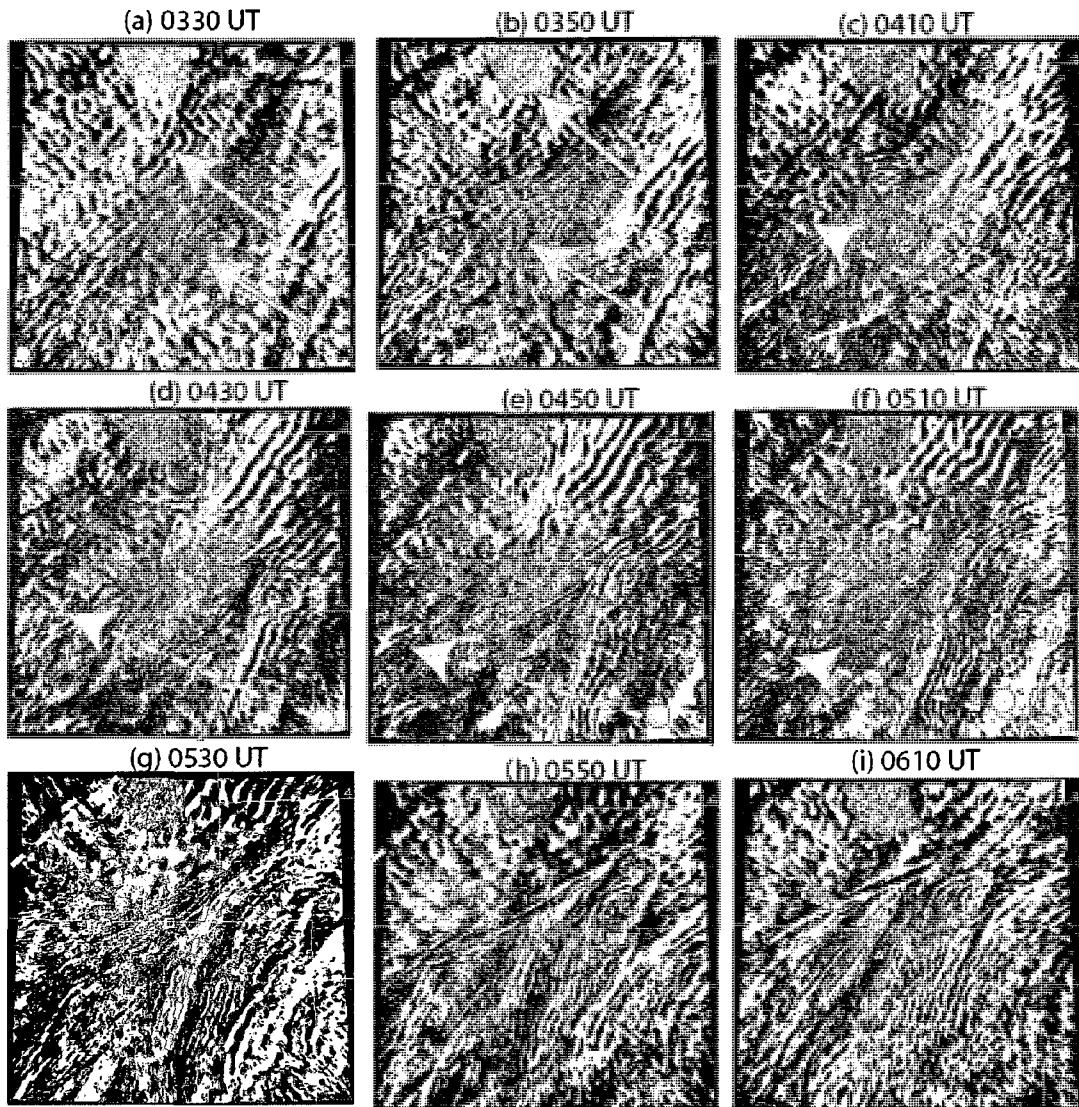


Figure 4.12. same as Figure 4.11, except each image is the difference between two consecutive raw images.

At 0330 UT, the bright wavefront of GW #3 extending northeastward (the yellow dashed line) is behind (on the right-hand side of) a dark band in Figure 4.11a. This bright wavefront leading a bore is seen to propagate progressively in the northwest direction (blue arrows) indicated by the right, the middle and the right yellow dashed lines, respectively in Figures 4.11d, 4.11c and 4.11d. By comparing the locations of these

bright wavefronts, we can deduce the horizontal phase speed of GW#3 as it moves towards the northwest. The left yellow line in Figure 4.11b is to denote the dark wavefront of GW #3, which is about a half wavelength ahead of the bright wavefront (the rightmost yellow line). Inside the dark band of GW #3 (between the two yellow lines in Figure 11c), there is a narrower and darker band. Since the shape of this darker band changes with time and its front is not parallel to GW #3, its origin is not clear; it possibly results from interference between GW#3 and other waves. This darker band merges into the background of GW#3 after 0410 UT as shown in Figure 4.11d. After this time, more than one horizontal wavelength of GW #3 with one bright band and one dark band is gradually distinguishable. Three wavefronts of GW #3 are highlighted by yellow lines in Figure 4.11e: from the left to right, the dark front and the bright front mentioned above followed by another dark front. This enables the direct measurement of the horizontal wavelength  $\lambda_h$  (the distance between two dark fronts) and the phase speed  $c$  of the GW#3 between 0330 and 0500 UT; they are, respectively,  $335 \pm 16$  km and  $52 \pm 3$  m/s, giving the apparent period of  $\tau = \lambda_h/c = 109 \pm 10$  min. The normalized oscillation amplitude of the OH airglow emission associated with GW #3 is determined to be 10 % of the average airglow intensity including a small amount of background. The dark and bright bands of GW #3 continue to move northwestward. The yellow lines are also added in Figure 4.11g and 4.11h to assist the reader in following the wavefronts. After 0500 UT (Figure 4.11f), the bright front is gradually blocked by the grey shade, which is a stationary irrelevant object near the all-sky imager, while the dark front is moving outside of the imager field of view (FOV) in the upper left corner.

The typical feature of mesospheric bores, high-frequency small-scale undulations, entered the imager FOV along with the bright front of GW #3. Therefore, the bores should already have been generated following the bright front before GW #3 entered the FOV. This shows that the mesospheric bore is generated before 0330 UT. The difference images in Figure 4.12 enhance these high-frequency and small-scale undulations, seen only vaguely in the normalized images in Figure 4.11. On the right-hand side of the yellow line in Figure 4.12a (the same yellow line in Figure 4.11a to denote the bright front of GW #3), we can see that there are two small crests (white lines) following the bright front at 0330 UT. The small crests propagated northwestward in the same direction as GW #3. The phase velocity of the small crests is also the same as GW #3,  $\sim 52$  m/s. In Figures 4.12b and 4.12c, at 0350 and 0410 UT, four and six small wave-crests can be identified following the same bore front (or wave front). Because these small crests are moving into the FOV, we cannot determine the rate of their generation. The horizontal wavelength of the high-frequency crests is 23-27 km. The period is 9-10 min, which is much shorter than GW #3. After 0500 UT, the mesospheric bore excited by GW #3 propagates northwestward gradually out of the imager FOV, along with GW #3. The self-steepening of the GW #3 and the bore excitation process are not observed because they occur earlier and outside of the FOV, like previous mesospheric bore observations in the literature. Fortunately, at a later time we observed the steepening of another long-wavelength gravity wave, GW #4 and associated bore generation and propagation. This will be discussed below.

The bright front of GW #4 enters the FOV from the southeast corner at 0330 UT, denoted by a red dashed line in Figure 4.11a. The red line in Figure 4.11b denotes the

same bright wavefront, which is to the northwest of the red line in Figure 4.11a. It is apparent that the front of GW #4 is also moving towards the northwest, similar to GW #3. The first dark wavefront following this bright wavefront travels into the FOV at  $\sim 0410$  UT, in Figure 4.11c; we denote this dark wavefront by another red line (the right one) in Figure 4.11f. A full horizontal wavelength of GW #4 can be identified in the images during 0440-0520 UT. In Figure 4.11f at 0510 UT, the three red lines (from the left to the right) indicate the bright and the dark front mentioned above, and another bright front that follows. GW #4 propagates to the northwest with a speed of  $36 \pm 4$  m/s. Its horizontal wavelength  $\lambda_h$  is  $193 \pm 3$  km. The period  $\tau$  is  $90 \pm 10$  min. The amplitude of the GW #4 as deduced from OH emission is  $\sim 10\%$  relative to the background airglow brightness. Even though GW #4 may still be in the FOV, it is not distinguishable after 0630 UT in the images. As it can be seen, the direction of GW #4 propagation is slightly rotated counterclockwise from  $30^\circ$  north of west at 0330 UT to  $20^\circ$  at 0510 UT and it remains at the same direction after 0510 UT.

After 0330 UT, GW #4 excites more high-frequency small crests or undulations phase-locked behind (on the right-hand side of) the bright front (denoted by the red line in Figure 4.11a and 4.12a). The number of the crests is increasing. The number of crests behind the bright wavefront of GW#4 increases from one at 0330 UT to more than seven at 0530 UT. Therefore, the rate of crest generation is more than three crests hour<sup>-1</sup>. It is comparable to the addition rates of the first bore observation (2.8 hour<sup>-1</sup>) in Taylor et al. [1995], half of those in Smith et al. [2003] ( $\sim 6$  hour<sup>-1</sup>) and two times those in She et al. [2004] ( $\sim 1.5$  hour<sup>-1</sup>). At 0430 UT, the horizontal wavelengths of these high-frequency crests decrease from 22 km near the bright front to 15 km in the back (from the left to the

right). The average horizontal wavelength of the trailing small-scale crests decreases from 20 km at 0430 UT to 12 km at 0530 UT. The phase front of the small crests also gradually changes from straight lines into curves. The dark front of GW #4 (the right red line in Figure 4.11e and 4.12f) also excites small crests after 0530 UT. The averaged horizontal wavelength of these small-scale crests is  $\sim 17$  km.

#### **4.2.3 GW #4 steepening and bore excitation**

After the general introduction of GW #4 using Figure 4.11 and 4.12 in the last two paragraphs, we can look at the details of this nonlinear phenomenon, because the steepening and bore-generation process of GW #4 occurs within the imager FOV. We plot the normalized OH emission intensity perturbation as a function of the propagating distance in Figure 4.13. The time sequence of Figure 4.13 is selected from 0410 UT to 0600 UT, the same as Figure 4.11c-4.11h. The zero point of the x-axis in Figure 4.13 is at the lower right corner of Figures 4.11 and 4.12. The direction of the x-axis is along the green dashed arrows in Figures 4.11c-f and 4.12c-f. The length of the green arrows in the geographic map is 500 km, the distance covered by the x-axis of Figure 4.13. Again, the measured average horizontal wavelength, phase speed and perturbation of GW #4 are, respectively, 193 km, 36 m/s and greater than 10% amplitude. A sinusoidal wave with these parameters is superimposed in Figure 4.13 (dashed line) to simulate the propagation of the unperturbed GW #4 prior to nonlinear interactions that lead to steepening.

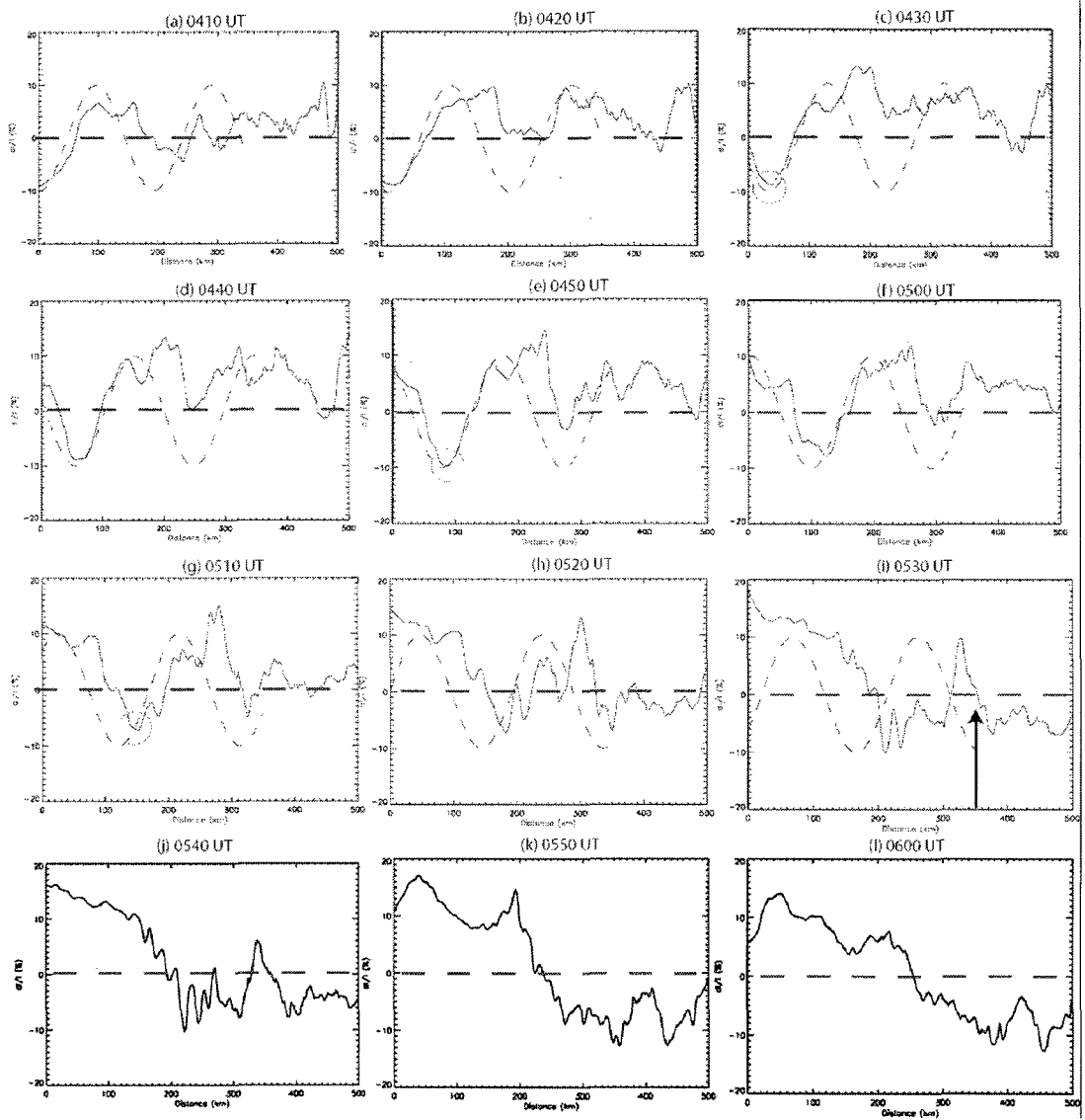


Figure 4.13 Sequence of the OH emission normalized perturbations along the propagating direction of GW #4. The X-axis is the geographic distance from the right lower corner of Figures 4.11 and 4.12 in the scale of 0-500 km. The scale of the y-axis is  $\pm 20\%$ . The dashed line is a sinusoidal wave with 193 km horizontal wavelength and 36 m/s velocity. The blue straight line indicates zero perturbation ( $y=0$ ).

Shown in Figure 4.13a, at 0410 UT, the part of GW #4 near the bright front (the crossing of the red dashed line by the green dashed arrow in Figure 4.12c) at  $x = 100$ - $200$  km apparently is not sinusoidal, while the wave (around the lower right edge in Figure 2c)

at  $x < 100$  km is reasonably sinusoidal. Comparing Figure 4.13a and 4.13b, the slope of the bright wavefront at  $x=150-200$  km clearly becomes sharper from 0410 to 0420 UT: it is nearly vertical at 0420 UT. We can see that the small crests trailing behind the bright front increases from two at 0430 UT (on the right side of the red line in Figure 4.12d and  $x \sim 200$  km in Figure 4.13b) to five at 0510 UT (between the two left-side red lines in Figure 4.12f and  $x=200-300$  km in Figure 4.13g).

In addition to this brightfront, the darkfront that follows in GW #4 is also observed to deviate from a sinusoid, and sharpened to a vertical line which then excites a bore, from 0430 (0-100 km in Figure 4.13c) to 0510 UT (100-200 km in Figure 4.13g). Red circles in Figure 4.13c, e and g highlight the trough of the dark band. The red dots are inserted in Figure 4.11 and 4.12 (g, i and k) to denote the same geographical locations as the circles in Figures 4.13c, e and g, respectively. In Figure 4.13c, at 0430 UT, the wave (solid line) around the red circle ( $0 < x < 100$  km) is quite sinusoidal, comparing well to the dashed line. In Figure 4.13e, at 0450 UT, the trough part leading the red circle ( $x > 100$  km) is quite sinusoidal, while the part trailing the valley ( $x < 100$  km) deviates from the sinusoid and is sharper than the dashed curve, and becomes nearly vertical at 0500 UT (Figure 4.13f). In Figure 4.13g, at 0510 UT, around the red circle, the trough is highly distorted from the sinusoid. At the same time, one small crest is excited trailing the red circle at  $x = 100$  km. The evolution of the darkfront from a nearly sinusoidal wave to a steepened front compares favorably to the numerically simulated bore generation process shown in Figure 4 of Seyler [2005] and Figures 3 and 4 in Laughman et al. [2009]. Both simulations invoke nonlinear interactions on the disturbances of the large-

scale GW that lead to steepening of wave fronts and undular bore formation within a ducting layer.

Surprisingly, the mesospheric bore excited at the bright front of GW #4 later develops into a single soliton-like perturbation from 0500 to 0530 UT at ~300 km in Figures 4.13g-4.13i. The amplitude of the soliton-like perturbation is greater than 15%. The reason that the undular bores evolve into a larger soliton-like perturbation remains unclear, nor has it been reported or discussed in the literature to our knowledge. It could be a scenario for further simulation study. Fortunately, around 0530 UT, this large perturbation in the OH imager passes the east lidar beam (its location is marked by the black arrow at  $x=350$  km in Figure 4.13i); its impact on the background atmosphere will be studied in Section 4.2.5. The large perturbation is damped after 0530 UT as shown in Figure 4.13j-4.13l.

#### **4.2.4 Temperature inversion layer and GW trapping**

The ducting layer is considered as a necessary but certainly not a sufficient condition to generate mesospheric bores and guide their propagation [Dewan and Picard, 1998; 2001]. The duct can be formed either by a temperature inversion layer or a wind shear layer as discussed in Section 3.3. The previous simultaneous observations with airglow imagers and fluorescence lidars have detected the coexistence of mesosphere bores and temperature inversion layers [Smith et al., 2003, 2005; She et al. 2004]. The numerical simulations by Seyler [2005] and Laughman et al. [2009] also invoke a ducting layer to confine the long-wavelength, large-amplitude GW in order to form internal bores.

On 09 October 2007, the CSU sodium lidar observed a temperature inversion layer at 2-7 UT near the OH airglow layer when the long-wavelength GWs and mesospheric bores were observed. Figure 4.14a gives the background temperature contour in the mesopause region (80-105 km). The temporal and vertical resolutions are 15 min and 2 km with the uncertainty of 3 K at around 90 km. The maximum measurement uncertainty is 5 K. The temperature in Figure 4.14a was measured by the east lidar beam. The west and north beams have less signal to noise ratio. There is a gap in the data at 6-7 UT for the temperature and wind measurement in the west and north beams. This gap is likely due to thin clouds in the lower atmosphere. As shown in Figure 4.14a, a temperature maximum descends from 92 km at 2 UT to 87 km at 6 UT. This temperature inversion layer vanishes after 7 UT. The squared Brunt-Vaisala frequency ( $N^2$ ) in Figure 4.14b is derived from the east-beam temperature. The Brunt-Vaisala frequency further demonstrates the existence of a downward propagating thermal duct at ~90 km before 7 UT. The white lines in Figure 5b denote the region where the value of  $N^2$  is zero. We can see that the large-valued  $N^2$  layer at ~90 km is well sandwiched by two layers of small  $N^2$ . The FWHM depth of the thermal duct layer is about 4 km at 2-4 UT and 3 km at 5-7 UT. Figure 4.14 shows that the temperature inversion layer at ~87 km ends around 6.5 UT. This agrees with the fact that no mesospheric bores were observed after 7 UT on 09 October 2007, suggesting the importance of a ducting layer to form and sustain the mesospheric bores.

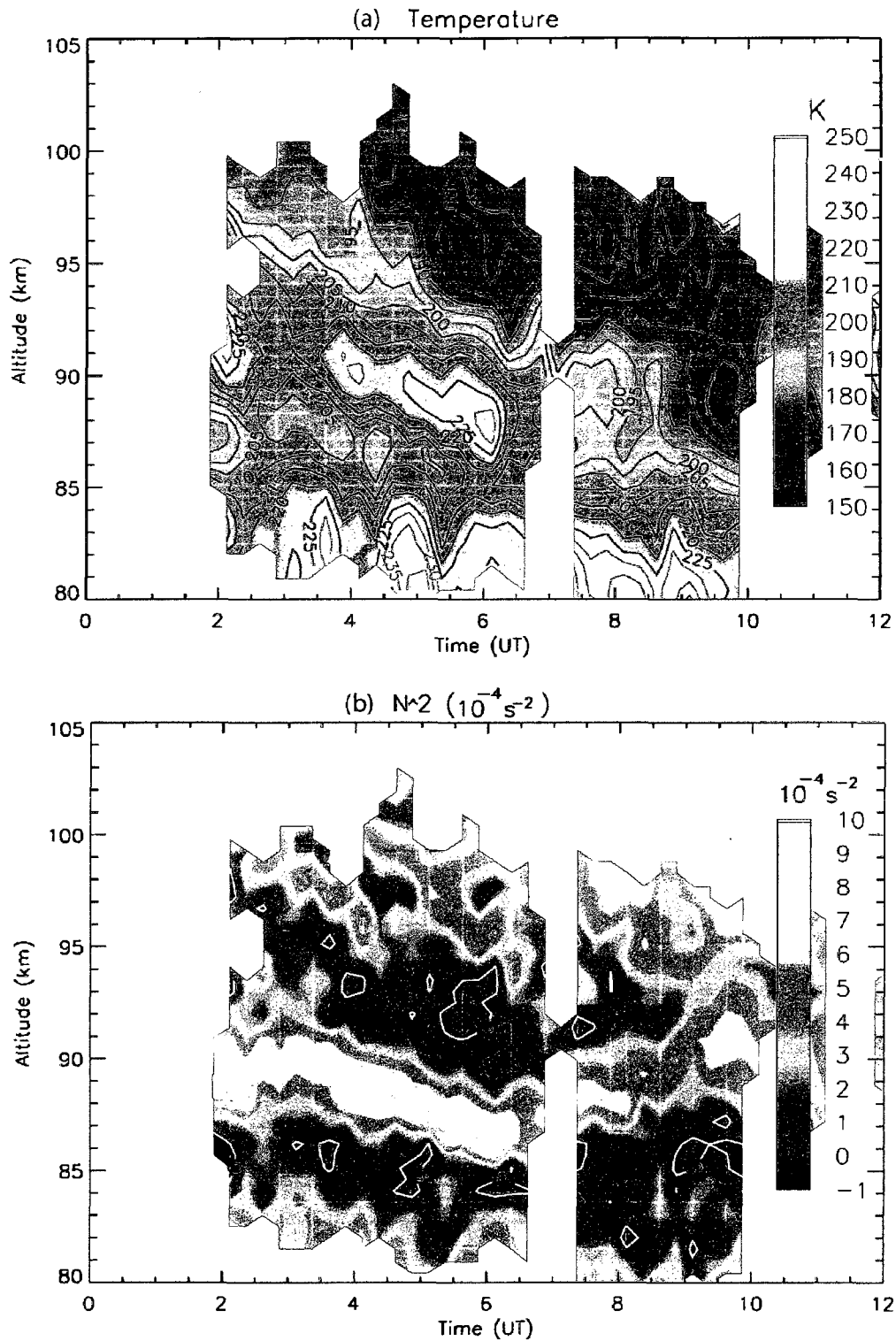


Figure 4.14. Sodium lidar measurement of the mesopause region on 09 Oct 2007. (a) Temperature in K (b) squared Brunt-Vaisala Frequency in  $10^{-4} \text{ s}^{-2}$ .

It is well-known that a wind shear in the mesopause may strengthen or weaken the thermal duct depending on the angle between the GW propagation direction and the mean wind direction [Dewan and Picard, 2001]. To include the horizontal wind into the duct, we calculate the vertical wavenumber  $m = 2\pi/\lambda_z$  using the dispersion relation (3.13), where  $c$  is the averaged phase velocity of the long-wavelength GWs ( $52 \text{ ms}^{-1}$  for GW #3 and  $36 \text{ ms}^{-1}$  for GW #4),  $u$  is the averaged horizontal wind in the GW propagation direction,  $k$  is the horizontal wavenumber ( $2\pi/335 \text{ km}^{-1}$  for GW #3 and  $2\pi/193 \text{ km}^{-1}$  for GW #4) and  $H$  is the scale height.  $H$  is a function of the temperature. Figure 4.15a shows the background wind velocity  $u$  to the northwest, along the direction of the long-wavelength GW propagation. Data with wind measurement errors greater than  $10 \text{ ms}^{-1}$  is discarded. The measurement uncertainty of horizontal wind at 90 km is  $\sim 5 \text{ ms}^{-1}$ . The wind between 2 and 6 UT at  $\sim 90 \text{ km}$  shows downward phase progression similar to the temperature contour. Using (3.13) and wave parameters of GW #4, Figure 4.15b gives  $m^2$  of GW #4. The white lines denote the region where  $m^2$  is zero. Once  $m^2$  is negative, GWs become evanescent and may be reflected. We see that in Figure 4.15b there is a solid reflective upper boundary with  $m^2 = 0$  for GW #4 at 2-6 UT. This boundary progresses downward from 97 km at 2 UT to 92 km at 6 UT. There is a less-reflective lower boundary with small but positive  $m^2$  at  $\sim 85 \text{ km}$ . It enables GW #4 to penetrate partially into the ducting region between 87 and 90 km from the lower atmosphere without being fully reflected. The coexistence of the upper and lower boundaries suggests partial trapping of GW #4 inside the layer. The similar  $m^2$  profile can be calculated for GW #3 using (3.13), its phase speed and  $k$  value (not shown). We find GW #3 is also trapped in a thermal duct similar to GW #4 shown in Figure 4.15(b).

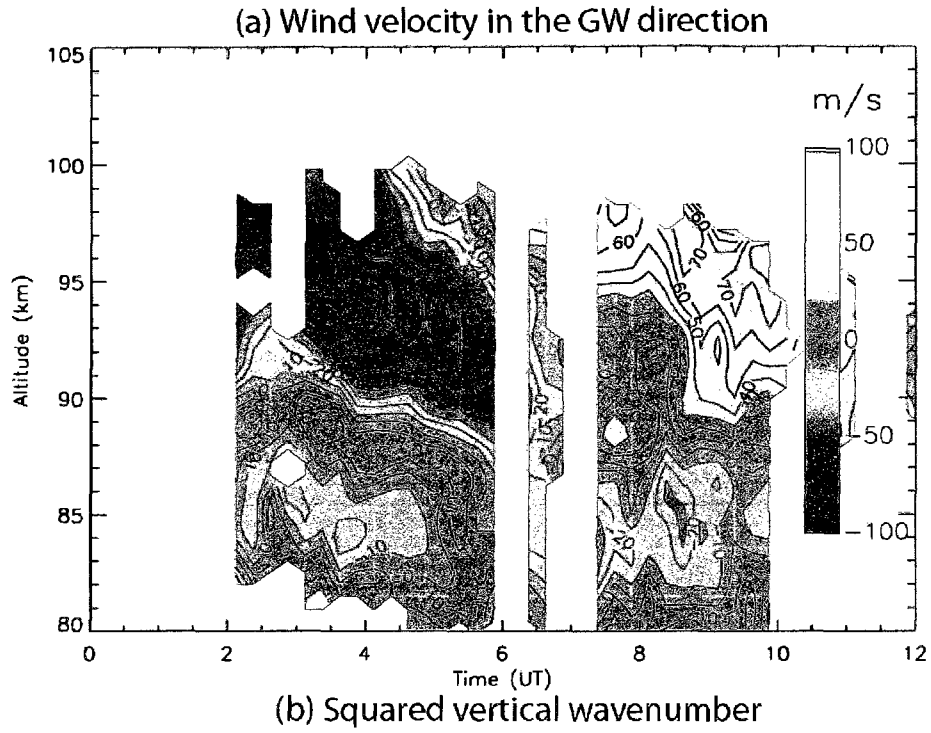


Figure 4.15. Sodium lidar measurements of the mesopause region on 09 Oct 2007. (a) Wind velocity ( $\text{ms}^{-1}$ ) in the GW #4 direction (b) squared vertical wavenumber for GW #4 in  $\text{km}^{-2}$ .

When GW #3 and #4 are trapped in the thermal duct, the lidar-measured temperature consists of oscillations induced by these large-amplitude gravity waves, along with longer-period inertia gravity waves, tidal waves and the mean state. We separate the internal GW effect from the mean temperature, long-period tidal waves and inertia GWs. Figure 4.16a is the reconstructed mean state plus inertia GWs and tidal wave temperature following the least-square fitting algorithm in *She* [2004]. 24 hours are included in the tidal fit. The reconstructed contour without any internal GW effects (Figure 4.16a) shows that the temperature inversion layer  $\sim 90$  km is strongly related to the inertia gravity waves and tidal waves. The importance of tidal waves on the generation of inversion layers has been discussed in Meriwether and Gardner [2000]. Figure 4.16b shows the residue temperature after the mean state and tidal waves were removed. Confined in the thermal duct around 90 km before 7 UT, there are two groups of temperature oscillations. The solid ellipse in Figure 4.16b encloses the temperature oscillation of  $\sim 140$  min period at 2-5 UT with a downward phase progression. The amplitude of the temperature perturbation is 10 K. In the dashed ellipse, there is a temperature oscillation of 90 min period at  $\sim 87$  km between 5-7 UT without apparent downward phase progression. Recall that in Figure 4.11, the front of GW #3 travels through the CSU lidar before  $\sim 0530$  UT and the front of GW #4 passes the beams after  $\sim 0530$  UT. The imager-measured periods of GW #3 and #4 are  $109 \pm 10$  min and  $90 \pm 10$  min, respectively. The period and the observation times of the temperature oscillations measured by lidar compare favorably with the imager observed large-amplitude GWs at the same altitude, suggesting that these lidar observed temperature oscillations inside the duct are caused by the trapped GW #3 and #4.

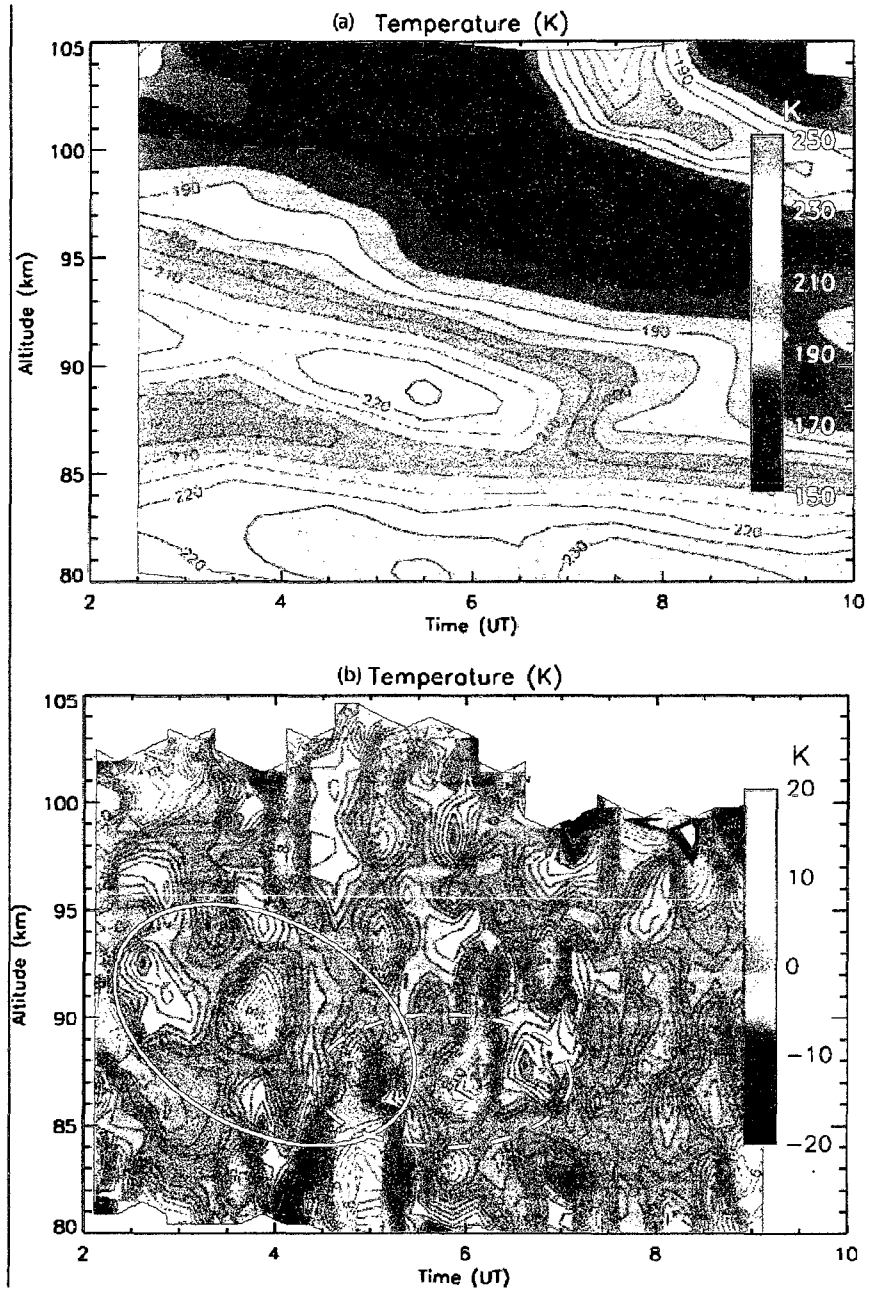


Figure 4.16. (a) Mean state and tidal component reconstructed temperature contour, (b) residue temperature after Mean state and tidal component being removed.

#### 4.2.5 Vertical motions induced by the mesospheric bores

So far, we have discussed how the duct can facilitate the formation of mesospheric bores from large GWs; in turn, the perturbations which arise from the bore formation may disturb the mean state. As mentioned earlier at the end of Section 4.2.3, mesospheric bores from GW #4 developed into a large-amplitude soliton-like perturbation and passed the east-pointing lidar beam at 0530 UT. Here we will discuss the background potential temperature and sodium densities in response to this soliton-like feature.

The potential temperature  $\Theta$  is a better measure of the motion of an air parcel than the temperature  $T$ . It may be derived from the temperature by assuming hydrostatic balance and the ideal gas law [Franke and Collins, 2003]:

$$\Theta(z, t) = T(z, t) \exp\left(\frac{R}{c_p} \int_{z_0}^z \frac{g dz'}{RT(z', t)}\right) \quad (4.4)$$

where  $T(z, t)$  is the temperature,  $z_0$  is the reference altitude (81 km in our calculation),  $g = 9.5 \text{ ms}^{-2}$ ,  $R = 287 \text{ JK}^{-1}\text{kg}^{-1}$  and  $c_p = 1004 \text{ JK}^{-1}\text{kg}^{-1}$  are the gravitational acceleration at the middle atmosphere, gas constant and specific heat at constant pressure, respectively. Figure 4.17 gives the calculated potential temperature contour for 09 Oct 2007. It shows a nearly vertical lines of constant potential temperature between 88 and 94 km around 6 UT suggesting convective instability, and those extending from 89 km to 94 km near 0530 UT are in fact super-adiabatic [Williams et al., 2002; Franke and Collins, 2003; Smith et al., 2005; Xu et al., 2006]. Since this time frame is coincident with the passage of the soliton-like large perturbation in GW #4 (see Figure 4.13i) in the OH emission, the observed instability is likely the result of this huge perturbation.

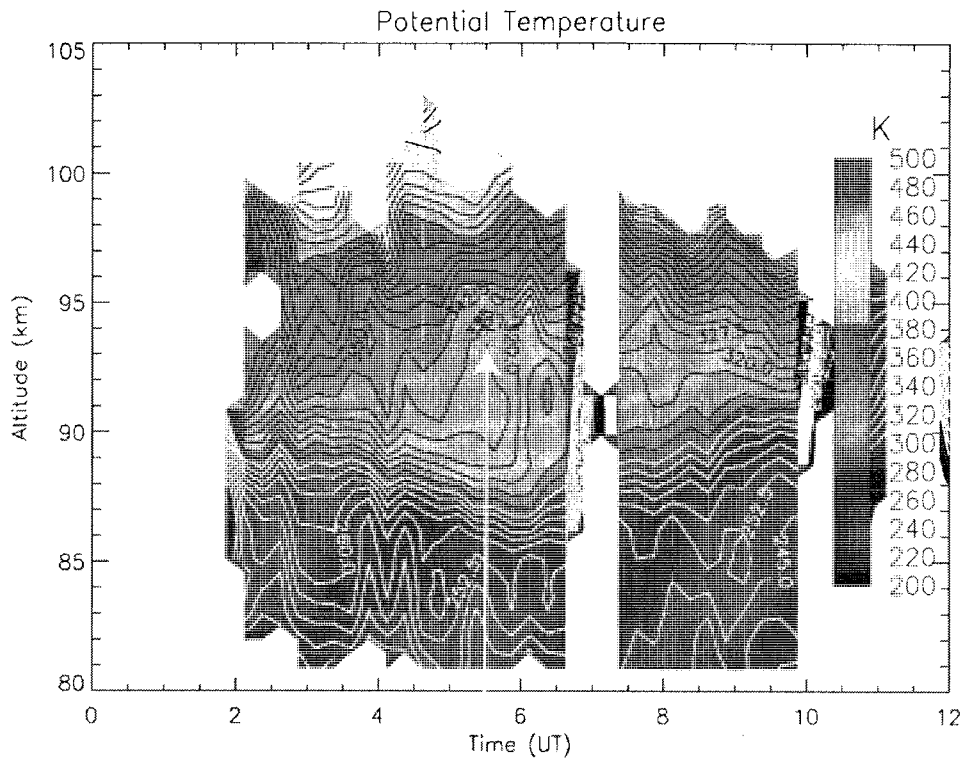


Figure 4.17. Potential temperature on Oct 09 2007 measured by the east beam. The white arrow indicates the time when the bright front of GW #4 with a large perturbation passed the beam.

To further confirm that the vertical motion at 0530-0600 UT is related to the passage of GW #4, we look at the sodium density changes in three lidar beams. Although the temperature and wind data in the north and west beams is unavailable around 0600 UT, the sodium density profiles in three beams are available throughout the night since the determination of sodium density requires lower lidar signal level. Assuming that the chemical reactions involving sodium atoms are not important in our case, the sodium density can be regarded as a passive tracer of the GW perturbation. Figure 4.18 shows the sodium density contours with 5 minute interval. The panels from the top to the bottom are measured by the east, north and west beam, respectively. Because GW #4 is propagating northwestward, the front should pass through the east beam in the mesopause before the

north and west beams. As shown in Figure 4.11, the bright front of GW #4 passes by the east beam around 0530 UT, and by the north and west ones around 0600 UT. When GW #4 passes through the CSU lidar at around 0530-0600 UT, the sodium atom densities dramatically increased in all three channels at 87-92 km. The sodium density reaches the peak at around 0520 UT in the east beam, 0545 UT in the north beam and 0630 UT in the west beam. One unique capability of a multi-beam lidar measurement is that it shows delays in the GW perturbed lidar signal when the GWs travel through the beams. From Figure 4.11, we can see that GW #4 took 30 min to travel from the east beam to the west/north beams. We can see that the sodium density enhancement at  $\sim 90$  km in the east beam (Figure 4.18a) occurs around 25 minutes and 70 min prior to the similar enhancements in the north and the west beams, respectively (Figure 4.18b and 4.18c). The time delay between the east and north beams is consistent with the imager observation. The passage of GW #4 and its mesospheric bores in relatively short time duration of  $\sim 25$  min appears to be correlated with the sodium atom density enhancement. However, over longer time durations, other factors may alter the Na density distributions. While the wave front in the imager arrives at the west and north beam locations about the same time, their time delay in the Na density maxima is  $\sim 45$  min.

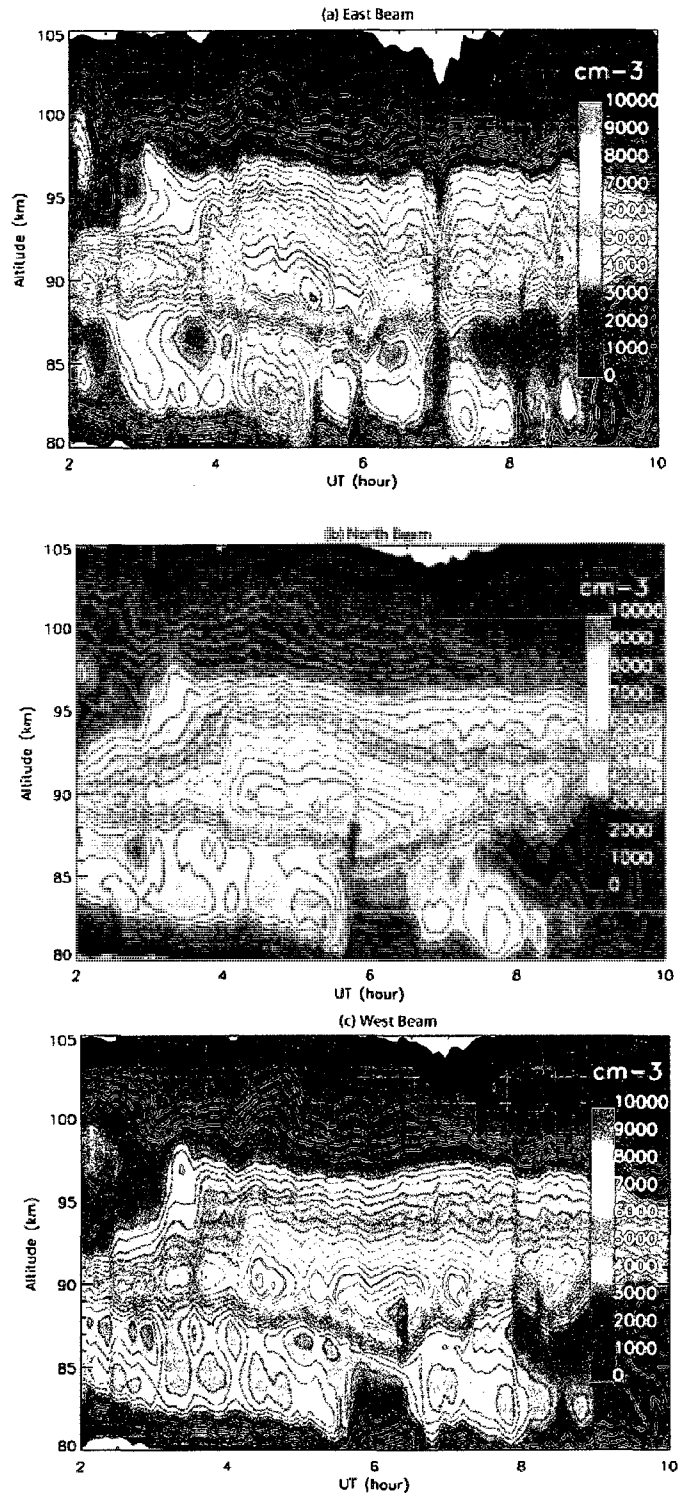


Figure 4.18. Sodium density (in a unit of  $\text{cm}^{-3}$ ) contours measured by CSU sodium lidar on 09 Oct 2007 by the east (a), north (b) and west (c) beams. The temporal spatial resolution is 5 min.

#### 4.2.6 Lower atmosphere origin of large-scale gravity waves

We have shown bore generation from long-wavelength GWs consistent with nonlinear simulations of Seyler [2005] and Laughman et al. [2009]. An equally important question is “what mechanism generates these GWs?” There are several candidate sources in the lower atmosphere that could generate GW #3 and #4 with  $\sim 200$  km horizontal wavelengths and 1.5-2 hour periods: topography, convection, shear instability, and geostrophic adjustment related to jets and fronts [Hooke, 1986; Fritts and Alexander, 2003; Zhang, 2004]. Smith et al. [2003] and Brown et al. [2004] already related the troposphere frontal systems to the mesospheric bores. Figure 4.19a shows the weather map several hours before the observations of large-scale GWs #3 and #4. Here, a cold front was aligned from southwest to northeast with an extent from Texas to the Great Lakes at 22 UT on 08 Oct 08 2007. The white lines and arrow are added above Fort Collins in Figure 4.19a to show the phase of the long GWs and their propagating direction. This large cold front was aligned with the wavefronts of GW #3 and #4. By implication, the large-scale GWs could have been generated hours ago by this cold front. We find this coincidence of mesospheric bores and cold fronts with southwest to northeast phase alignment in every case of mesospheric bore observations over Fort Collins. Figures 4.19b-19d show the weather map with the similar cold fronts extending northeastward from the Texas to the Great Lakes on the nights of 07 Oct 2002 [She et al., 2004], 29 Oct 2003 and 19 Oct 2006, when the mesospheric bores were detected by the OH imager hours after. The difference images of the corresponding bores are inserted in Figure 4.19b-4.19d over Colorado. Although the scale of the airglow images is not the same as the weather maps, we can see that all of these mesospheric bores are more or less

aligned with the cold fronts and are propagating away from the fronts. While the detailed link between the cold fronts and trapped long-wavelength GWs requires further investigation, the perturbations produced by the passage of cold fronts in the troposphere should result in long-wavelength GWs with extensive wave fronts parallel to the cold front; these GWs then propagate up and are trapped by waveguides in the mesopause region. Climatologically, most of the mesospheric bores observed above Fort Collins are in October and November, when temperature inversion layers often observed over Fort Collins by the sodium lidar.

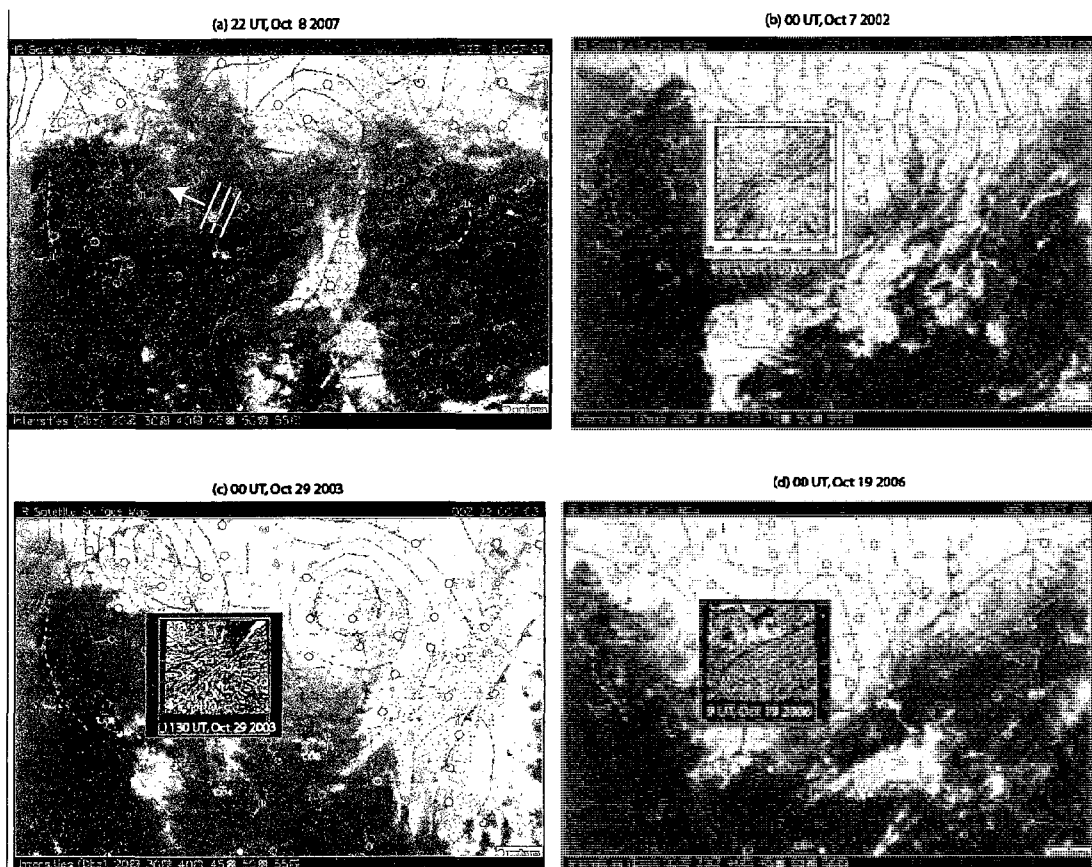


Figure 4.19. Weather maps at (a) 22 UT, 8 October 2007 (b) 00 UT, 7 October 2002 (c) 00 UT, 29 October 2003 (d) 00 UT, 19 October 2006.

### 4.3 Large wind shears and convective stability

The large winds and wind shears in the mesosphere and lower thermosphere (MLT) region not only play the essential role in the dynamics by causing Kelvin-Helmholtz (KH) instability, they also determine the critical levels for gravity wave propagation. The large wind and enhanced wind shear drive electrodynamics/plasma in the ionosphere. For example, the Lorentz force associated with the oppositely pointing zonal wind in a strong wind shear has been thought of as dominating mechanism for the formation of sporadic E layer in the MLT [Whitehead, 1970; Mathews, 1998; Collins et al., 2002] and the associated quasiperiodic (QP) radar echos [Larsen, 2000]. Furthermore, the large winds and wind shears also drive the equatorial electrojet [Hysell et al., 2002]. Enhanced winds and strong wind shears have been observed at 100-110 km over a wide range of latitudes, longitudes, seasons and local times by rocket sounding via chemical release experiments for the past five decades [Larsen, 2002]. The large wind shears can often exceed  $70 \text{ ms}^{-1}\text{km}^{-1}$  and sometimes reach  $100 \text{ ms}^{-1}\text{km}^{-1}$ . These large winds and wind shears can also be verified by other experiments. For example, the VHF radar is able to measure wind velocity between 93 and 110 km by tracking non-specular meteor echoes; large winds and large wind shears above 95 km have been reported [Oppenheim et al., 2009]. Even though the enhanced wind at 100-110 km can be reproduced by the thermosphere-ionosphere-mesosphere-electrodynamics general circulation model (TIME-GCM) with finer resolution [Larsen and Fesen, 2009], the strong wind shear is still unachievable in model studies. Indeed, the large wind and wind shear is significantly underestimated by the Horizontal Wind Model (HWM). The mechanisms to drive and

maintain the enhanced wind and extremely large wind shear in the MLT still remain open questions.

The narrow-band Doppler sodium lidar is capable of measuring the time evolution of temperature and horizontal winds simultaneously with high enough temporal and height resolution. This facilitates the investigation of the involved dynamics when large wind shears are present. For example, large wind shear ( $100 \text{ ms}^{-1}\text{km}^{-1}$ ) and temperature gradient ( $100 \text{ K km}^{-1}$ ) were observed simultaneously by the sodium lidar at high latitude between  $\sim 85$  and  $95 \text{ km}$  [Fritts et al., 2004]. Seven years of wind profiles by the Doppler sodium lidars in New Mexico ( $35.0^\circ\text{N}$ ,  $106.5^\circ\text{W}$ ) and Hawaii ( $20.7^\circ\text{N}$ ,  $156.3^\circ\text{W}$ ) have been compared to the results of chemical release experiments. The agreement is good below  $105 \text{ km}$  [Larsen and Fesen, 2009]. Because the sodium density decreases dramatically above  $100 \text{ km}$ , the Na lidar can seldom measure horizontal winds above  $\sim 105 \text{ km}$ .

Between 2002 and 2005, over 1600 hours of nocturnal mesopause region temperature, zonal and meridional wind data were collected. Because the analysis of stabilities and large wind shears requires high temporal and height resolutions [Zhao et al., 2003; Sherman and She, 2006], we only use the nocturnal lidar data for the characterization of stabilities and wind shears. Though the daytime data is available, it has lower signal to noise ratio. In this study, the 24-hour continuous lidar measurement in 1-hour interval will be utilized to determine the tidal wave and the background state.

#### 4.3.1. Lidar data analysis

To study the large wind and wind shear, the 2-minute photon count profiles are first averaged over every 15 minutes and vertically smoothed using a Hanning window of 2 km full-width half-maximum (FWHM) over-sampled at 0.5 km interval. It is recognized that GWs, tidal waves and planetary waves are superposed on the mean state, from which the local atmospheric stability is determined. The 2 km vertical resolution and 15 min temporal resolution of the lidar measurement can only cover a portion of the GW spectrum with periods longer than 30 min; this temporal resolution is short enough for the determination of tidal waves and planetary waves. The restriction by the measurement errors mainly due to photon noise prevents the further increase of resolution. To determine the tidal components during the nights with large wind shears, we also use hourly mean profiles on both day and night in 2002-2005, as in Yuan et al. [2008a, b].

The averaged measurement uncertainties due to photon noise for the nocturnal temperature and horizontal wind between 85 and 100 km are 2 K and  $3.5 \text{ ms}^{-1}$  for 15 min and 2 km resolution. Outside this altitude range, the measurement uncertainty increases dramatically due to decreasing sodium atom density. In this paper, we set the maximum allowed uncertainty of 5 K and  $10 \text{ ms}^{-1}$  for the observed temperature and horizontal wind following Sherman and She [2006]. The data with errors higher than this threshold is discarded. The gradient of temperature and horizontal wind is calculated with a vertical interval of 2 km. At the altitude of 85-100 km, the averaged measurement errors for the temperature gradient and wind shear are  $3 \text{ K km}^{-1}$  and  $5 \text{ ms}^{-1}\text{km}^{-1}$ . For the 1-hour and 2-km resolution data, the average measurement error for the temperature and horizontal wind is 1 K and  $1.5 \text{ ms}^{-1}$ , respectively.

With simultaneous temperature  $T$ , zonal wind  $U$  and meridional wind  $V$  measured by the CSU sodium lidar, we can deduce the quantities representing the local stability with specified temporal and height resolution, i.e., Brunt-Vaisala frequency and Richardson number. When the atmospheric lapse rate  $\Gamma = -dT/dz$  is greater than the adiabatic lapse rate  $\Gamma_d$ , i.e.,  $N^2$  is negative, the atmosphere is convective unstable. The larger the  $N^2$ , the more convective stable and stratified the atmosphere is. Based on the measurement uncertainties of temperature and its gradients, the typical error of  $N^2$  for 15 min resolution is  $0.00015 \text{ s}^{-2}$ . Large wind shear  $S = \sqrt{(du/dz)^2 + (dv/dz)^2}$  can overcome the stability of a stratified atmosphere, and induce dynamic instability. When  $Ri$  is small (typically less than 1/4), dynamic instability occurs and Kelvin-Helmholtz (KH) billows are formed.

It is worth mentioning that the Richardson number criterion is a necessary but not sufficient condition for dynamic instability [Dutton, 1986]. This Richardson number criterion may not rigorously apply in a number of scenarios, i.e., for slantwise (the wind shear is tilted from zenith) instabilities [Hines, 1971; Sonmor and Klaassen, 1997 and references therein], or when the molecular viscosity is important [Liu, 2007]. Moreover, this dynamic stability threshold is derived from the linear theory; the criterion may not apply to nonlinear flows.

#### **4.3.2. Observation of large wind shears**

While the typical tracing time for the chemical release experiments is ten minutes or less [Larsen et al., 2003], Na Doppler lidars can change the time resolution by averaging the profiles over a specified period. Along with simultaneous temperature

measurement, this allows us to investigate the stability associated with the large wind shears. Figure 4.20 shows the superposition of all of the wind shear profiles in 2002-2005 observed by the CSU Na lidar with the same vertical resolution (2 km) but different time resolutions (15 min vs. 1 hour). Profiles in Figure 4.20(a) are calculated from all the nocturnal lidar data in 15 min interval, which is more comparable to the time interval for a whole trace of rocket sounding winds. As shown, the Na lidar often observes large wind shears of greater than  $40 \text{ ms}^{-1}\text{km}^{-1}$  above 85 km. The shear magnitude increases with altitude and reaches the peak value at  $\sim 100 \text{ km}$ . This is consistent with the trend of the wind shear in the rocket sounding data in Figure 4.21 [Larsen, 2002]. However, the amplitude of the Na lidar measured shear is much less than the chemical release experiment results. This is partly because a 2-km FWHM Hanning window is employed to smooth out the lidar data vertically and to improve the signal to noise ratio. By changing to a 1-km resolution, the maximum shear by the Na lidar increases by  $\sim 20 \text{ ms}^{-1}\text{km}^{-1}$  (not shown). For the chemical release profiles, none of the measurement uncertainty is explicit and the vertical resolution is arbitrary. Those extremely large wind shears of  $\sim 100 \text{ ms}^{-1}\text{km}^{-1}$  might have been calculated in smaller spacing with larger uncertainty, compared to the lidar data. Given a quoted uncertainty of  $5\text{-}10 \text{ ms}^{-1}$  and 1 km interval [Larsen, 2002; Larsen et al., 2003], the typical rocket sounding measurement error for the wind shear is  $8\text{-}15 \text{ ms}^{-1}\text{km}^{-1}$ .

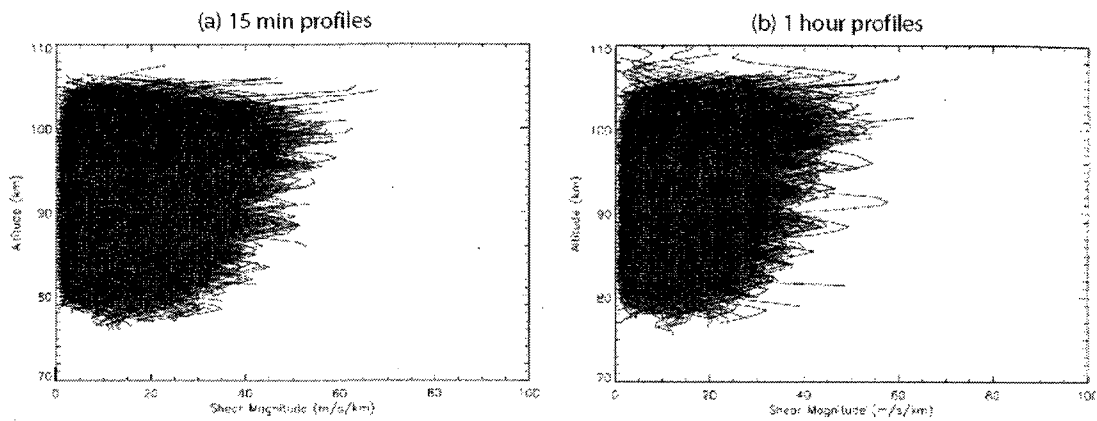


Figure 4.20. Superposition of the total wind shear magnitude profiles in 2002-2005 with (a) 15 min average time (b) 1 hour average time.

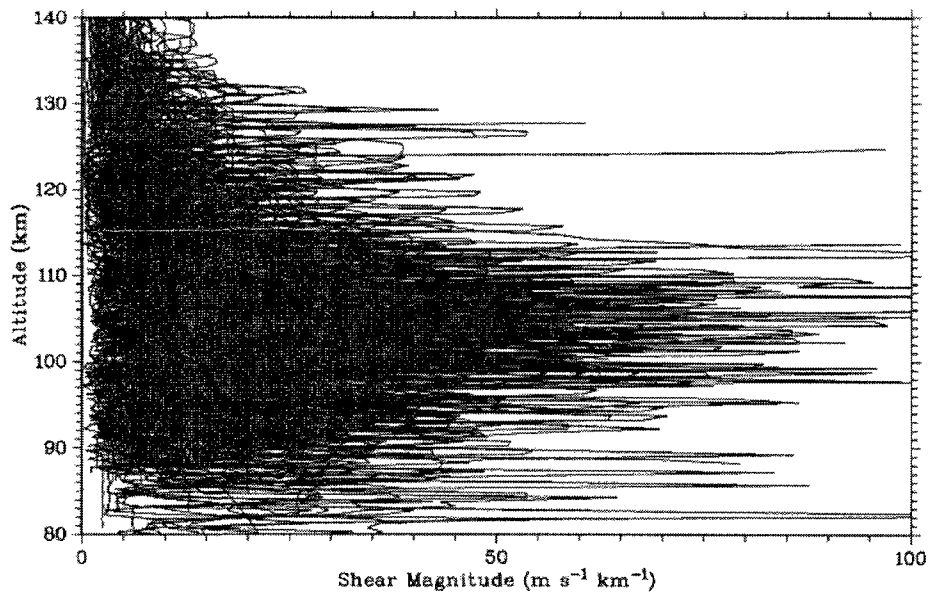


Figure 4.21 Superposition of wind shears measured by rocket chemical release experiments for four decades [Larsen, 2002].

Figure 4.20(b) shows the superposition of shear profiles averaged in 1 hour with the same height resolution of 2 km. By comparing the results to those with different time resolution of 15 min, we see no significant ( $<10$  m/s/km) difference in the shear amplitude or its altitude dependence, especially at higher altitude. Therefore, the

contribution of internal GWs with periods between 30 min and 2 hour to the large wind shear appears to be small, compared to the dynamics with period greater than 2 hours. Larsen and Fesen [2009] state that: because the enhanced horizontal wind at 100-110 km can be reproduced using the TIME-GCM model and the small-scale waves are not resolved in this model, the enhanced wind is not likely due to small-scale effects, like internal gravity waves. If we assume both the enhanced horizontal wind and strong wind shear at 100-110 km are generated by the same mechanism, then small-scale and high-frequency internal GWs do not significantly attribute to the enhanced wind and large wind shear at the lower thermosphere. It must be related to some large-scale dynamics either origins in the MLT or propagating upward from lower atmosphere. For example, sources could be tidal waves or planetary waves [Larsen and Fesen, 2009]. Next, we will illustrate the possible relation between large wind shear and tidal waves with a case study.

#### **4.3.3 Large wind shears and tidal waves**

We employ two data sets here for analysis. One is the nocturnal lidar data with 15 min and 2 km resolutions in 2002-2005. Another data set of full diurnal cycle observations, i.e., with >24 h continuous data in 2-km/1-hour resolution is used to retrieve the tidal-period (24h, 12h, 8h, 6h) perturbations. The result of a case study based on data taken in the night of May 14 2003 is presented in Figure 4.22, showing zonal wind, meridional wind, and wind shear, respectively in top, middle and bottom rows. The left column is the measured high-resolution nocturnal lidar data; the right column is the nighttime reconstruction of the mean-state and tidal-period perturbations deduced from the hourly mean full-diurnal cycle observations. In this example, judging from the

correlations between left and right columns, the observed large wind shear may be attributed mostly to the semidiurnal tidal perturbation. Shown in Figure 4.22(c) (left column), there is a downward propagating band of large wind shear ( $\sim 40\text{-}50 \text{ ms}^{-1}\text{km}^{-1}$ ) lasting almost all night. The wind shear deduced from the reconstructed mean state and tidal perturbations (Figure 4.22(c), right column) of  $\sim 40 \text{ ms}^{-1}\text{km}^{-1}$  reproduce the shape of the wind shear in the raw data. The meridional wind contour (Figure 4.22(b), right column) shows an unusually large vertical gradient of semidiurnal tide throughout the night at 85-95 km. The vertical wavelength of the semidiurnal tide in the meridional wind is about 11 km, which is much smaller than the typical vertical wavelength of 45-100 km for monthly mean climatology semidiurnal tides observed by the Na lidar [Yuan *et al.*, 2008b]. While at this night, the tidal amplitudes in the meridional wind at 90 km are 20 m/s, 45 m/s, 10 m/s and 5 m/s for the periods of 24h, 12h, 8h and 6h. The rapid wind transition within an extremely short-vertical-wavelength semidiurnal tide with the amplitude of  $30 \text{ ms}^{-1}$  significantly contributes to this night-long large wind shear. Comparing the raw wind shear and tidal wave wind shear in Figure 4.22(c), the effect of tidal wave on the large wind shear is obvious. Previous lidar studies have also shown the large wind shears follow the downward tidal phase in the mesopause region [Zhao *et al.*, 2003; Li *et al.*, 2005].

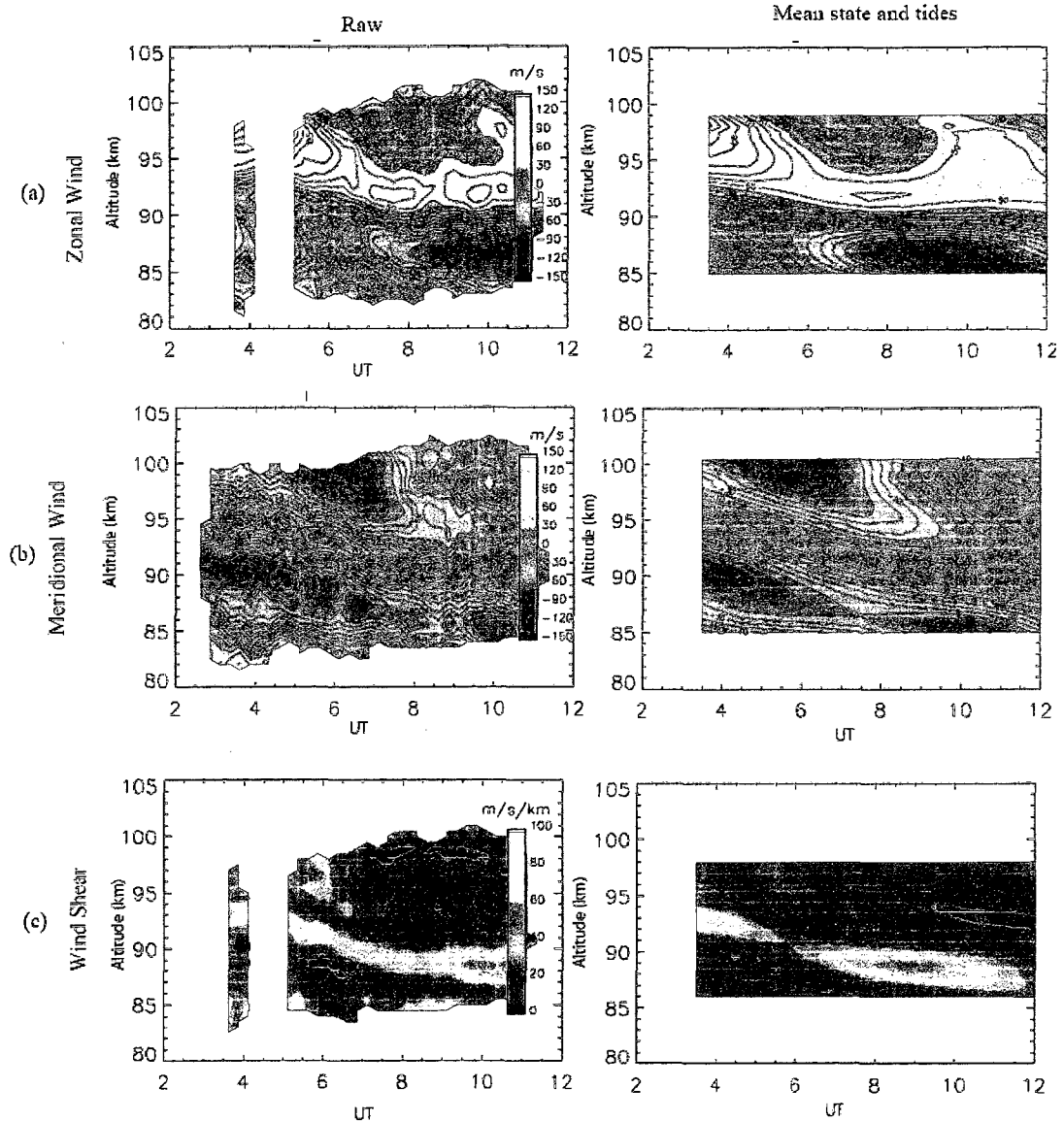


Figure 4.22. Lidar data on May 14 2003. (a) zonal wind ( $\text{ms}^{-1}$ ), (b) meridional wind ( $\text{ms}^{-1}$ ), (c) wind shear ( $\text{ms}^{-1}\text{km}^{-1}$ ). Column (from left to right): Raw data, mean state and tides only. The color scale is the same for the left and right column.

Although we only show one example in Figure 4.22, more than 60% of large wind shears ( $> 50 \text{ ms}^{-1}\text{km}^{-1}$ ) out of  $\sim 35$  nights are generated directly by the variability of solar tides at 85-100 km in 4 years of lidar data. The large wind shear is often accompanied by tidal waves with either shortened vertical wavelength or enhanced amplitude or both.

There have been studies to explain tides with shorter vertical wavelength and larger amplitude [Ortland and Alexander, 2006; Liu et al., 2007]: the interaction between tidal waves and transient planetary waves/GWs could be responsible for the significant short-term variation of tides.

Moreover, Figure 4.23(a) shows the local time dependence of the large wind shear occurrence at 95-100 km in winter. The tidal-period variation is obvious. The large nocturnal wind shear is likely to exist right around 19 - 21 Local Solar Time (LST) with the probability of 3-4 %. It is unlikely to be observed after midnight. Figure 4.23(b) gives the local time distribution of large amplitude of zonal and meridional wind shear. Peak of large zonal wind shears occur at 5-6 LST and at/before 19-20 LST; and large meridional wind shears likely occur around 3-4 LST. The phase of the zonal wind semidiurnal tide at 95-100 km in winter is  $\sim 6$  and 18 LST; the phase of the meridional wind semidiurnal tide is  $\sim 3$  and 15 LST [Yuan et al., 2008b]. The occurrence of large wind shears is consistent with the phase of the wind semidiurnal tides.

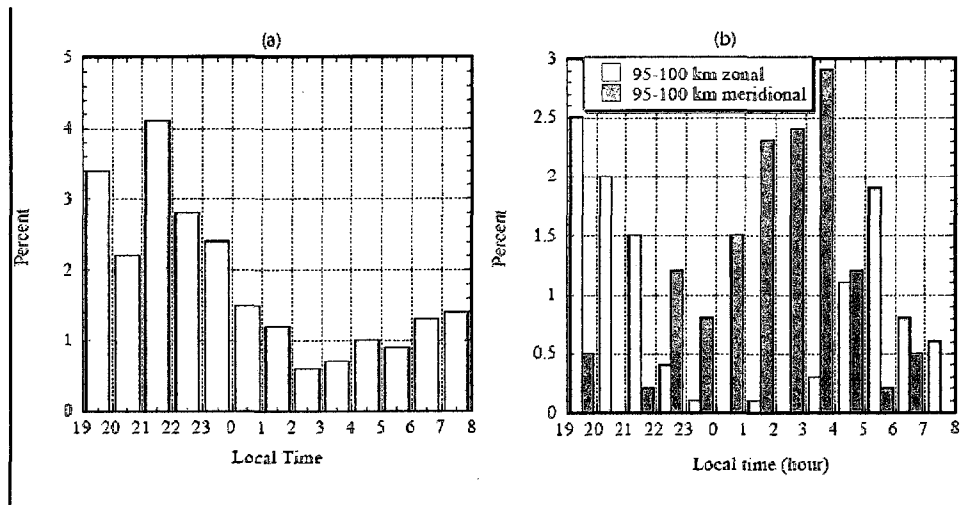


Figure 4.23 The local time dependence of (a) large total wind shear ( $> 40 \text{ ms}^{-1}\text{km}^{-1}$ ) (b) large amplitude of zonal and meridional wind shears ( $> 30 \text{ ms}^{-1}\text{km}^{-1}$ ) at 95-100 km in winter.

#### 4.3.4 Correlation between large wind shear and Brunt-Vaisala frequency

Besides the generation mechanism of the large wind shear, another important question is how are these large wind shears sustained in the lower thermosphere? A possible and obvious mechanism is that the large  $S$  could be maintained in the region of large  $N^2$  without breaking [Liu, 2007]. Using (3.25), we see that when  $N^2$  is large,  $S$  can reach a large value before the local atmosphere becomes dynamically unstable and induces KH billows, thus limiting further growth of wind shear. The maximum sustainable magnitude of wind shear  $S_{max}$  is  $2N$  based on the commonly assumed necessary but not sufficient condition for dynamic instability with  $Ri = 1/4 = N^2 / S_{max}^2$  [Liu, 2007]. For a given value of  $N$  representing the degree of atmospheric stability, an  $S$  value larger than  $S_{max}$  will induce dynamic instability and turbulence will be generated; the wind shear will be diminished by the turbulence until the local stability is reached again. As a result, large wind shears can exist longer in a region with higher convective stability, which depends on the temperature lapse rate. Since our Na lidar measures both wind and temperature directly, next we show the relation between  $N^2$  and  $S$  with the Na lidar data.

In Figure 4.24 and 4.25, we show points relating wind shear  $S$  to  $N^2$  at 15-min/2-km resolution from nocturnal lidar data taken in 2002-2005 at different altitude ranges for summer (June-July) and winter (November-February), respectively. The lidar data in summer covers less altitude range than the data in winter because of lower sodium density in summer. The blue line in each figure indicates the maximum allowed wind shear as a function of  $N^2$ , i.e.,  $S_{max} = 2\sqrt{N^2}$ . Above this curve,  $Ri$  is less than 0.25 and the atmosphere is dynamically unstable. When the flow becomes dynamically unstable,

due to the onset of turbulence, the amplitude of wind shear will decrease rapidly [Kim et al., 2009]. Not surprisingly in summer, within the measurement error bar due to photon noise (the blue cross), almost all the points lie below the blue line at all altitudes. There exist points above the blue curve beyond the error bar limit in both summer and winter. This implies that there are some incidences that large wind shear and dynamic instability exist simultaneously. Such occasional occurrences are to be expected due to both the fact that  $Ri < 0.25$  is only a necessary but not a sufficient condition for dynamic instability, and that it takes a finite time for a larger wind shear to react to local instability, to create turbulence and restore atmospheric stability. [Fritts et al., 1996]. Thus, for 15 min average data, large wind shears and dynamic instability could be observed simultaneously by the Na lidar. The green line shows  $N^2 = 0$ . On the left side of this line, the local atmosphere is convective unstable. Figure 4.26 and 4.27 give similar scattered points relating wind shear  $S$  to  $N^2$  at 1-hour/2-km resolution in summer and winter. With longer average time (as a result, longer relaxation time by turbulence), nearly no large wind shear satisfies dynamic instability within the error bar (above the blue line) in summer; and there are much fewer large wind shears and dynamic instability simultaneously observed in winter. In general, the observed wind shear and temperature gradient must satisfy the condition convective and dynamic stability.

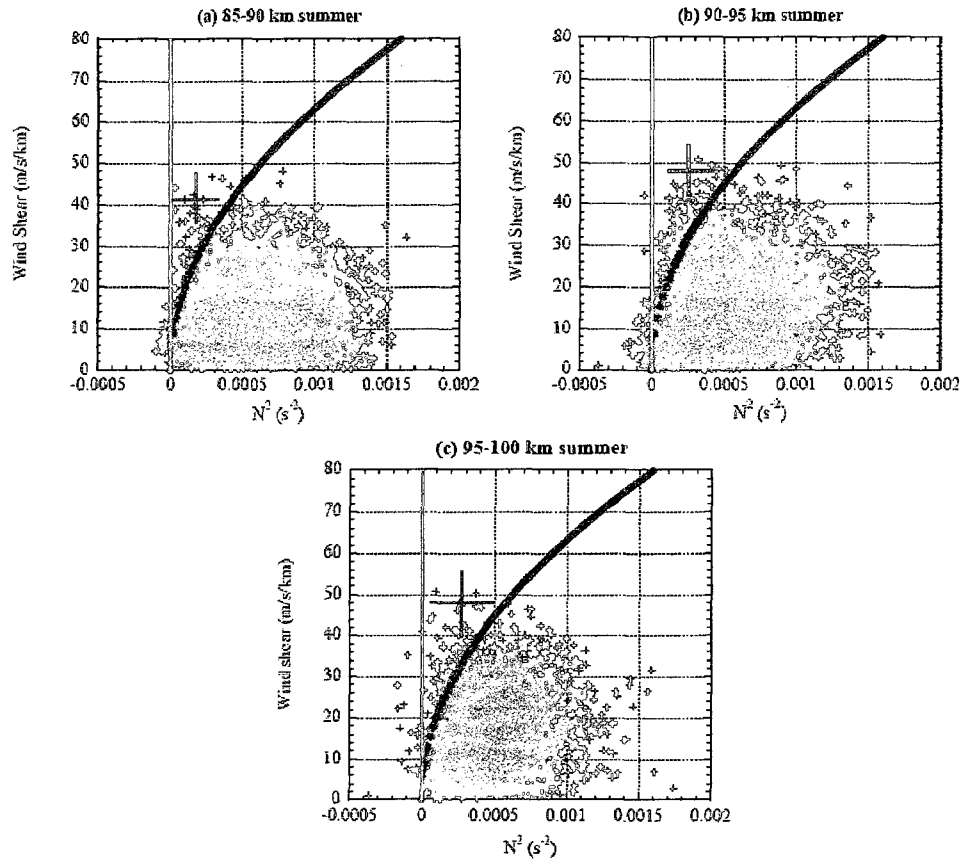


Figure 4.24 Brunt-Vaisala frequency square versus wind shear in summer with 15 min integration time and 2 km vertical resolution at the altitude of (a) 85-90 km (b) 90-95 km (c) 95-100 km. The blue cross indicates the averaged measurement uncertainty.

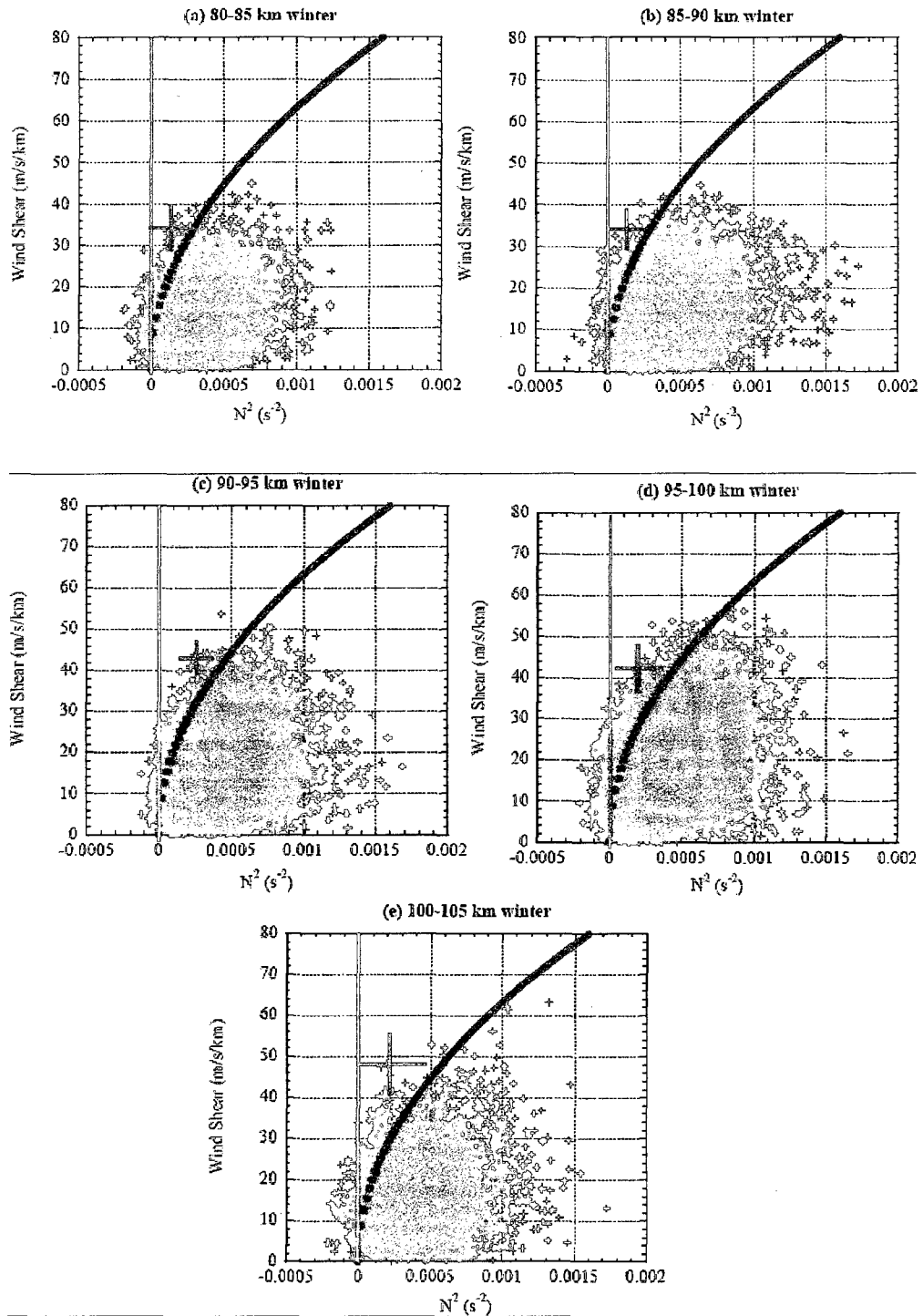


Figure 4.25. Brunt-Vaisala frequency square versus wind shear in winter with 15 min integration time and 2 km resolution at the altitude of (a) 80-85 km (b) 85-90 km (c) 90-95 km (d) 95-100 km (e) 100-105 km.

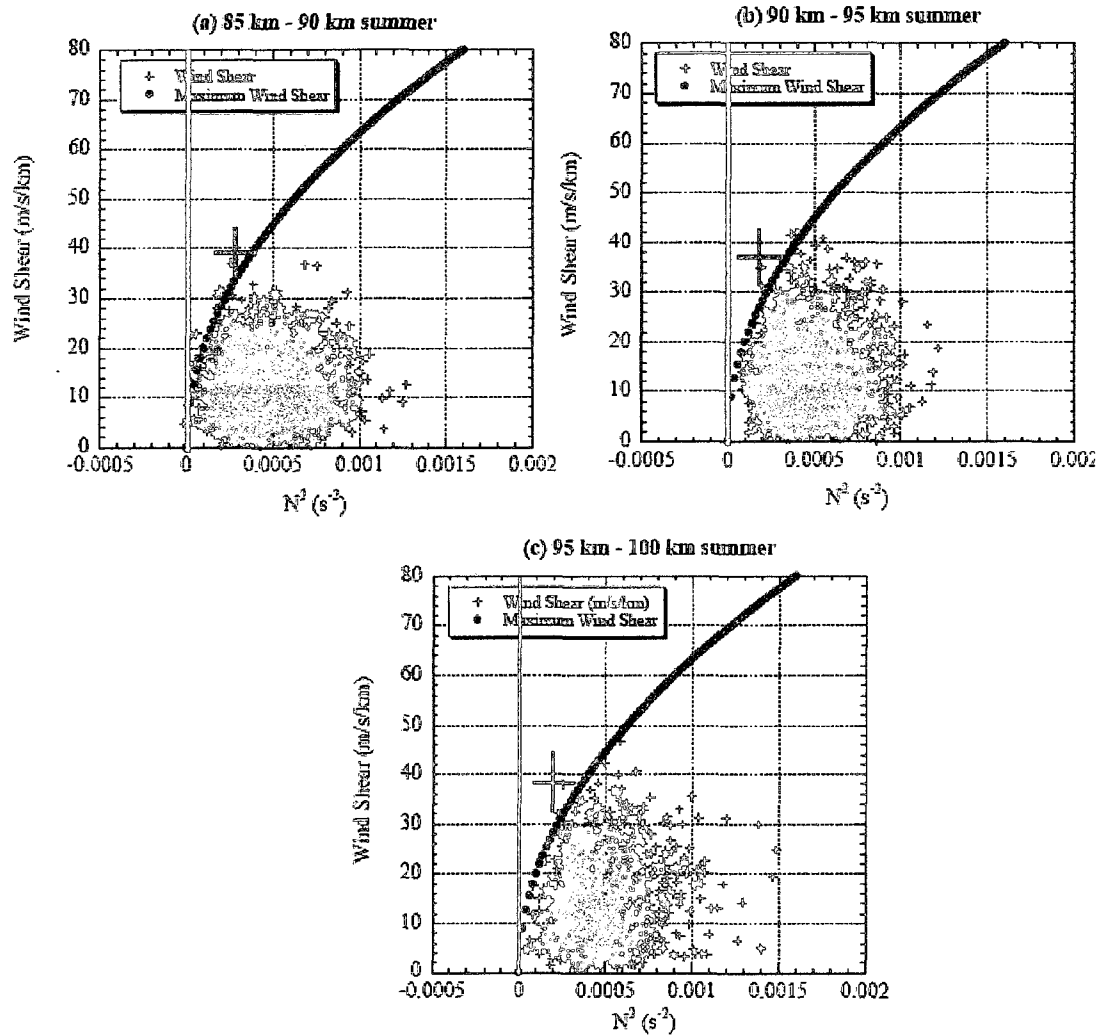


Figure 4.26. Brunt-Vaisala frequency square versus wind shear in summer with 1 hour integral time and 2 km vertical resolution at the altitude of (a) 85-90 km (b) 90-95 km (c) 95-100 km. The blue cross indicates the averaged measurement uncertainty.

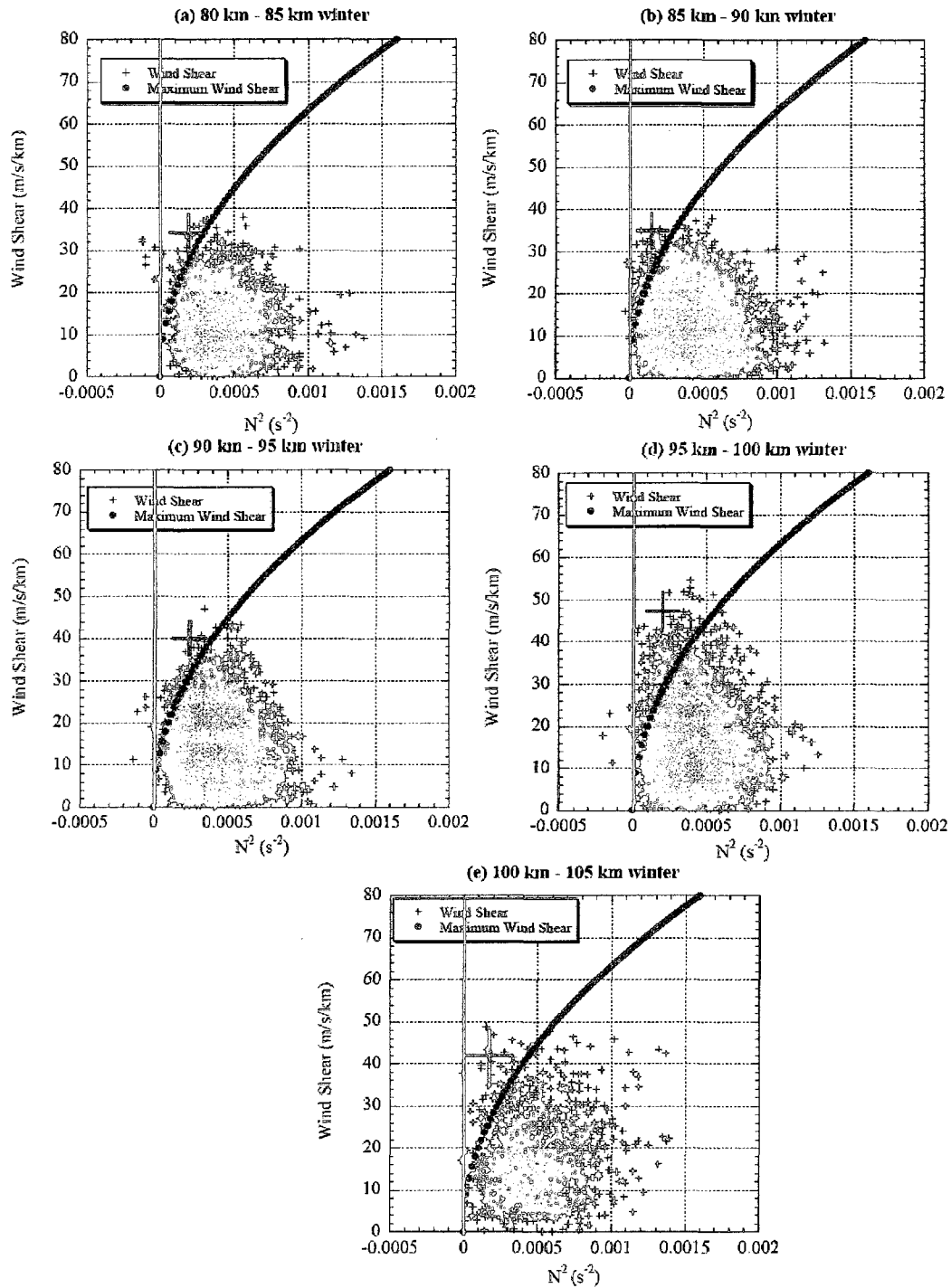


Figure 4.27. Brunt-Vaisala frequency square versus wind shear in winter with 1 hour integral and 2 km resolution at the altitude of (a) 80-85 km (b) 85-90 km (c) 90-95 km (d) 95-100 km (e) 100-105 km.

Now we discuss the possible seasonal variation of large wind shear vertical distribution in relation to the  $N^2$  profiles. To explain the seasonal variation of large wind shears, Figure 4.28 gives the maximum allowed wind shear deduced from nocturnal mean  $N^2$  profiles in summer and winter, including both the mean state and the effect of tidal waves, based on the hourly mean data. Following the definition of Brunt-Väisälä frequency as  $N^2 = \frac{g}{T}(dT/dz + \Gamma_a)$ , the maximum  $N^2$  exists at where the temperature gradient  $dT/dz$  is large and the temperature  $T$  is small. Only the mean temperature profile right above the mesopause meets this condition at the MLT region. Because the mesopause is at  $\sim 84$  km in summer and at  $> 100$  km in winter at mid-latitude [She and Von Zahn, 1998; Yuan et al., 2008a], the mean  $N^2$  has its maximum at 88 km in summer and at  $> 103$  km in winter, as shown in Figure 4.26.

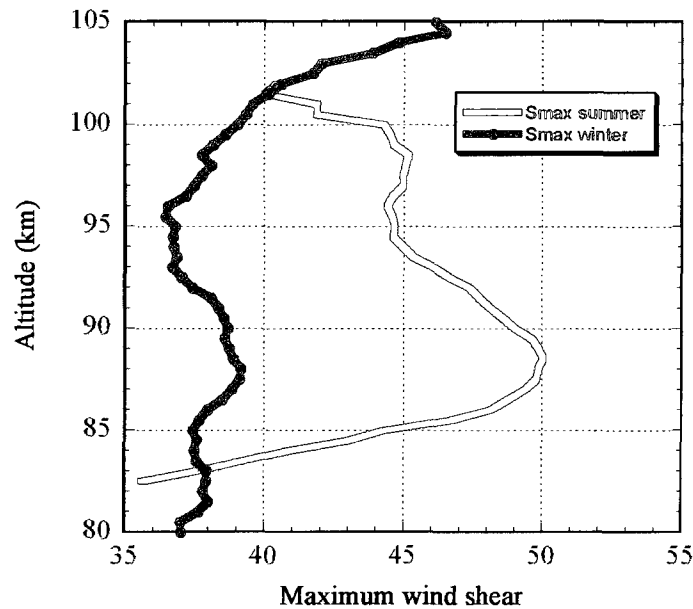


Figure 4.28. Maximum allowed wind shear  $S_{\max}$  in summer (red) and winter (blue).

To investigate the validity on the seasonal difference of the maximum allowable wind shears, we plot the superposition of the observed wind shears in winter and summer using the 15-min/2-km resolution nocturnal data in Figure 4.29. Qualitatively, the actual maximum wind shears in winter are observed to increase upward from  $\sim 30$  m/s/km at 90 km to  $\sim 50$  m/s/km at 105 km while the actual maximum shears between 87 and 98 km (with a mild peak at  $\sim 95$  km) are  $\sim 40$  m/s/km in summer. The altitude dependence of the maximum wind shears as observed in Fig. 4.29 is in qualitative agreement with the allowed wind shears deduced from nocturnal mean  $N^2$  profiles as shown in Fig. 4.28, except that the observed wind shears in summer [with values typically less than 40 m/s/km] appears to be less than the maximum allowed value deduced from  $N^2$ ,  $\sim 50$  m/s/km. To understand this discrepancy, we note that the large wind shear is generated by one mechanism, likely by semidiurnal tides and its sustainment limited by another mechanism, i.e., the dynamic stability. Therefore, the magnitude of large wind shears should be determined by both mechanisms. We have discussed in Section 4.3.4 that tidal waves could significantly contribute to the large wind shears in the MLT. The Na lidar has reported that the amplitude of the semidiurnal zonal and meridional wind above 90 km is growing much faster during winter than during summer at Fort Collins [Yuan et al., 2008b], as shown in Figure 4.30. The vertical wavelength of semidiurnal tide is also shorter (implicating larger wind shears) in winter. All these suggest that larger wind shears could be partially generated by semidiurnal tide in winter above 90 km. On the contrary, in summer the semidiurnal tidal amplitudes do not grow significantly below 95 km, compared to those in winter. Therefore, though the maximum allowed wind shears

can be as high as 50 m/s/km at 88 km in summer, most of the observed large wind shears remain below 40 m/s/km.

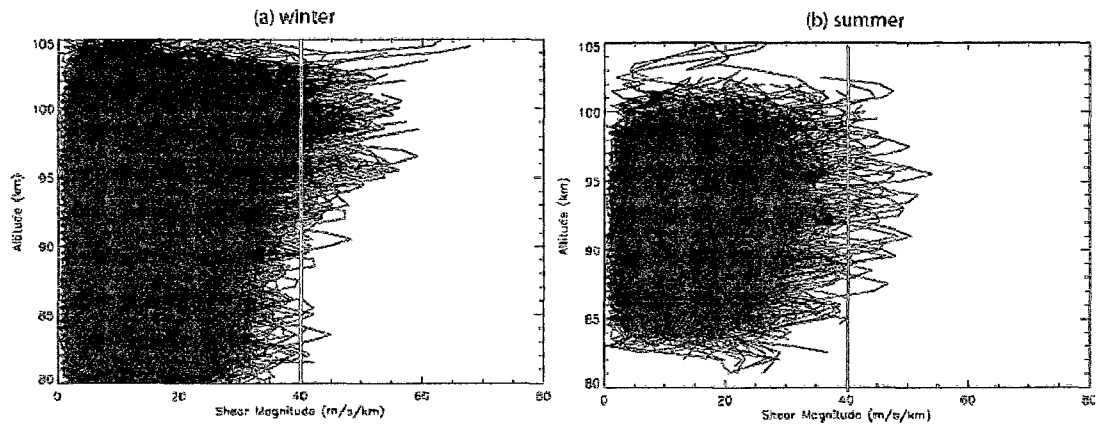


Figure 4.29 Superposition of the total wind shear magnitude profiles in 2002-2005 with 15 min average time in (a) winter and (b) summer.

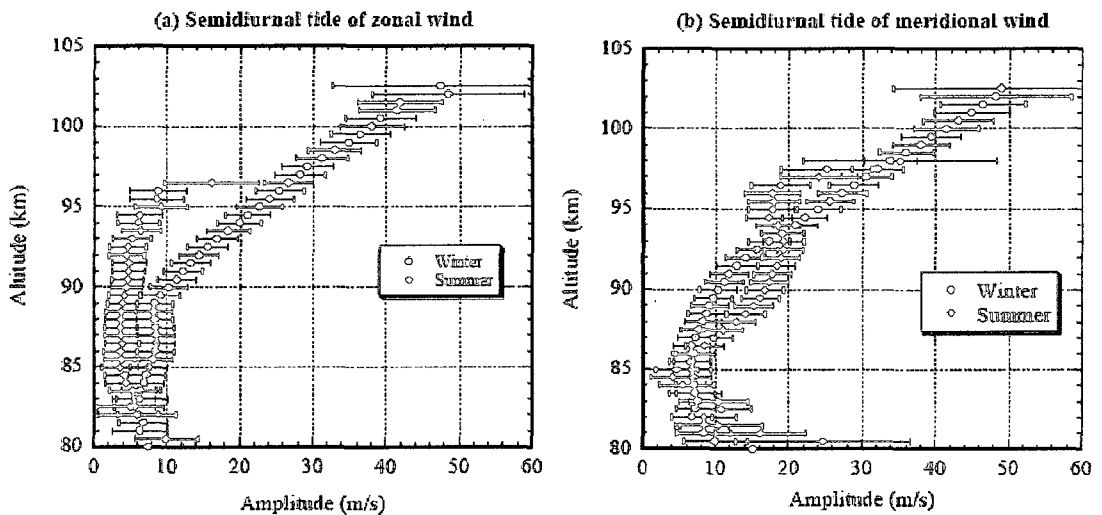


Figure 4.30 Semidiurnal tide amplitude of (a) zonal and (b) meridional wind at 80-105 km.

Since the Na lidar does not have enough signals to measure winds above 105 km, we can not observe the rapidly decreasing large wind shears and  $N^2$  in the thermosphere above 110 km, like the chemical release experiments did. Though the semidiurnal tidal

amplitude above turbopause (~110 km) no longer increases as altitude due to high molecular diffusion in this region [Forbes, 1982], the large wind shear still require a stable  $N^2$  profile as its background. Away from the mesopause, because the temperature increases rapidly with altitude due to absorption of highly energetic solar radiation,  $N^2$  decreases rapidly, so does the maximum allowed wind shear. Though we do not have lidar temperature measurements above 105 km, using TIME-GCM simulation, Liu [2007] has shown the similar profiles of the maximum wind shear at 80-140 km deduced from  $N^2$ , to be compared to the measured wind shears in Larsen [2002].

In this chapter, we have discussed three important middle atmosphere phenomena observed by the Na lidar and the OH imager: concentric gravity waves, mesospheric bores and large wind shears. The technical development described in Chapter 2 assures that the data used here has enough signal to noise ratio and temporal/spatial resolution. Gravity wave theories introduced in Chapter 3 are cited here to explain the observations, e.g., wave generation, gravity wave dispersion relation, wave filtering, wave ducting and wave breaking. Three scientific projects all lead to publications. We will discuss the future work in next chapter to extend these studies in the near future.

## References:

- Acott, P., Mesospheric Momentum flux studies over Fort Collins CO (41N, 105W), Ph.D. dissertation, Colorado State University, 2009.
- Alexander, M.J., J. R. Holton, and D. R. Durran, The gravity wave response above deep convection in a squall line simulation, *J. Atmos. Sci.*, *52*(12), 2212-2226, 1995.
- Alexander, M.J., P.T. May and J.H. Beres, Gravity waves generated by convection in Darwin area during the Darwin Area Wave Experiment, *J. Geophys. Res.*, *109*, D20S04, doi:10.1029/2004JD004729, 2004.
- Brown L.B, A.J. Gerrard, J.W. Meriwether and J.J Mekela, All-sky imaging of mesospheric fronts in OI 557.7 nm and broadband OH airglow emissions: Analysis of frontal structure, atmospheric background conditions and potential sourcing mechanisms, *J. Geophys. Res.*, *109*, D19104, doi:10.1029/2003JD004223, 2004.
- Collins, S. C., et al., A study of the role of ion-molecule chemistry in the formation of sporadic sodium layers, *J. Atmosph. Sol.-Terr. Phys.*, *64*, 845-860, doi: 10.1016/S1364-6826(02)00129-3, 2002.
- Dewan, E. M., R. H. Picard, R.R. O'Neil, H.A. Gardiner, J. Gibson, J.D. Mill, E. Richards, M. Kendra, and W.O. Gallery, MSX satellite observations of thunderstorm-generated gravity waves in mid-wave infrared images of the upper stratosphere, *Geophys. Res. Lett.*, *25*, 939-942, 1998.
- Dewan, E., and R. Picard, Mesospheric bores, *J. Geophys. Res.*, *103*(D6), 6295-6305, 1998.
- Dewan, E., and R. Picard, On the origin of mesospheric bores, *J. Geophys. Res.*, *106*(D3), 2921-2927, 2001.
- Dutton, J. A., *The ceaseless wind*, 79 pp., Dover Publications, INS, New York, 1986
- Fechine, J., Medeiros, A.F., Buriti, R.A., Takahashi, H., Gobbi, D., Mesospheric bore events in the equatorial middle atmosphere. *J. Atmos. Terr. Phys.*, *67*, 1774 – 1778, 2005.
- Fovell, R., D. Durran, and J. R. Holton, Numerical Simulations of Convectively Generated Stratospheric Gravity Waves, *J. Atmos. Sci.*, *49*, 1427-1442, 1992.
- Franke P. M., R. L. Collins, Evidence of gravity wave breaking in lidar data from the mesopause region, *Geophys. Res. Lett.*, *30* (4), 1155, doi:10.1029/2001GL014477, 2003.

- Fritts, D. C., T. L. Palmer, O. Andreassen and I. Lie, Evolution and breakdown of Kelvin-Helmholtz billows in stratified compressible flows, part I, Comparison of two- and three-dimensional flows, *J. Atmos. Sci.*, 53, 3173-3191, 1996.
- Fritts, D. C., and J. M. Alexander, Gravity wave dynamics and effects in the middle atmosphere, *Reviews of Geophysics*, 41; pages 3.1, 2003.
- Fritts, D. C., B. P. Williams, C. Y. She, J. D. Vance, M. Rapp, F.-J. Lübken, A. Müllemann, F. J. Schmidlin, R. A. Goldberg, Observations of extreme temperature and wind gradients near the summer mesopause during the MaCWAVE/MIDAS rocket campaign, *Geophys. Res. Lett.*, 31, L24S06, doi:10.1029/2003GL019389, 2004.
- Garcia, F. J., M. J. Taylor, and M.C. Kelley, Two-dimensional spectral analysis of mesospheric airglow image data, *App. Opt.*, 36(29), 7374-7385, 1997.
- Hecht, J. H., S. Kovalam, P. T. May, G. Mills, R. A. Vincent, R. L. Walterscheid, J. Woithe, Airglow imager observations of atmospheric gravity waves at Alice Springs and Adelaide, Australia during the Darwin Area Wave Experiment (DAWEX), *J. Geophys. Res.*, 109, D20S05, doi:10.1029/2004JD004697, 2004.
- Hecht, J. H., Instability layers and airglow imaging, *Rev. Geophys.*, 42, RG1001, doi:10.1029/2003RG000131, 2004.
- Hines, C. O., Internal atmospheric gravity waves at ionospheric heights, *Can. J. Phys.*, 38, 1441-1481, 1960.
- Hines, C. O., Generalization of the Richardson criterion for the onset of atmospheric turbulence, *Quart. J. R. Met Soc.*, 97, 429-439, 1971.
- Horinouchi, T., T. Nakamura, and J.-i. Kosaka, Convectively generated mesoscale gravity waves simulated throughout the middle atmosphere, *Geophys. Res. Lett.*, 29(21), 2007, doi:10.1029/2002GL016069, 2002.
- Hung, R.J., T. Phan, and R.E. Smith, Observations of gravity waves during the extreme tornado outbreak of 3 April 1974, *J. Atmos. Terr. Phys.*, 40, 831-843, 1978.
- Hysell, D. L., J. L. Chau, and C. G. Fesen, Effects of large horizontal winds on the equatorial electrojet, *J. Geophys. Res.*, 107 (A8), 1215, doi:10.1029/2001JA000217, 2002.
- Kaladze, T. D., D. J. Wu, O. A. Pokhotelov, R. Z. Sagdeev, L. Stenflo, P. K. Shukla, Rossby-wave driven zonal flows in the ionospheric E-layer, *J. Plasma Physics*, 73(1), 131-140, 2007.
- Kim, E., H. Liu, and J. Anderson, Probability distribution function for self-organization of shear flows, *Phys. Plasmas*, 16, 052304, 2009.

- Lane, T. P., M. J. Reeder, and T. L. Clark, Numerical modeling of gravity waves generated by deep tropical convection, *J. Atmos. Sci.*, 58, 1249-1274, 2001.
- Lane, T.P., R.D. Sharman, T.L. Clark, and H.-M. Hsu, An investigation of turbulence generation mechanisms above deep convection, *J. Atmos. Sci.*, 60, 1297-1321, 2003.
- Lane, T.P. and R.D. Sharman, Gravity wave breaking, secondary wave generation, and mixing above deep convection in a three-dimensional cloud model, *Geophys. Res. Lett.*, 33, L23813, doi:10.1029/2006GL027988, 2006.
- Larsen M. F. and W. E. Swartz, Gravity-wave generation by thunderstorms observed with a vertically-pointing 430 MHz radar, *Geophys. Res. Lett.*, 9(5), 571-574, 1982.
- Larsen, M. F., A shear instability seeding mechanism for quasiperiodic radar echoes, *J. Geophys. Res.*, 105(A11), 24,931–24,940, 2000.
- Larsen, M. F., Winds and shears in the mesosphere and lower thermosphere: Results from four decades of chemical release wind measurements, *J. Geophys. Res.*, 107 (A8), 1216, doi:10.1029/2001JA000218, 2002.
- Larsen M. F., A. Z. Liu, R. L. Bishop, and J. H. Hecht, TOMEX: A comparison of lidar and sounding rocket chemical tracer wind measurements, *Geophys. Res. Lett.*, 30 (7), 1375, doi:10.1029/2002GL015678, 2003.
- Larsen, M. F. and C. G. Fesen, Accuracy issues of the existing thermospheric wind models: Can we rely on them in seeking solutions to wind-driven problems?, *Ann. Geophys.*, 27(6), 2277-2284, 2009.
- Laughman B., D. C. Fritts, and J. Werne, Numerical simulation of bore generation and morphology in the thermal and Doppler ducts, *Ann. Geophys.*, 27, 511-523, 2009.
- Li F., A. Z. Liu, G. R. Swenson, Characteristics of instabilities in the mesopause region over Maui, Hawaii, *J. Geophys. Res.*, 110, D09S12, doi:10.1029/2004JD005097, 2005.
- Liu, A. Z., and G. R. Swenson, A modeling study of O<sub>2</sub> and OH airglow perturbations induced by atmospheric gravity waves, *J. Geophys. Res. (Atmospheres)*, 108 (D4), ACH 11-1, CiteID 4151, DOI 10.1029/2002JD002474, 2003.
- Liu H.-L., On the large wind shear and fast meridional transport above the mesopause, *Geophys. Res. Lett.*, 34, L08815, doi:10.1029/2006GL028789, 2007.
- Liu H.-L., T. Li, C.-Y. She, J. Oberheide, Q. Wu, M. E. Hagan, J. Xu, R. G. Roble, M. G. Mlynczak, J. M. Russell III, Comparative study of short-term diurnal tidal variability, *J. Geophys. Res.*, 112, D18108, doi:10.1029/2007JD008542, 2007.

- Marwitz, J.D, and E.X. Berry, The airflow within the weak echo region of an Alberta hailstorm, *J. Appl. Meteor.*, 10, 487-492, 1971.
- Mathews, J. D., Sporadic E: current views and recent progress, *J. Atmos. Terr. Phys.*, 60(4), 413-435, 1998.
- Medeiros, A. F., Taylor, M. J., Takahashi, H., Batista, P. P., Gobbi, D., An unusual airglow wave event observed at Cachoeira Paulista 23oS, *Adv. Space Res.*, 27, 1749 – 1754, 2001.
- Meriwether, J. W., and C. S. Gardner, A review of the mesosphere inversion layer phenomenon, *J. Geophys. Res.*, 105(D10), 12,405–12,416, 2000.
- Nakamura, T., T. Fukushima, T. Tsuda, C.-Y., She, B.P. Williams, D. Krueger and W. Lyons, Simultaneous observation of dual-site airglow imagers and a sodium temperature-wind lidar, and effect of atmospheric stability on the airglow structure, *Adv. Space Res.*, 35, 1957-1963, 2005.
- Nielsen, K., M. J. Taylor, P. D. Pautet, D. C. Fritts, N. Mitchell, C. Beldon, W. Singer, F. J. Schmidlin, and R. A. Goldberg, Propagation of short-period gravity waves at high-latitudes during the MaCWAVE winter campaign, *Annals. Geophys.*, 24, 1-17, 2006.
- Offermann, D., M. Jarisch, J. Oberheide, O. Gusev, I. Wohltmann, J. M. Russell III, M. G. Mlynczak, Global wave activity from upper stratosphere to lower thermosphere: A new turbopause concept, *J. Atmos. Terr. Phys.*, 68, 1709-1729, 2006.
- Oppenheim M. M., G. Sugar, N. O. Slowey, E. Bass, J. L. Chau, S. Close, Remote sensing lower thermosphere wind profiles using non-specular meteor echoes, *Geophys. Res. Lett.*, 36, L09817, doi:10.1029/2009GL037353, 2009.
- Ortland D. A., M. J. Alexander, Gravity wave influence on the global structure of the diurnal tide in the mesosphere and lower thermosphere, *J. Geophys. Res.*, 111, A10S10, doi:10.1029/2005JA011467, 2006.
- Piani, C., D. Durran, M. J. Alexander, and J. R. Holton, A numerical study of three-dimensional gravity waves triggered by deep tropical convection and their role in the dynamics of the QBO, *J. Atmos. Sci.*, 57(22), 3689–3702, 2000.
- Pierce, A. D. and S. C. Coroniti, A Mechanism for the Generation of Acoustic-Gravity Waves During Thunderstorm Formation, *Nature*, 210, 1209–1210, 1966.
- Roble, R. G., Energetics of the mesosphere and thermosphere, in *The Upper Mesosphere and Lower Thermosphere: A Review of Experiment and Theory*, *Geophys. Monogr.*, No. 87, edited by R. M. Johnson and T. L. Killeen, pp. 1-20, American Geophysical Union, 1–20., 1995.

- Sentman, D. D., E. M. Wescott, R. H. Picard, J. R. Winick, H. C. Stenbaek Nielsen, E. M. Dewan, D. R. Moudry, F. T. Sao Sabbas, M. J. Heavner, and J. Morrill, Simultaneous observations of mesospheric gravity waves and sprites generated by a midwestern thunderstorm, *J. Atmos. Terr. Phys.*, *65*, 537-550, 2003.
- Seyler C. E., Internal waves and undular bores in mesospheric inversion layers, *J. Geophys. Res.*, *110*, D09S05, doi:10.1029/2004JD004685, 2005.
- She C.-Y., and R.P. Lowe, Seasonal temperature variations in the mesopause region at mid-latitude: comparison of lidar and hydroxyl rotational temperatures using WINDII\UARS OH height profiles, *J. Atmos. Terr. Phys.*, *60(16)*, 1573-1583, 1998.
- She, C., and U. von Zahn, Concept of a two-level mesopause: Support through new lidar observations, *J. Geophys. Res.*, *103(D5)*, 5855-5863, 1998.
- She, C. Y., J. Sherman, T. Yuan, B. P. Williams, K. Arnold, T. D. Kawahara, T. Li, L. Xu, J. D. Vance and David A. Krueger, The first 80-hour continuous lidar campaign for simultaneous observation of mesopause region temperature and wind, *Geophys. Res. Lett.*, *30*, *6*, *52*, 10.1029/2002GL016412, 2003.
- She C. Y., Initial full-diurnal-cycle mesopause region lidar observations: diurnal-means and tidal perturbations of temperature and winds over Fort Collins, CO (41N; 105W), *J. of Atmos. and Sol. Terre. Phys.*, *66*, 663-674, 2004.
- She C. Y., T. Li, B. P. Williams, T. Yuan, R. H. Picard, Concurrent OH imager and sodium temperature/wind lidar observation of a mesopause region undular bore event over Fort Collins/Platteville, Colorado, *J. Geophys. Res.*, *109*, D22107, doi:10.1029/2004JD004742, 2004.
- Sherman, J. P., and C.-Y. She, Seasonal variation of mesopause region wind shears, convective and dynamic instabilities above Fort Collins, CO: A statistical study, *J. Terr. Sol. Atmos. Phys.*, *68*, 1061-1074, 2006.
- Shiokawa, K., Suzuki, S., Otsuka, Y., Ogawa, T., Nakamura, T., Mlynyczak, M. G., Russell III, M. J., A Multi-Instrument Measurement of a Mesospheric Front-Like Structure at the Equator. *J. Meteo. Soc. Japan*, *84*, 305 – 316, 2006.
- Simkhada, D. B., J. B. Snively, M. J. Taylor, and S. J. Franke, Analysis and Modeling of Ducted and Evanescent Gravity Waves Observed in the Hawaiian Airglow, Submitted to *Ann. Geophys.*, 2009.
- Smith, S. M., M. Mendillo, J. Baumgardner, and R. R. Clark, Mesospheric gravity wave imaging at subauroral site: First results from Millstone Hill, *J. Geophys. Res.*, *106*, 27119-27130, 2000.

- Smith S. M., M. J. Taylor, G. R. Swenson, C.-Y. She, W. Hocking, J. Baumgardner, and M. Mendillo, A multidagnostic investigation of the mesospheric bore phenomenon, *J. Geophys. Res.*, *108* (A2), 1083, doi:10.1029/2002JA009500, 2003.
- Smith, S. M.; Friedman, J.; Raizada, S.; Tepley, C.; Baumgardner and J.; Mendillo, M., Evidence of mesospheric bore formation from a breaking gravity wave event: simultaneous imaging and lidar measurements, *J. of Atmos. and Sol. Terre. Phys.*, *67*(4), 345-356, 2005.
- Sonmor, L. J., and G. P. Klaassen, Toward a unified theory of gravity wave breaking, *J. Atmos. Sci.*, *54*, 2655-2680, 1997.
- Suzuki, S., K. Shiokawa, Y. Otsuka, T. Ogawa, K. Nakamura, and T. Nakamura, A concentric gravity wave structure in the mesospheric airglow images, *J. Geophys. Res.*, *112*, D02102, doi: 10.1029/2005JD006558, 2007.
- Taylor, M.J., and M. A. Hapgood, Identification of a thunderstorm as a source of short period gravity waves in the upper atmospheric nightglow emissions, *Planet. Space Sci.*, *36*, 975-985, 1988.
- Taylor, M. J., M. B. Bishop, and V. Taylor, All-sky measurements of short period waves imaged in the OI (557.7nm), Na(589.2nm) and near infrared OH and O2(0,1) nightglow emissions during the ALOHA-93 campaign, *Geophys. Res. Lett.*, *22*(20), 2833-2836, 1995.
- Taylor, M., D. Turnbull, and R. Lowe, Spectrometric and Imaging Measurements of a Spectacular Gravity Wave Event Observed During the ALOHA-93 Campaign, *Geophys. Res. Lett.*, *22*(20), 2849-2852, 1995.
- Vadas, S. L. and D. C. Fritts, Reconstruction of the gravity wave field from convective plumes via ray tracing, *Annals. Geophys.*, in press, 2008.
- Vadas, S.L., M.J. Taylor, P-D. Pautet, P. Stamus, D.C. Fritts, H.-L. Liu, F.T. Sao Sabbas, V.T. Rampinelli, P. Batista, and H. Takahashi, Convection: the likely source of of the medium-scale gravity waves observed in the OH airglow layer near Brasilia, Brazil, during the SpreadFEx campaign, *Ann. Geophys.*, in press, 2008a.
- Vadas, S. L., J. Yue, C.-Y. She, P. Stamus, and A. Z. Liu, A model study of the effects of winds on concentric rings of gravity waves from a convective plume near Fort Collins on 11 May 2004, *J. Geophys. Res.*, in press, 2008b.
- Waldock, J.A. and T.B. Jones, Source regions of medium scale travelling ionospheric disturbances observed at mid-latitudes, *J. Atmos. Terres. Phys.*, *49*, 105-114, 1987.
- Whitehead, J., Production and Prediction of Sporadic E, *Rev. Geophys.*, *8*(1), 65-144, 1970.

- Williams B. P., M. A. White, D. A. Krueger, and C. Y. She, Observation of a large amplitude wave and inversion layer leading to convective instability in the mesopause region over Fort Collins CO (41°N, 105°W), *Geophys. Res. Lett.*, 29 (17), 1850, doi:10.1029/2001GL014514, 2002.
- Xu J., A. K. Smith, R. L. Collins, C.-Y. She, Signature of an overturning gravity wave in the mesospheric sodium layer: Comparison of a nonlinear photochemical-dynamical model and lidar observations, *J. Geophys. Res.*, 111, D17301, doi:10.1029/2005JD006749, 2006.
- Yuan T., C.-Y. She, D. A. Krueger, F. Sassi, R. Garcia, R. G. Roble, H.-L. Liu, H. Schmidt, Climatology of mesopause region temperature, zonal wind, and meridional wind over Fort Collins, Colorado (41°N, 105°W), and comparison with model simulations, *J. Geophys. Res.*, 113, D03105, doi:10.1029/2007JD008697, 2008a.
- Yuan T., C.-Y. She, H. Schmidt, D. A. Krueger, S. Reising, Seasonal variations of semidiurnal tidal-period perturbations in mesopause region temperature, zonal and meridional winds above Fort Collins, CO (40.6°N, 105°W), *J. Geophys. Res.*, VOL. 113, D20103, doi:10.1029/2007JD009687, 2008b.
- Zhang, F., Generation of Mesoscale Gravity Waves in Upper-Tropospheric Jet-Front Systems, *J. Atmos. Sci.*, 61, 440-457, 2004.
- Zhao, Y., A. Z. Liu, and C. S. Gardner, Measurements of atmospheric stability in the mesopause region at Starfire Optical Range, NM, *J. Terr. Sol. Atmos. Phys.*, 65, 219-232, 2003.

## **Chapter 5: Conclusions and Future Work**

This dissertation presents science from two ground-based optical instruments: the CSU Na lidar and the Yucca Ridge OH airglow imager. The CSU Na lidar can observe the temperature, zonal and meridional wind, gravity wave momentum flux. The OH airglow imager can automatically monitor the gravity wave activities on the horizontal plane at the height of 87 km. The CSU lidar provides the necessary temperature and wind information in the mesopause region (80-105 km). The knowledge of the background is helpful to deduce the intrinsic phase velocity and vertical wavelength for gravity waves. This leads to the full characteristic of the gravity waves observed by the imager. Therefore, more interesting science can be investigated with both instruments in operation.

In this dissertation, after a brief description of the sodium lidar system and airglow imager in Chapter 2, basic gravity wave theory was reviewed in Chapter 3. Chapter 4 presented the results of observations by the CSU Na lidar and the OH airglow imager.

### **5.1 Conclusions**

The first scientific topic was the observations of concentric gravity waves on 9 nights using the all-sky OH imager. These waves consisted of nearly perfect circles, “squashed” rings, and arcs. In every case, deep convection in the form of over-shoot above the

tropopause was present an hour or more prior below the observed event of the CGW. According to the radiosonde data, the wind below 30-35 km on those nights was weak, less than 20 m/s. A detailed study of the gravity wave on 11 May 2004 was performed. On that night, two nearly circular concentric gravity waves were observed, with different centers. Strong convective updrafts that “overshot” the tropopause were identified as the sources of the two concentric gravity waves. The locations of these convective plumes coincide with the centers of the concentric gravity waves to within  $0.2^\circ$  in lat/long. The horizontal winds from radiosonde and TIME-GCM model data between the tropopause and mesopause were small. The modeling study by a collaborator, S. Vadas, confirmed that the centers of the waves coincided with that of the convective plumes when the intervening winds are weak. The model study also finds that the concentric gravity waves appear as concentric rings for climatological April winds. The observed horizontal wavelengths on 11 May 2004 as a function of radius and time are in good agreement with the predictions of the Boussinesq gravity wave dispersion relation (with assumed zero winds and constant temperatures) for radii between 150 and 200 km. The apparent periods are in reasonable agreement. Somewhat better agreement is obtained when anelastic effects and varying winds are employed in the model. By studying all 9 cases in which nearly concentric gravity waves were observed by the OH imager, we conclude that the occurrence frequency of the mesospheric observation of CGW is small, about  $9/723$ , or about 1.25%. Due to the strong seasonal occurrence after the spring equinox and just prior to the fall equinox, which coincides with times when the mean background wind is nearly zero, weak mean background wind between the tropopause and mesopause was hypothesized to be a necessary condition for enabling concentric gravity waves to

propagate upward as concentric rings to the OH airglow layer. Thus, we hypothesize that during the times when the 9 events occurred, the mean wind as well as the winds from tides and planetary waves were likely small.

In general, in northeastern Colorado, the tropospheric winds tend to be westerly (toward the east) and the sources of thunderstorms are likely to be east of Colorado; thus the winds may blow the convective clouds eastward out of the OH imager field of view, enabling a relatively higher rate of observation of concentric gravity waves for northeastern Colorado than for other imager locations.

Secondly, we report the observation, of large-scale gravity waves on the night of 09 Oct 2007 from the Kyoto University OH imager. These gravity waves steepened and generated mesospheric bores after they were trapped in a temperature inversion layer, in a manner similar to recent numerical simulations in the literature. To our knowledge, this is the first observation of mesospheric bores being generated. We also observed that the undulations trailing a bore front can sometimes coalesce into a huge soliton-like perturbation. When these perturbations passed a lidar beam, the potential temperature contours become vertical, implicating convective atmospheric instability. After the temperature inversion layer vanished, no more mesospheric bores could be identified. This fact suggests the need of a duct to form and sustain an internal bore; the required background atmospheric conditions were indeed verified by the concurrent Na lidar data. The weather map shows the existence of a cold front system in the lower atmosphere; the alignment of the long wavelength gravity waves with the cold front implies that the latter may be the source of the former. Besides the 09 Oct 2007 case reported here, all 7

mesospheric bores we observed in Fort Collins can be linked to a cold front system in terms of propagation direction and time.

The third project was on the large wind shears in the lower thermosphere. For this study, we used only lidar data between 2002 and 2005, ~1600 hours of nocturnal temperature and horizontal wind observations. Since the nighttime observation has sufficient signal-to-noise ratio, we form high resolution temperature, zonal and meridional wind profiles with 2 km and 15 min height and temporal resolution. With all data acquired in the full-diurnal-cycles, we also form hourly mean with 2 km vertical resolution; these data are used to determine the mean state and tidal-period oscillations with 24 hour continuous data. By comparing the wind shear profiles with different integration time (15 min and 1 hour) and the same vertical resolution, we find that the large wind shears in questions are related to longer period waves with tidal period (24h, 12h, 8h, 6h), rather than gravity waves with less than 2 hour period. A case study is shown to illustrate the possible relation between large wind shears and semidiurnal tides. Our high resolution data have demonstrated that the value of Brunt-Väisälä frequency,  $N$ , indeed confines the maximum magnitude of wind shear. Those wind shears with magnitudes greater than  $2N$  become dynamically unstable, and are prevented from growing. Owing to the corresponding relationship between temperature gradient and  $N^2$ , the altitudes with highest wind and wind shear exist at a few kilometers above the mesopause, ~84 km in summer and >100 km in winter for wind shear above  $50 \text{ ms}^{-1}\text{km}^{-1}$ . Combining the seasonal variations of tidal wave amplitude and mean temperature profiles, we can qualitatively explain the vertical distribution of large wind shears during summer and winter.

These three observational studies are connected together by the theory of gravity waves. The concentric gravity wave study gives a spectacular example of one type of gravity wave sources, deep convections. The wave propagation is in agreement with the gravity wave dispersion relation presented in Chapter 3. The statistics of the concentric gravity wave observation is consistent with the effect of mean wind filtering. The mesospheric bore study illustrates importance of the wave ducting. The nonlinear interaction of gravity waves is shown to be capable of steepening the wave front and generate a bore. The large wind shear study shows that the dynamic instability threshold limits the growing of wave amplitude (not only gravity waves, but also tidal waves and planetary waves) leading to high correlations between the maximum observed wind shear and  $N^2$ .

## 5.2 Future work

The studies presented in Chapter 4 are not the end of the story. Future work has been planned for each of the project.

A new OI band imager purchased by T. Nakamura at National Institute of Polar Research (Japan) will be installed at Yucca Ridge Field Station this fall. This additional channel will allow the observation of gravity waves at the height of  $\sim 97$  km. Along with the current OH airglow imager, the observations of concentric gravity waves and mesospheric bores will be continued. With more examples, we can conduct a better statistical study of the correlation of mean wind filtering and the occurrence of concentric gravity waves near equinoxes. This will strengthen our conclusions. In the same manner, we have observed the mesospheric bores all traveling from the southeast mostly in

October. More examples and the investigation of relative phase of a bore at different altitudes will help us draw more convincing conclusion.

Large telescopes and high efficiency PMTs were added to the CSU lidar system in 2006. This upgrade increases the signal level by at least 8 times. This yields higher temporal ( $\sim 5$  min) and height ( $\sim 1$  km) resolution lidar data with good signal to noise ratio. With accumulated lidar data at higher resolution, we can investigate in more depth on the correlation between large wind shears and smaller-scale gravity waves.

The merit of the collaboration between the observation and simulation has been demonstrated in the study of the concentric gravity waves. The agreement between the observation and the ray-tracing result is encouraging. The comparison work will be continued. On the night of September 8 2005, two groups of concentric gravity waves were generated from two deep convections thousands of km apart, one in Colorado, one in Nebraska. Multiple sources have been added into the ray-tracing program by S. Vadas. We will simulate the multiple concentric gravity waves simultaneously with real radar and radiosonde wind instead of the model wind. Interesting comparison results are expected.

In a broad view, the author would like to share his vision on the future of the Na Doppler lidar, as a tradition of every graduate from the CSU lidar group. With the effort of every past student, the development of a stable component to enhance the capability of the wind/temperature Na lidar has been made, a stabilized Faraday filter allowing daytime measurement, a chirp monitoring subsystem to correct the bias in the PDA, a setup of larger telescopes and high-efficient PMTs to measure the gravity wave momentum flux, a stable electronics and control system. The current system holds the

record of the same type fluorescence lidar in longest continuous observation (9 days, She et al. [2004]) and the longest dataset (18 years, She et al. [2009]). What direction would the CSU Na lidar go if I commanded the ship? My answer is “go fully automatic and mobilized”. Currently, the running of the Na lidar system relies heavily on the man power. A multi-day observation requires the effort of a number of people. This extreme dependence on the man power limits the amount of observation time, unlike other ground-based instruments (airglow imagers and radars). One solution is to make the system automatically or remotely controlled. We also have demonstrated how much science the collaboration of Na lidar and OH imager has yielded. The more the Na lidar joins with other ground-based instruments (airglow imagers, radars, rockets, etc.), the more science contribution the lidar makes. It is also well-known that the middle atmosphere is very different at various latitudes. All of these require the lidar to be mobilized. The current Na lidar system is based on the dye laser system. Looking for affordable and stable solid-state laser sources is the next step [She et al., 2007]. Once the solid-state lasers replace the current ring dye laser and the PDA, the lasers can be remotely or automatically controlled without daily dye change. The alignment of the steering mirrors can also be motorized and remotely-controlled.

## References:

- She C. Y., T. Li, R. L. Collins, T. Yuan, B. P. Williams, T. D. Kawahara, J. D. Vance, P. Acott, D. A. Krueger, H-L. Liu and M. E. Hagan, Tidal perturbations and variability in mesopause region over Fort Collins, CO (41N, 105W): continuous multi-day temperature and wind lidar observations, *Geophys. Res. Lett.*, 31, L24111, doi:10.1029/2004GL021165, 2004.
- She, C. Y., J. D. Vance, T. D. Kawahara, B. P. Williams, Q. Wu, A proposed all-solid-state transportable narrow-band sodium lidar for mesopause region temperature and horizontal wind measurements, *Can., J. Phys*, 85(2), 111-118(8), 2007.
- She, C.-Y., D. A. Krueger, R. Akmaev and H. Schmidt, Long-term variability in mesopause region temperatures over Fort Collins, CO (41°N, 105°W) based on lidar observations from 1990 through 2007, *JASTP*, in press, 2009.